Fluid Transport and Entropy Production in Electrochemical and Microchannel Droplet Flows

by

Adedoyin Odukoya

A Thesis Submitted in Partial Fulfillment of the Requirements for the Degree of Doctor of Philosophy

in

The Faculty of Engineering and Applied Science
Mechanical Engineering Program

University of Ontario Institute of Technology

April 2012

Abstract

The growth of energy demand in the world requires addressing the increasing power requirements of industrial and residential consumers. Optimizing the design of new and existing large power producing systems can efficiently increase energy supply to meet the growing demand. Hydrogen as an energy carrier is a promising sustainable way to meet the growing energy demand, while protecting the environment. This thesis investigates the efficient production of hydrogen from the electrolysis of copper chloride, by predicting entropy production as a result of diffusive mass transfer.

Also, this thesis investigates the possibility of producing electrical energy from waste heat produced by industrial or other sources. The thermocapillary motion of fluid droplet in a closed rectangular microchannel is used to generate electrical energy from waste heat in a piezoelectric membrane by inducing mechanical deformation as a result of the droplet motion. Modeling, fabrication, and experimental measurement of a micro heat engine (MHE) are investigated in this study. Analytical and experimental results are reported for both circular and rectangular microchannels. A novel fabrication technique using lead zirconate titanate (PZT) as substrate in microfluidic application is presented in this study. This thesis develops a predictive model of the entropy production due to thermal and fluid irreversibilities in the microchannel. Thermocapillary pressure and friction forces are modelled within the droplet, as well as surface tension hysteresis during start-up of the droplet motion. A new analytical model is presented to predict the effect of transient velocity on the voltage production in the MHE. In order to predict the effect of the applied stress on voltage, the different layers of deposition are considered for thin film laminates. The highest efficiency of the system from simulated taking into

account the electromechanical coupling factor is about 1.6% with a maximum voltage of 1.25mV for the range of displacement considered in this study. In addition, new experimental and analytical results are presented for evaporation and de-pinning of deionised water and toluene droplets in rectangular microchannels fabricated from Su-8 2025 and 2075.

Acknowledgements

I will first like to thank my mentor and supervisor Professor G.F. Naterer for his guidance and unwavering support through the course of this research. I will also like to thank members of my thesis committee, Professor Marc Rosen, Professor Dan Zhang, Professor Murat Aydin, and Professor Anatoli Chkrebtii for their time and advice.

I would like to thank all members of the Clean Energy Research Laboratory (CERL) for their support and friendship, especially Ron Roberts. I would also like to thank the staff of the Faculty of Engineering and Applied Science at the University of Ontario Institute of Technology (UOIT) for their support, especially Svetlana Novak and Karla Gomez for their friendship and kindness. I am also indebted to Prashant Regulagadda for his support and generosity during this research. The members of the Center of Integrated Radio Frequency Engineering (CIRFE) research group at the University of Waterloo, Waterloo, Ontario are also greatly acknowledged for their guidance, especially Bill Jolley.

Financial support from the Natural Sciences and Engineering Research Council of Canada (NSERC), Ontario Graduate Scholarship (OGS), and UOIT Office of Graduate Studies Excellence Scholarship are gratefully acknowledged.

Finally, I would like to express my eternal gratitude to my family (Odukoya, Sanni, Ojukotola, and Opaleye) who have always given me endless love and support throughout my life. I would like to specially thank my father (Alhaji Adesupo Odukoya) for his persistent encouragement through the course of this research.

Table of content

List of figures

List of tables

List of appendices

Nomenclature

A	cross sectional area (m^2)
A_s	surface area (m^2)
C	concentration (mol/m^3)
C_l	molar liquid content (mol/m^3)
c_p	specific heat (J/kgK)
D	channel diameter (m)
D_{AB}	diffusion coefficient (m^2/s)
D_{ij}	electrical polarization (C/m^2)
D_{ij}	piezoelectric coefficient (C/N)
E	Young's modulus of elasticity
e_v	uncertainty in voltage measurement (V)
e_i	uncertainty in current measurement (A)
e_P	uncertainty in pixel measurement
e_w	uncertainty in width measurement (m)
e_{F_N}	uncertainty in frame number
e_{F_R}	uncertainty in width measurement (m)
F_c	Faraday's constant (96,785 C/ mol)
F	force (N)

F_N	frame number
F_R	frame rate
$f_{\mathrm{Re}\sqrt{A}}$	friction factor
g	acceleration due to gravity (m/s^2)
h	heat transfer coefficient (W/m^2K)
H	fixed height (m)
G	Gibb's free energy (J/kg)
i	current density (mA/cm^2)
I	current (mA, A)
i_o	exchange current density (A/cm^2)
j(r)	evaporation rate per unit area (kg/m^2)
k	thermal conductivity (W/mK)
k_p	coupling coefficient
l	thickness (m)
L	length (m)
m	mass (kg)
$\dot{m}$	mass flow rate (kg/s)
N	number of samples
n_d	electro-osmotic drag coefficient
P	pressure (kPa)
P_c	external pressure at boundary of meniscus (kPa)

P_i	power (W)
P_ς	Poiseuille number
Q	volumetric flow rate (m^3/s)
$q_s^{"}$	heat flux (W/m^2)
r	electrical resistance ($k\Omega$)
R	gas constant (J/kgK)
Re	Reynolds number
s	specific entropy (J/kg K)
$\bar{s}$	molar entropy (J/kgK)
S	entropy (J/K)
S_D	standard deviation
S_{gen}	entropy production (J/kgK)
t	time (s)
T	temperature (^oC or K)
T_{ij}	applied mechanical stress (N/m^2)
t_{pzt}	thickness of membrane (m)
t_{sub}	thickness of substrate (m)
u	instantaneous velocity (m/s^2)
U	uncertainty
u_b	bulk velocity (m/s^2)

$\overline{u}$	average velocity (m/s^2)
u^*	dimensionless velocity
V	volume (m^3)
V_D	voltage drop (mV, μV, V)
V_e	induced electric field (V/m)
w	width of microchannel (m)
W_m	piezoelectric displacement (m)
x	displacement (m)
x_c	radius of meniscus at equilibrium (m)
x_I	radius of meniscus at inlet (m)
z	height of meniscus (m)
Z	numbers of electrons
Z_n	distance from neutral axis (m)

Greek

α_t	charge transfer coefficient
α	thermal diffusivity (m^2/s)
Δ	discrete change
δ^*	boundary layer thickness (m)
η_v	overpotential (mV)
σ_e	electrolyte conductivity (1/Ωm)

ε	resistivity (Ωm)
γ	residual stress (N/m)
γ	proportionality factor
μ	dynamic viscosity (kg/m s)
ρ	density (kg/m^3)
σ	surface tension (N/m)
θ	contact angle (^{o})
ς	dimensionless time
ν	kinematic viscosity (m^2/s)
Φ	electric permittivity matrix (F/m)
ψ	arbitrary length scale (m)
χ	proportionality constant
ϕ	concentration gradient of evaporating fluid (mol/m^3)
Υ	aspect ratio

Subscripts

a	air
act	activation
an	anode
app	apparent
b	bias

c	critical contact angle
ct	cathode
d	droplet
DM	digital measure
e	experiment
elect	electrolyte
f	friction without roughness
ohmic	ohmic
i	initial
L	left
m	meniscus
MM	multimeter
NI	National Instruments
o	start
p	precision
pzt	lead zirconate titanate
r	reference
R	right
sub	substrate
t	total

Abbreviations

AECL	Atomic Energy of Canada Limited
ASME	American Society of Mechanical Engineers
CERL	Clean Energy Research Laboratory
CIRFE	Center of Integrated Radio Frequency Engineering
DC	Direct Current
DI	Deionized
DMFC	Direct Methanol Fuel Cell
EGM	Entropy Generation Minimization
GDL	Gas Diffusion Layer
GHG	Greenhouse Gas
IPA	Isopropyl Alcohol
LOR	Lift Off Resist
NI	National Instrument
NiMH	Nickel Metal Hydride
MCFC	Molten Carbonate Fuel Cell
MEA	Membrane Electrode Assemblies
MEMS	Microelectromechanical Systems
MHE	Micro Heat Engine
PAFC	Phosphoric Acid Fuel Cell
PEM	Proton Exchange Membrane
PEMFC	Polymer Electrolyte Membrane Fuel Cell

PZT	Lead Zirconate Titanate
RCA	Radio Cooperation of America
RF	Radio Frequency
RIE	Reactive Ion Etching
SMR	Steam Methane Reforming
SOFC	Solid Oxide Fuel Cell
SPE	Solid Polymer Electrolyte
TCP	Thermocapillary Pumping
TIMGen	Thermally Integrated Micro Generation
Ti-W	Titanium Tungsten
UV	Ultra Violet

Chapter 1 : Introduction

Water is the most abundant substance in the world. The ability to harness the immense amount of energy found in water in an environmentally friendly way can prolong our ability to preserve earth's natural resources. A variety of ways have been invented and commercialized to achieve this purpose, ranging from hydroelectricity, tidal energy, and thermochemical splitting of water to generate hydrogen.

Large scale (Macroscopic) power generating systems are conventional power plants, i.e., gas turbine plants, steam turbine plants, cogeneration, combined cycle power plants, nuclear plants, and combined cycle cogeneration power plants. These generally produce power in the order of megawatts. Fossil fuels are generally used to power such systems, resulting in increased emission of greenhouse gases (GHG). These large power generating units will be called macro scale power plants in this thesis. Microscopic power producing devices are usually miniaturized forms of macroscopic power plants. These systems are usually designed to produce a much smaller scale of power in the order of micro watts. The focus of this research is to generate energy on this smaller scale, which is in the order of microwatts. Systems which operate on such small scales do not usually require any fossil fuels for their operation, and they are classified as renewable energy systems. These systems will be referred to as micro scale power systems in this thesis.

Water is used as the working fluid in steam power plants to produce power in the other of megawatts. It is also used significantly in cooling of various industrial processes.

The use of water in such large units will be considered as macroscopic application of water. Water has also found significant application at much smaller scale in the order of micrometers. Water has been used in microcooling, sensors, actuators, and micropumps, which are classified as microscopic devices. This thesis examines a different and unique approach from the usual macroscopic way of using water as an energy mover, by exploiting the properties of water at the microscopic level. The motivation of working on the microscopic level stems from the desire to use smaller systems in our daily life. These devices require a source of energy for continuous operation. The conventional form of energy for most portable devices such as tablets, phones, mp3 players, and headsets is the battery, which is usually heavier and bulkier than the system mechanisms. The macro systems are mostly a combination of several micro-electromechanical systems (MEMS) coupled together.

Fossil fuels (natural gas, coal, and petroleum) have traditionally been used as energy carriers for large power generating units. Hydrogen is another prime energy carrier, which can be used to meet the growing energy demand on a macro scale. Although micro scale applications have a prime importance in our daily lives, macro scale power production are also significant. The increased need for reduction in GHG emissions requires a combined solution from both macro and micro energy systems. Increasing efficiency requires a reduction in entropy generation in micro and macro systems. This thesis specifically examines entropy production for two case studies: the micro heat engine (MHE) and electrolytic cells, as these are energy producing devices, which have a promising future. This thesis investigates the irreversibilities associated with mass transfer and diffusion in an electrolytic cell used for producing hydrogen. It

also investigates the entropy production as a result of heat transfer to a droplet in a closed microchannel.

MEMS for powering microdevices can reduce the energy consumed by conventional systems. Increasing the efficiency of these systems by embedded MEMS devices can reduce their energy utilization. For example, waste heat recovery by electrical components in MEMS devices can be used to drive these micro-electromechanical systems by producing micro voltages to power individual electrical components within microchips. This can be achieved by various methods of energy conversion and heat recovery and used for exploiting properties of thermoelectric or piezoelectric materials in MEMS devices. Thermoelectric materials have the ability to convert heat directly to electricity, while piezoelectric materials can convert stresses on a material into electric voltages. This thesis examines the transport phenomena associated with such energy conversion for MEMS devices, in particular the Micro Heat Engine (MHE). Earlier investigations [1, 2] suggest that surface tension of water can be used for thermocapillary pumping in a microchannel. This study further investigates the possibility of using this property to develop a MHE, which can be used to generate energy at the micro level.

Micro energy systems can be classified into two categories: regenerative and non-regenerative systems. Non-regenerative micro systems are scaled down designs of corresponding macro power systems. Some examples of such systems include: microcombustors, microbatteries, micro heat engines, micro turbines, and micro fuel cells. In contrast, regenerative power systems can be implemented as stand alone or hybrid power systems. These systems include: piezoelectric devices, thermoelectric

devices, micro-thermo-photovoltaic cells, and electromagnetic and induced coupled plasmas.

Although conventional batteries are relatively heavy and bulky, recent advances in MEMS technology have taken advantage of micro and nano-scale phenomena that can improve battery performance. Innovative new MEMS devices are becoming promising alternatives to conventional battery technologies. For example, researchers have built micro heat engines that work on heating and cooling cycles in flexing of a piezoelectric membrane [3]. Nano-motors powered by solar energy have been developed by researchers at the University of California [4]. Micro Solid Oxide Fuel Cells (SOFCs) have been developed by researchers in Alberta, Canada and Zurich, Switzerland [5]. This thesis investigates the use of cyclic heating and cooling of droplets in microchannels to provide a new source of energy conversion between thermal and mechanical energy for MEMS devices.

A closed microchannel is formed when an empty channel of an arbitrary cross section is sealed at all fluid inlets and exit boundaries of the channel. If a droplet is injected into the channel before it is sealed, a droplet in a closed microchannel is formed. When heat is applied to one end of the droplet in a closed microchannel, an increase in temperature at the heat source leads to a temperature gradient across the droplet. This results in the displacement of the droplet along the length of the channel towards the cooler end of the channel. This process is known as thermocapillary pumping. The resulting displacement increases the pressure at the closed end of the channel. The increased pressure is used to induce stress on a membrane at the closed end of the channel. This induced stress results in mechanical deformation of the membrane. The

mechanical deformation of the membrane results in flow of electrons in an externally connected circuit, which is the conversion of mechanical energy to electrical energy. Figure 1.1 shows a schematic of the MHE and the forces acting within the microchannel.

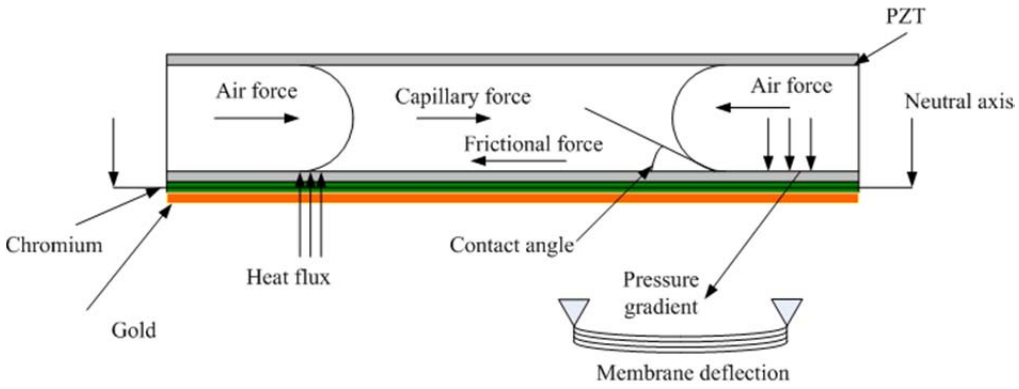

Figure 1.1: Schematic of problem configuration in the MHE

1.1 Types of power supplies

Power sources which require continuous sources of energy to sustain their power output can be classified as a non-regenerative power supply. Many of these systems have commercial potential, in today's industries. The current technology available to MEMS manufacturing can sustain production of most of these power sources, including the ability to improve their design and efficiency.

1.1.1 Batteries

Batteries are the most widely used regenerative power supply for MEMS devices due to their modularity, portability, and practicality. Some of the advantages of using batteries include their simultaneous generation and storage capability, high power densities, and easy replacement within the MEMS device. Batteries supply direct current

(DC) continuously, making the connection to MEMS devices less complicated than other micro power sources.

Nickel metal hydride (NiMH) is used to power most portable devices, but because of its relative size in comparison to the actual device, the batteries account for a high percentage of the total mass of the device. A common example is the cell phone, where the battery accounts for 36% of the total mass. This has led to the development of lithium ion cells as an alternative for supplying power to MEMS devices. They have a longer shelf life, high range of operating temperatures, low self-discharge rate, quick charging characteristics, high voltage output, and high energy efficiencies, compared to other batteries. However, some disadvantages associated with these batteries include: unsustainable charge at high temperatures, complex circuits required for charging, and excessive internal temperatures when over-charged.

Other problems associated with the use of the lithium–ion thin film and microbattery technology are packaging of a high volume of lithium and the losses associated with the packaging. Fabrication techniques are still limited for its incorporation into MEMS devices. The platinum coated substrates which are required for its fabrication make them less economical than other batteries. Recently developed ways to overcome the low current and capacity associated with lithium ion thin film cells include the following: 1) use of thin film silicon-zirconium-silver [6] cells, where the cells have greater capacity to store charge during cycling; 2) use of thick-film metal hydride cells, increasing the specific energy and power per unit area; and 3) use of 3-D micro batteries, which have a higher capacity due to an increased surface area and electro active layer. Hybrid batteries have also been considered as a viable option to increase the

power supply lifetime and the durability of a MEMS device. The application of hybrid batteries to gas chromatography has a power supply mass and volume of about 47.1% and 43.8% respectively [7].

1.1.2 Microcombustors, turbines and heat engine

Microturbine (miniaturized gas turbine) systems like their macro counterparts consist of miniaturized combustors, turbine, compressors, recuperators and generators. This system has been proposed as an alternative to microbatteries because of the potentially higher power density. Microturbines can use different types of fuel in the combustors, producing power at high efficiency, and resulting in lower emissions. These systems are relatively easy to fabricate [8]. Despite these advantages, if a recuperator is not used, the efficiency is lower than that of a reciprocating engine, thus making a reciprocating engine more advantageous for high load and high rotation speed applications. Currently, microturbines are capable of producing between 25 kW and 75 kW of power [8].

Past studies have focused on improving the efficiency of individual components, to improve the overall efficiency of the power systems. Such miniaturization efforts have been limited to the combustor, since a reduction in its size leads to incomplete combustion, high temperatures, and resulting material limitations. Premixed combustion has been proposed to maintain a low flame temperature, which causes problems such as flame blowout, flashback and inconsistent pressure in the combustion chamber. Silicon nitride has been suggested as an appropriate structural component for the micro-combustor [9]. An example is the microphotovoltaic combustion chamber.

Hydrogen is used as the fuel for the microcombustor because of its high heating value and low reaction time. The combustion of hydrogen in the presence of air results in photon production due to the selective emitter materials, dielectric filters, and photovoltaic arrays in the microcombustor [10]. In the process of generating electrical power, the filters recycle the photons with energy lower than the band-gap of photovoltaic cells, but transmit the photons with higher energy than the band-gap of the cells.

1.1.3 Microfuel cells

Fuel cells are being investigated as an alternative for powering MEMS devices. The components of a fuel cell include: an anode, cathode, and an electrolyte. The various types of fuel cells are mainly distinguished by the nature of the electrolyte used to separate the anode, and the cathode of the cell. The fuel is supplied to the anode, and the oxidant is supplied to the cathode. Hydrogen is the preferred fuel for the cell, while oxygen or air is the oxidant supplied to the cathode.

When an acidic electrolyte is used to separate the anode and the cathode, hydride ions are released at the anode and the accompanying electrons flow through an electric circuit, while the hydrogen ions react with oxygen to form water. In contrast, when an alkaline electrolyte is used, hydroxyl ions are liberated at the cathode. These ions react with hydrogen to create water and electrons [11] that flow through the electric circuit. The various types of fuel cells include the polymer electrolyte membrane fuel cell (PEMFC), solid oxide fuel cell (SOFC), molten carbonate fuel cell (MCFC), direct methanol fuel cell (DMFC), and phosphoric acid fuel cell (PAFC). Some of the advantages of fuel cells include: relatively high efficiency, cogeneration capability, high current density, quiet

operation and few moving parts required for its operation. Highlights the various types of fuel cells, power produced, current, and voltage generated have been published in past literature [12-20].

PEM fuel cells offer a unique advantage because of their resistance to mechanical vibrations and low operating temperatures, which range from 20 – 100^{o}C [21]. Their relatively small size compared to other fuel cells also makes them advantageous for MEMS devices. The cost of the platinum catalyst required for its fabrication make the cells costly. Another drawback in PEM fuel cells is controlling the quantity of water in the electrolyte to maintain conductivity and avoid flooding of the electrodes.

Direct and indirect methanol fuel cells have also been investigated for MEMS as a power source. When methanol is reacted with water in a direct methanol fuel cell, six electrons are produced, while a reformer is required in an indirect methanol fuel cell to produce hydrogen molecules. Fuel crossover has been observed in both cells. This tends to reduce the flow of electrons, reducing the production of electricity. Membrane electrode assemblies (MEA) have been investigated as a way of reducing the impact of fuel crossover [22]. Integrated MEMS fabrication is increasingly being investigated to enhance the capabilities of micro fuel cells. The aim is to design the anode and cathode of a fuel cell on one single substrate as opposed to two different substrates.

The fabrication techniques include photolithography, deep reactive ion etching, and electron beam deposition [23]. Ion etching can be used for making porous silicon layers for electrode assemblies, reducing the gas diffusion path and enhancing the bulk flow and efficiency of microfluidic transport [24]. The continued development of DMFC

is dependent on addressing the challenges associated with microfluidic transport control, water and temperature management, and optimization of the contact resistance between component materials. The use of SOFCs can be enhanced by minimizing the ionic resistance in the electrolyte, stress relaxation in fabrication processes, and preventing heat losses during its operation [25, 26].

1.2 Regenerative MEMS power sources

The ability to utilize waste heat is a form of regenerative energy source. Electrical energy generated from regenerative sources increases the overall efficiency of energy systems. The component efficiency of the energy harvesting system itself may be low, because the temperature difference between the source device and the ambient temperature is usually much lower than that associated with other power generating devices like turbines and reciprocating heat engines. The modes of generating electric power for microdevices from regenerative sources can be classified into three main categories, namely; solar cells, thermoelectric power, and vibrating power sources.

1.2.1 Solar cells

Solar cells have been studied extensively in past literature and implemented on a commercial scale in some MEMS devices. These cells typically consist of solar cell arrays and signal conversion circuits. The incident light on solar cells produces a photovoltaic effect. This is direct conversion of light to electrical current. Photons from sunlight are absorbed by the cells and produce proton holes, which enable current flow in the circuitry. These systems offer a unique advantage because they have no moving parts, making it easy to incorporate them into devices. These cells require a large surface area to produce high current density, which is not usually possible with microdevices. Another

disadvantage is the difficulty to predict the frequency of incoming sunlight. The solar cells are also cost prohibitive, making them less competitive than other technologies available for harvesting solar energy.

Most solar cells are microfabricated from multi-crystalline silicon or monocrystalline silicon. The efficiency of these devices is typically between 10 and 16%. Some novel designs have shown efficiencies between 24% and 40%, but at very high cost. The power producing capabilities, power conversion efficiency, and operating conditions of solar cells have been published in past literature [14, 27-50]. The strategies investigated in past literature to reduce the effect of surface area on the efficiency of solar cells include: photovoltaic cells arranged in series to produce high voltage [28]; microphotovoltaic cells integrated with a microwave antenna [51]; thermally integrated micro generation (TIMGen), which simultaneously produces heat and electricity [26]; and a laser photovoltaic system [29]. The power densities of novel solar cells are as high as those produced by thin and thick lithium and lithium ion batteries [52-55].

1.2.2 Thermoelectric power

Temperature gradients are capable of changing the electrical properties of certain materials, making them generate electricity in the process. This process is known as the Seeback effect. Some of the devices which have been manufactured based on this process have been reported in past literature [56-65]. Thermocouples are commonly used to measure temperatures, based on induced electrical current at the junction of two dissimilar metals in direct contact.

The schematic of a typical thermoelectric device is shown in Figure 1.2. The ability of thermoelectric devices to operate for long periods makes them very reliable for electricity generation. They also produce little noise and emission [58, 66].

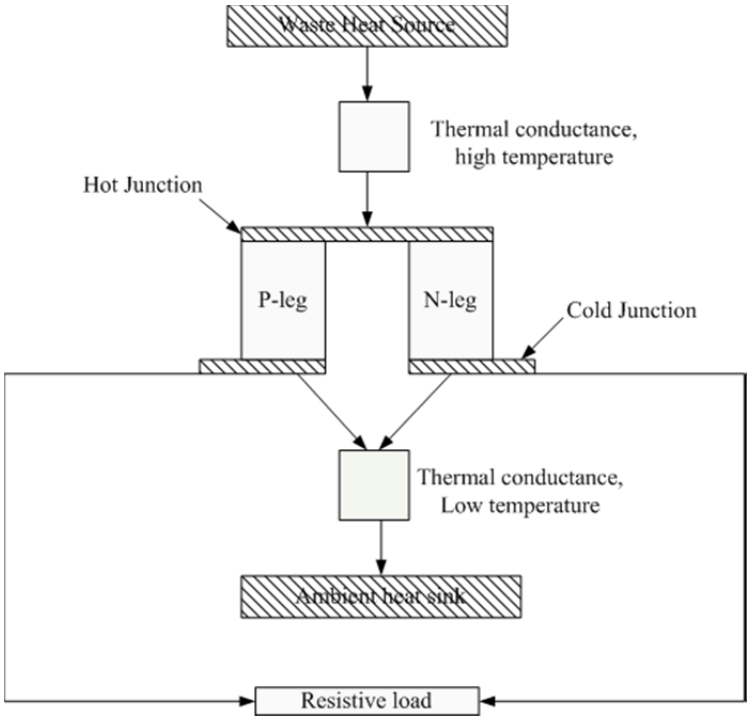

Figure 1.2: Schematic of thermoelectric energy harvesting system

The materials used for fabrication of these devices typically have a low melting point, low energy conversion efficiency, and low operating temperatures, which limit their application in commercial devices [67]. Materials like Bi_2Te_3, Pb-Te and Si-Ge used for their fabrication are also not readily available and release toxic contents during processing. Hybrid thermoelectric devices have also been explored as a way of improving the performance of thermoelectric generators. Such hybrid systems include two-stage solar concentrators, which simultaneously produce heat and electricity [46]; or a thermoelectric generator combined with thermoacoustic refrigerator [68].

1.2.3 Vibrating power sources

Generating power from mechanical vibration is receiving considerable attention because of the high energy density associated with such energy harvesting devices. The design of this power generating device is relatively simple and easy to fabricate, giving it great commercial potential.

Thermostatic, electromagnetic, and piezoelectric generators can be classified into this group of devices. These devices convert mechanical vibrations directly into electrical current. The generation of electric current using piezoelectric generators is yet to reach its commercialization potential. However, these devices have been used extensively in sensors, actuators, and transducers. Electromagnetic generators produce electricity by the relative motion of a conducting coil within a magnetic field. When the coil rotates in the magnetic field, current is induced into the coil, which is harvested and supplied to a load or stored in batteries [69, 70].

The range of electricity generated is proportional to the magnetic field strength, number of turns of the coil, and angular velocity of the coil. Some innovative designs of electromagnetic generators and their respective power densities have been cited in past literature [71-82]. This generator does not require any input voltage but generate low voltages, which usually require transformers for MEMs devices. There are also challenges associated with fabrication of micro scale magnets. The number of turns of the coil at the micro scale has hindered its application in MEMs devices.

Electrostatic generators are very similar to capacitors. They consist of two conductive plates separated by air, vacuum, or a dielectric to ensure the plates are

electrically isolated. The plates are also capable of moving relative to one another [83]. The two modes of energy conversion in electrostatic generators are constrained capacitors and constrained voltage. When the capacitor is constrained, the voltage is allowed to increase while the capacitance decreases. In the case where the voltage across the capacitor is constrained, the charge leaves the capacitor and the capacitance decreases [84]. An external source of power is required to charge the plates in order to store energy, which is later used by the MEMS device.

The energy produced is equivalent to the work done to overcome the electrostatic force between the plates. The three groups of electrostatic generators are in-plane overlapping varying, in-plane gap closing, and out off-plane gap closing [84-87]. The constrained approach, however, generates the highest amount of energy. The in-plane gap closing technique has been shown to produce the highest amount of power of the three groups [86]. Electrostatic generators are amenable to surface micromachining, which make them well suited for incorporation into MEMS devices. The power densities of some electrostatic generators which have been reported in past [75-83, 85, 86, 88-92]. Applications of this device have focused on cardiac pacemakers, coulomb force generators, and biosensors [88, 93-95].

The energy density of electrostatic generators can be increased by reducing the plate's gap spacing and surface area to nanometers or micrometers [69]. The impedance and voltage produced by these devices are high, reducing the current available to supply MEMS applications. Due to the low current produced, secondary circuitry is required, thereby increasing its complexity. Electrode shorting has also been observed in micro scale applications.

Piezoelectric materials produce electricity when they are mechanically deformed. The crystallographic structure of the material is arranged in such a way that the positive and negative charges cancel each other around the center of gravity, when no force has been applied to the material. Once a force is applied to the material, a distortion of the latter arrangement occurs within the material, forming dipoles within the material. The dipoles polarize the material, which are neutralized by the free flow of electrons within the material. Piezoelectric effects can be observed in the materials such as composites, single crystals, ceramics, polymers, thin films, and ferroelectric materials. Specific materials which exhibit piezoelectric effects include: lithium niobate ($LiNbO_3$), lead zirconate–lead titanate (PZT), barium titanate ($BaTiO_3$), quartz, polyvinylidene di-fluoride (PVDF), and Pb $(Mg_{1/3}Nb_{2/3})O_3$ (PMN). The application and power density of piezoelectric based devices have been reported and analyzed in past literature [3, 8, 96-103]. Some fabrication techniques for piezoelectric devices include photolithography, sol-gel, screen print and photomask [3, 96, 97, 104].

1.2.4 Nano-electromechanical and microfluidic power generation

Nanofluidics is still in a relatively early stage of commercial application but it shows great promise, as a substantial amount of research is underway in this area. The transport and physical properties at the nano-scale are not well understood. Conflicting research findings are still contested in literature. Microfluidics on the other hand, has less conflicting concepts and has been used significantly commercially. Micro heat exchangers have been developed for convective cooling of microelectronic circuits [105, 106]. MEMS have been used for bio-devices to separate biological cells and enable blood

analysis [107]. Near-wall flow control [108], micro engines [3], and microchannel batteries [109] are other examples of recent MEMS innovations.

Researchers at the University of California have developed a nano-motor, which operates by transferring atoms between two molten metal droplets in a carbon nanotube [110]. The relaxation oscillator consists of two liquid metal droplets along a surface within a 200 nanometer enclosure. Electrical current passes through the nanotube, which moves metal atoms from the larger droplet along the nanotube to the smaller droplet. As a result, the small droplet expands and eventually touches the larger droplet. This contact generates a rapid release of energy at a contact relaxation point, when the larger droplet absorbs atoms that were previously transported through the nanotube.

Researchers at the National Institute for Nanotechnology, University of Alberta, Canada, have fabricated a micro-device that produces electricity from the interaction between flowing water and the surfaces of microchannels [109]. The chemical reaction between water and the surface leaves the walls negatively charged, which in turn attracts positive hydrogen ions in the water. Water flow through the microchannel then produces a streaming electric current by moving the positively-charged ions in the direction of the water current. Yang *et al.* [109] achieved electrical currents between 1 - 2 μA, by flowing water through a glass filter containing millions of microchannels across a 30 cm hydrostatic pressure drop. The electrical current was raised by increasing the salt concentration in the flowing solution. The device produced a sufficient amount of electricity to generate power for a light-emitting diode. A 1500nA current was generated from a 30 cm hydrostatic pressure drop with tap water. The authors described various ways to enlarge the current, such as a higher pressure drop (requiring additional pump

input power), smaller thickness and larger surface potential of the porous material, and using a salt solution as the operating liquid. Also, a higher power output can be achieved with a larger external load, as the current remains nearly constant when the external load is much smaller than the resistance of the microchannel array.

Researchers at Oregon State University, Washington State University and the US Army Research Laboratory have collaborated to develop a novel energy source called the P^3 micro heat engine [3]. An external heat source is used to generate phase change and increase the vapor fraction of a saturated liquid-vapor mixture in a chamber. The expansion process flexes a piezoelectric membrane to generate an output voltage. The volume of the saturated mixture is then reduced in a cooling cycle. Repeated heating and cooling cycles are required to maintain cyclical operation of this heat engine. Three units can produce 40 microwatts of electricity, which would be sufficient to supply power for a wristwatch, using body heat of the person as the heat supply for the micro engine. Each unit is about twice the thickness of a human hair and two millimeters square in size.

The P^3 micro engine uses a lead zirconate titanate (PZT) film to convert mechanical work into electricity, through a membrane generator that is formed by depositing a bottom electrode, PZT, and top electrode on a SiO_2/Si membrane. A power output of 4V and 1mW has been achieved with membrane generators ($9mm^2$ in area and 2-3μm thick). The material properties of the PZT film can be further improved to optimize the electrical performance and mechanical reliability of the membrane generator. The authors modified several processing parameters, such as orientation, crystal structure and chemical gradients within the PZT film to improve the performance of the membrane generator.

Glockner and Naterer [2] proposed another novel micro heat engine, which provides certain advantages over past methods. Rather than a fuel source such as propane, the method uses thermocapillary pumping (TCP) as a driving mechanism to move a discrete droplet within a closed-ended microchannel and generate electricity. The microdroplet would act like a piston to expand and compress the adjoining gas chambers, thereby flexing a piezoelectric membrane and the channel ends to generate electricity. TCP is a non-mechanical method of fluid pumping that takes advantage of temperature-dependent changes of fluid surface tension. It is driven by internal pressure differences, resulting from surface tension variations at the ends of a discrete droplet, due to an applied temperature gradient. A prototype of a micro heat engine was manufactured with microchannels, fluid access holes, heaters and heater leads at the University of Manitoba, Canada [111].

The application of microfluidic devices is dependent on the ability to control fluid motion in microchannels. The principles used to control the fluid motion include pressure change, electromagnetic induction, and heat transfer. This thesis will use heat transfer to cause a change in surface tension of a droplet in a closed microchannel to induce fluid motion. When heat is applied to the droplet, the change in surface tension causes a change in the contact angles at the ends in order to maintain a constant volume [2]. Due to the complexity of the fabrication process [112] the MHE was not fully fabricated.

This thesis examines an alternative method of fabrication to build the MHE, and in addition, investigates analytically the droplet dynamics associated with the MHE. The novel design uses a PZT substrate as the base for the MHE, which has not yet been used to pattern microfluidic devices. Although the surface roughness of the substrate is higher

than silicon substrates, it still possesses excellent surface characteristics for the microfluidic motion. The effect of surface roughness on transport properties will also be investigated in this study. A solution to the heaters was found by using titanium-tungsten (Ti-W) as a heating element as opposed to the aluminum heater original investigated by Glockner [112]. The channels were also developed using SU-8, which provides excellent structural properties for the microchannels. Details of the design and fabrication will be described in subsequent chapters.

1.3 Motivation

In accordance with the above discussion in the prior sections, the motivation for this thesis is to develop better waste heat energy utilization. The need to develop alternate power sources for microdevices was the focus of this research. Most of the designs available are often complex and difficult to fabricate. If one could develop a simpler and cheaper method of harnessing energy from waste heat, the commercialization time of the device to go from the prototype to a market stage could be shortened. Numerous technologies are never realized commercially due to their complexity in the environment in which they operate. The design of the MHE in this thesis takes into consideration the seamless integration into existing microdevices. The method of having very few moving parts and a solid structural stability makes this device well suited for integration into micro electromechanical assemblies. Although water is a widely used liquid and has been studied extensively on the macroscopic scale, several publications [113] have conflicting information about its behaviour on the micro/nanoscale. Additional experimental and analytically analysis of water droplets at the micro scale will add to the body of knowledge of microfluidics and micro scale heat transfer.

1.4 Objectives

The main objective of this research is to develop a simpler design rubric for the MHE, which could be more easily commercialized. The primary goal was to investigate transport phenomena that affect operation and performance of the MHE. Additional objectives of this research were to: 1) increase the thermodynamic efficiency based on analyses of the MHE, and 2) account for entropy generation in the operation of the MHE to investigate Second Law losses associated with the MHE. The entropy generation from the MHE was investigated analytically to account for the losses associated with the MHE to improve the efficiency of the device. Developing a model to predict the entropy production in an electrolytic cell was another objective of this study.

This study was performed to investigate the losses associated with producing hydrogen from HCl/CuCl electrolysis. No models currently exist to compare experimental results from half-cell reactions of Atomic Energy of Canada Limited (AECL), hence a predictive model was developed in this thesis. A new model which could be used to predict the entropy generation for the full cell reaction was developed in this thesis.

Investigating the expected voltage from the MHE was an objective to ensure its viability in future applications. Alternate models that could predict the transient nature of the operation of the MHE was a key obstacle in comparing numerical and experimental results. The assumption of steady state models was seen to over-predict experimental observations, highlighted later in this thesis. This confirmed the need to study the transient droplet velocity in the micro heat engine. Past studies indicated that surface roughness had a significant effect on the droplet velocity. One of the objectives of this

dissertation was to account for surface roughness in analytical modeling of the MHE. Although the primary objective was voltage production of the MHE, it became apparent during the course of this study that the rate of evaporation and pinning of the droplet in the microchannel were essential in understanding the operation of the MHE. The effects of evaporation and de-pinning on droplet width were also investigated in this study.

Chapter 2 : Literature review

This chapter will highlight the developments in the areas of microfluidic and electrochemical transport phenomena. This will include droplet displacement, entropy generation, surface roughness, transient velocity distribution, electric voltage generation, droplet evaporation, and droplet de-pinning.

2.1 Droplet displacement in microchannels

This thesis investigates heat transfer and resulting changes of surface tension within a droplet in a closed microchannel. These changes of surface tension lead to thermocapillary motion of the droplet. When heat is transferred to the droplet, the change in surface tension causes a change in the contact angles at both ends, in order to maintain a constant volume. This leads to thermocapillary driven motion of the droplet [2]. Past studies have investigated fluid motion in microchannels of various shapes such as: rectangular, circular, and trapezoidal. Open and closed microchannels have been analysed, both experimentally and numerically, in past literature. Sobhan and Garimella [114] published a review on heat transfer and fluid flow in micro and mini channels. The study indicated departure of past experimental results from theoretical predictions of heat transfer in microchannels.

Experimental and numerical studies of hydrodynamics and heat transfer in rectangular microchannels were reported by Baviere *et al.* [115], showing a decrease in the Nusselt number for laminar flow at a constant Poiseuille number. Lee and Garimella [116] predicted 3-D heat transfer in rectangular microchannels of different aspect ratios. A correlation was developed for the Nusselt number, and results showed that local heat transfer rates decline at the edges of the channel. Muwanga *et al.* [117] compared the

heat transfer rates of uniform and varying cross sectional area in microchannels. Increasing the inlet area improves the heat transfer characteristics of the microchannel flow. As examples of other geometrical configurations, helical configurations of fluid flow and heat transfer have been investigated in past studies [118, 118-120]. Chua *et al.* [118] conducted similar experiments as this thesis, using a helical heat source for the microchannel.

Past numerical analyses of heat transfer and fluid flow in microchannels showed that thermocouples embedded in the channels influence the flow regime [121]. Friction was also shown to affect the thermal performance of the microchannels [122, 123]. The frictional losses declined upon heating of the channel at low Reynolds numbers, due to a reduction of viscosity of the fluid in the channel. Heat transfer rates were highest at the entrance of the channel. A decrease in flow rate reduced the thermal resistance. Khan and Yovanovich [123] showed that lower fluid friction increases the heat transfer effectiveness of the channels. Past studies [124-126] showed that accurate predictions of the effects of surface roughness on the flow distribution are significant for effective control of microfluidic motion. The surface roughness has a significant effect on wall velocity slip, pressure gradient and heat transfer coefficient in a microchannel. These fluid flow parameters are essential to develop theoretical models, which can accurately predict the flow in microchannels.

Glockner and Naterer [1] developed a computational fluid dynamic (CFD) model for heat transfer to an immersed moving droplet in a rectangular closed microchannel. It was shown that increases of the temperature at the exterior of the channel have a significant effect on surface tension within the droplet. A higher thermocapillary pressure

occurs at the cooler end of the channel. A pressure change across the microchannel leads to the droplet displacement. When the heat source is removed, the droplet returns to its original position and balances pressure at both ends of the channel.

2.2 Entropy generation in microchannels

This thesis will investigate the processes of heat and entropy transport within the droplet in the microchannel. Experimental and predicted temperature changes across the droplet in the closed microchannel will be examined in this thesis. Also, entropy generation of thermal and friction irreversibilities associated with the droplet motion will be investigated. Entropy generation minimization will be used to optimize the channel dimensions and flow parameters, such as the optimal Reynolds number (Re) and applied heat flux.

Although numerous past studies have examined fluid and heat flow in microchannels, few have examined entropy and the Second Law, particularly few or none involving immersed droplets as considered in this thesis. To obtain new physical insight into various energy conversion mechanisms in microchannel flows, this thesis investigates friction and thermal irreversibilities of entropy production due to droplet motion in closed microchannels. Past performance criteria for channel flows were examined by Zimparov [127], using the method of entropy generation minimization (EGM) [128]. Naterer and Adeyinka [129] presented a numerical model to examine entropy production in open microchannels, including electromagnetic irreversibilities, induced at the contact between the fluid and channel walls. A model to analyse heat and entropy transfer in a semi-infinite medium was developed by Hussain *et al.* [130], based on extended irreversible thermodynamics. In this thesis, the droplet is modelled as a

semi- infinite body, since the main source of heat transfer is axial heat conduction along the channel length, which is much larger than its diameter. Past studies have applied Bejan's method for analyzing entropy generation in microchannel flows [127-131]. This study extends Bejan's method to include additional physical phenomena associated with thermocapillary droplet transport in microchannels.

Entropy generation through circular ducts was investigated by Dagtekin *et al.* [132] to determine the effects of pumping power on the input energy requirements. The optimal Reynolds number was found to increase when the pumping power increases, but with decreased entropy generated in the process when a fin configuration is used to enhance the heat transfer along the channel. Ratts and Raut [133] developed a predictive model, which could be adapted to internal flows of any cross-section for a given mass flow rate, and uniform heat flux. The model showed good agreement with Bejan's model, although this thesis extends the capabilities to include additional thermophysical transport processes. Jakowski [134] developed an algorithm to determine the optimal shape of a duct to minimize entropy generation in internal flows. The results showed that by controlling the irreversibilities, this can minimize the entropy generation rate.

2.3 Entropy production in electrochemical processes

Hydrogen is frequently cited as a major solution to address climate change and a sustainable alternative to fossil fuels as an energy carrier. Hydrogen burnt in the presence of oxygen produces only water vapor, which can significantly reduce greenhouse gas emissions into the atmosphere. However, sustainable production of hydrogen on a large commercial scale is challenging, since most of the world's hydrogen (about 96%) is currently derived from fossil fuels. Also, there is a large amount of energy required to

produce hydrogen. A number of industrial processes have been developed for hydrogen production, including steam-methane reforming (SMR), partial oxidation of bitumen, thermo-chemical cycles (such as the copper-chlorine cycle), water electrolysis and steam electrolysis [135-137]. This thesis focuses on mass transfer within a particular electrochemical process of the copper-chlorine (Cu-Cl) cycle, involving an electrochemical cell that produces hydrogen from electrolysis of cuprous chloride.

Hydrogen is used widely by petrochemical, agricultural (ammonia for fertilizers), manufacturing, food processing, electronics, plastics, metallurgical, aerospace, and other industries. Also, auto-makers are investing significantly in hydrogen vehicles, so major efforts worldwide are investigating lower-cost methods of sustainable hydrogen production. Bio-hydrogen production processes are one of the emerging methods (dark-fermentation, photo-fermentation, and biocatalyzed electrolysis) being investigated as a low cost alternative for hydrogen production [138]. These processes have 57-79% efficiency, along with a significant reduction of GHGs when compared with conventional steam reforming processes. However, these processes are yet to be used in commercial scale applications. Bio-hydrogen systems have been proposed to power proton exchange membrane (PEM) electrolyzers [139].

Wind and solar plants have been proposed in several studies [140], as a renewable energy source to provide electricity for water electrolysis. However, the inability to effectively predict weather patterns and intermittency has limited the commercial viability of these methods for large-scale consistent production of hydrogen. A new method of producing hydrogen by exploiting the dissociation of water with a continuous-action reactor has been investigated in earlier studies [141]. The method requires a much

larger energy input than the technique investigated in this study. In this thesis, electrolysis of CuCl/HCl consumes less energy input to produce hydrogen than conventional water electrolysis. However, challenges include materials that can withstand the corrosive hydrochloric acid, which is used as an oxidant in the electrochemical reaction.

In recent years, electrolysis has been developed as an efficient method to generate hydrogen at lower costs. Three types of electrolysis have been developed on a commercial scale [142], with two based on the alkaline electrolyzer and a third based on a solid polymer electrolyte (SPE). The latter is also called a Proton Exchange Membrane (PEM) electrolyzer. Although these electrolytic processes do not generate greenhouse gas (GHG) emissions, the systems require electricity, which may be generated from power plants that emit GHGs. Advantages of SPEs over alkaline cells include greater safety and reliability, materials that can withstand higher pressures and compact structures within the cell [142].

In order to address the power consumption from the electrolytic process, some researchers have investigated electrolysis with existing power systems to co-generate electricity and hydrogen and improve the overall plant efficiency. An investigation of the integration of steam electrolysis with an advanced CANDU Reactor (ACR-1000) shows that plant efficiencies ranging from 33-34% can be achieved [135]. Unlike electrolysis for electrochemical decomposition of water, this thesis investigates cuprous chloride electrolysis in a thermochemical cycle, which can lead to higher overall efficiency of hydrogen production [136] if the process in combined with nuclear power plants or other heat sources. The oxidation of cuprous chloride (CuCl) during an electrochemical

reaction in the presence of hydrochloric acid (HCl) can be used to generate hydrogen in the Cu-Cl cycle. The process requires electricity as the energy input, which can be supplied from a nuclear power station or other source of renewable energy, such as wind or solar power.

Electrolytic cells have similar features and configurations as fuel cells, but opposing objectives. The major difference between fuel cells and electrolysis is the direction of current flow. The fuel cell generates electricity, while the electrolytic cell requires electricity as an input. Some past studies have indicated that combining both systems into a single unit can yield a highly efficient energy conversion system. The two-phase flow in a direct methanol fuel cell (DMFC) is similar to flow that occurs in an electrolytic cell. The latter flow conditions have been simulated and examined to show how the performance of the fuel cell was affected by temperature, pressure and concentration of methanol [143]. Heat and mass transfer occurs through porous electrodes of a fuel cell in local thermal non-equilibrium states [144], generating losses due to entropy production at the interface of the electrode and electrolyte.

Entropy production in proton exchange membrane fuel cells (PEMFC) has been examined by Naterer *et al.* [145]. This thesis performs a similar study to characterize irreversible losses in an electrochemical cell of cuprous chloride electrolysis. Electrochemical mass transfer is an irreversible process, which generates entropy to degrade performance of the electrolytic cell by increasing the voltage losses. Voltage losses in electrochemical systems can be characterized effectively by entropy and the Second Law of Thermodynamics [131]. Methods of heat-entropy analogies and planar

laser induced fluorescence [146,147] have utilized entropy-based methods to reduce irreversible losses in thermofluid systems.

This thesis formulates the diffusive mass transfer in an electrochemical cell with respect to entropy and the Second Law of Thermodynamics, in order to develop a useful alternative methodology of identifying and reducing the overall system losses. It investigates irreversible losses and entropy production of diffusive mass transfer in an electrochemical reaction of cuprous chloride and hydrochloric acid. The effects of ohmic and activation potential on the voltage drop across the electrolytic cell will be formulated. Operating parameters like the overpotential, current density, charge transfer coefficient, temperature and exchange current density will be analyzed as performance indicating parameters. The formulation presents a new predictive model and results for the analysis of electrochemical irreversibilities, associated with electrolysis of cuprous chloride for hydrogen production.

2.4 Effect of surface roughness on flow in microchannels

Experimental measurements in laminar and turbulent flow were presented in 1993 by Nikuradse [148]. It was initially believed that the transition from laminar to turbulent flow occurs at about a Reynolds number of about 2,300, but recent studies [149] have shown that this only occurs in channels with diameter greater than 1cm. Experimental results on the effect of relative roughness on heat transfer in circular channels (1.06mm, 0.62mm diameters) were reported by Satish [149]. As the channel diameter reduces, the effect of surface roughness on heat transfer and pressure drop increases across the channel. A numerical model to investigate the effect of the different roughness patterns on the Poiseuille number and average Nusselt number was developed by Zhang *et al.*

[150]. The latter numbers differ significantly from those reported for a smooth channel. The roughness patterns included triangular, semicircular and rectangular patterns. Experimental results from this thesis show that an average roughness height is a better approach as the patterns formed as a result of microfabrication are highly irregular. Experimental results for flow in a micro tube were reported by Mala and Li [151], which indicate that at low Reynolds number, the Poiseuille flow assumption is sufficient for analytical studies. However, the results showed that significant variation from the steady state assumption is observed at higher Reynolds numbers. An empirical correlation was developed to predict the dynamic viscosity for a rough surface.

2.5 Piezoelectric power generation

The main difference between various methods of piezoelectric power generation is the nature of the applied force on the piezoelectric material, as necessary for deformation required to generate the electric voltage. Past studies have used combustion [3], electrostatic induction [83], mechanical vibrations [152] and acoustic vibrations [153] to achieve distortion of the crystallographic structure of the piezoelectric membrane to produce an electric displacement in a preferred direction.

This study uses displacement of a microdroplet in a closed microchannel to generate the deflection in a piezoelectric membrane. The induced motion occurs as a result of changes in the surface tension of the droplet when heat is applied on one end of the droplet, forcing the droplet to compensate for this change in order to maintain a constant volume, and inducing translational motion in the process. Glockner and Naterer [2] were the first to propose a MHE working with a similar principle. The P_3 micro heat engine works based on combustion in a closed channel [3] and also makes use of the

deflection to generate voltage. Most of the piezoelectric energy harvesting devices in past literature focus on the mechanical deformation using static loading conditions [154]. Cook-Chennault *et al.* [154] investigated the use of piezoelectric effects to harness energy from household devices with the aid of a bimorph composite of piezoelectric membranes.

Different configurations of inserts have been investigated as energy harvesters using piezoelectric membranes [99, 155] in 31-mode loading conditions. These devices were able to produce high voltage, low current, and low energy devices capable of storing energy like a capacitor. A unique insert based on a two layer unimorph curved membrane was developed by Yoon *et al.* [156]. The width of the membrane was found to have a more significant effect on the charge generation than its length. It was also revealed that increasing the thickness of the membrane also improves the charge generation, but this can have an adverse effect on the load requirement to flex the membrane. It is important to note that although an increased size of membrane will generally improve the quantity of charge, an optimal sizing of height, and length to width ratio are required for a minimal force input.

In bio-medical industries, piezoelectrics have been used to generate energy from fluctuating blood pressure [8]. An energy harvester fabricated from PZT which vibrates in a 33-mode has been developed to power orthopaedic knee implants [100]. The life cycle was discovered to decrease linearly over 10 years of device usage. The power output between stacked and single layers of PZT of the micro-assembly were compared, and results indicated that stacking does not have any significant effect on power output,

but a reduced voltage output was recorded. Low voltage output harvesters are easier to integrate into devices in which they are required.

2.6 Droplet evaporation and pinning

Evaporation is a relatively simple phenomenon, but highly complex to model due the various processes which are associated with heat transfer and mass transfer occurring simultaneously. A comprehensive review of different phenomena associated with evaporation was conducted by Bonn *et al.* [113]. The experimental and numerical analysis of heat and mass transfer based on the contact line displacement was investigated. The main challenges include the liquid-vapor contact line relative to the vapor-solid contact line, and both relative to the substrate- liquid contact line. The initial spreading of liquids on a solid substrate can be analysed using the Gibbs adsorption equation to estimate the change in surface tension [157]. In other to sufficiently explain the dynamics of evaporation, the hydrodynamics of droplet spreading must be clearly understood. This problem has been studied by Bonn *et al.* [113]. However, most of the studies cited in past literature focused on droplet spreading on a flat surface.

This thesis investigates droplet spreading in a microchannel. The analyses in past literature usually assume that the droplet is spherical [158-161], but recognise the existence of a film, which tends to be detached from the main surface. Figure 2.1 shows the pinned film and the main part of the droplet. There are two major ways in which evaporation occurs on a flat surface. The droplet radius remains constant, while the contact angle of the liquid-substrate contact angle decreases [158]. The other method of evaporation is the contact radius that reduces while the contact angle remains constant [158]. In the latter case, both the contact angle and contact radius reduce simultaneously

at a certain contact radius. This stage precedes the de-pinning process. The de-pinning process occurs when the film, which appears to be separate from the main droplet, starts to evaporate. The separation of these two layers of the liquid has been used to transfer solid particles in a liquid droplet to a substrate in a previous study [162]. This is the technology used for the inkjet printer [163] as the carrier liquid evaporates and the patterns are left behind on the paper. Deegan [163] used this transport phenomenon to explain the pattern of satins left behind by a drop of coffee

The problems associated with evaporation also occur due to the nature of the droplet during evaporation. The boundary of the surface can be either saturated with vapor or a mix of liquid and vapor of unidentifiable proportions [164]. A temperature drop within the droplet occurs as a result of evaporation, but it is generally difficult to estimate how much of this heat transfer goes to the substrate or the atmosphere as the process is occurring at atmospheric conditions. This also leads to internal recirculation within the droplet caused by a change in surface tension [165,166].

The flow within the droplet always occurs towards the edge of the droplet so as to maintain constant a volume. The constant change in contact angles lead to a variation in advancing and receding contact angles. Various conflicting methods have been proposed for estimating the varying contact angles [167, 168]. The method of estimating the change in contact radius with respect to contact angle, which appears to be agreeable with most researchers, is the semi empirical approach proposed by Deegan *et al.* [158]. The authors proposed a relationship by assuming an equivalent contact angle, which is based on the change in volume of the droplet and proportional to an exponential function of time [158]. New results from experiments conducted by Shahidzadeh [169] showed that

although the method by Deegan is possible the vapor above the droplet accounts for the variation in the exponent. Different liquids will give different exponents in relation to time, i.e., $R \propto (t-t_0)^{\lambda}$, where λ varies for different liquids with respect to the equivalent contact angle. Here R is the contact radius, t is the time for the droplet of a given volume to evaporate, and t_0 is the instantaneous time.

The behaviour of wetting and non-wetting fluids differs during evaporation. Cahcile *et al.* [170] provided a semi-empirical correlation for estimating the hydrodynamic behaviour of alkanes on a wetting surface. The analysis neglected the pinning of the droplet on the substrate. The authors highlighted that although the model requires further investigation, the assumption of a spherical shape of the droplet appears to be an over simplification of the problem. It was recommended that an electrostatic model including the pinning process should be considered.

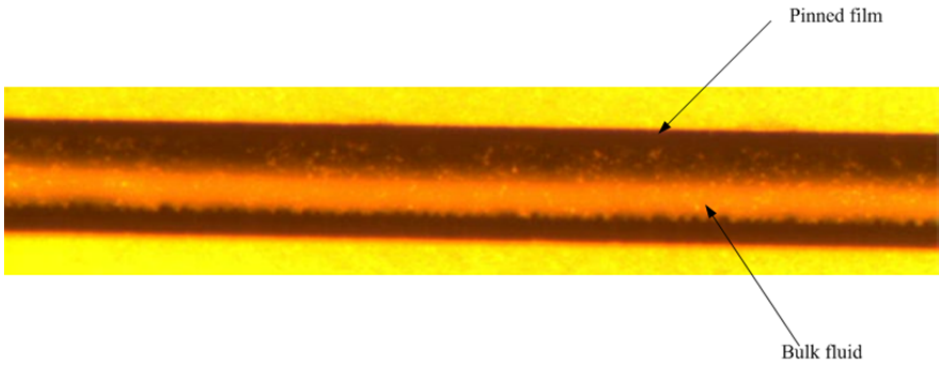

Figure 2.1: Separation of bulk fluid and pinned film in a SU-8 2025 microchannel with a depth of 20 µm

The next chapter will outline the experimental setup and procedures to investigate the operation of the novel design for the MHE. Detailed steps on the fabrication techniques will be outlined and an uncertainty analysis of the experimental measurements will be presented.

Chapter 3 : Experimental method and apparatus

A prototype to verify the concept of thermocapillary pumping in a microchannel was fabricated at the University of Ontario Institute of Technology - Clean Energy Research Laboratory (CERL). Experimental measurements were also conducted at the same location. There was a need to conduct the experiment in a controlled environment as the dust particles in the atmosphere could affect the observations and results. The Center of Integrated Radio Frequency Engineering (CIRFE) at the University of Waterloo, Ontario, was used to fabricate and perform the experimental measurement of the MHE. This laboratory was chosen because it allowed processing of metal deposition in its clean room. Most microfabrication facilities work with bulk micro machining of silicon, which are highly sensitive to metallic contaminants.

3.1 Experiment to verify concept

Prefabricated capillary tubes were used for the microchannels. Once the open channel is formed, a droplet is allowed to flow into the microchannel by capillary movement of water, when the channel is inserted into a volume of water. The droplet length is measured from the images obtained from the microscope for each experimental trial. The ends of the microchannel were then sealed after the droplet was injected into the channel. The ends of the channel are sealed with epoxy. Once the ends of the channel are sealed, the construction of the closed microchannel is complete, and it can be inspected under a microscope. An EMZ series stereo microscope (4.5 × magnification) was used to observe the displacement of the droplet.

The experiment consists of a microscope with a digital camera mounted on the viewing portion, and connected to a computer. A schematic of the experimental

measurement layout is shown in Figure 3.1. The circuit board placed on the image stage has a prefabricated substrate, attached to the surface. The substrate has an embedded thermocouple and helical heating coils. The thermocouple and heating coils are connected to a National Instruments (NI) digital acquisition board and computer. The acquired data is processed by Lab View Signal Express. The microchannel is placed in the center of the heating coils, in such a way that the droplet is divided evenly across the heating coils. The droplet is positioned so that only the droplet is heated, and not the air regions.

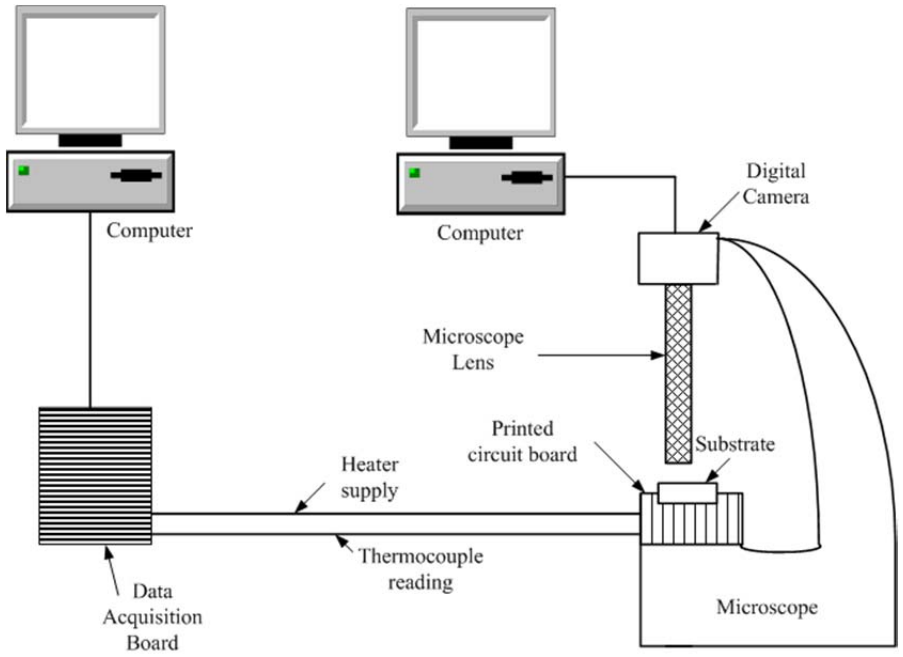

Figure 3.1: Schematic of microchannel experiments

The initial voltage readings (before heat is applied to the droplet) were measured. The initial temperature is then obtained based on a known relationship between the measured voltage and temperature. Alternating current is supplied to the heater through a rheostat. The readings from the digital camera and NI software are then synchronised, so that changes in temperature and displacement, with respect to time, can be measured

simultaneously. The data is acquired at a frequency of 100 Hz. The droplet moves to the right of the channel when heat is applied; then it moves back to its original position after heat is removed. The images of droplet movement are recorded by the camera. The distance moved by the droplet is estimated based on the number of pixels displaced between an initial and final position. The equivalent room temperature is converted to a voltage based on the following correlation,

$$V_r = 50.38118782\left(T_r\right) + 0.0304758368\left(T_r^2\right) - 0.0000856810657\left(T_r^3\right) + 0.000000132281953\left(T_r^4\right) - 1.7052958E\text{-}10\left(T_r^5\right) \quad (3.1)$$

where T_r is the room temperature and V_r is the equivalent voltage for the room temperature. The temperature of the droplet is determined from a correlation that relates the measured voltage and estimated room temperature voltage as follows:

$$T_i = 0.01978425(V_u + V_r) - 0.0000002001204\left(V_u + V_r\right)^2 + 1.036969E\text{-}11\left(V_u + V_r\right)^3 - 2.549687E\text{-}16\left(V_u + V_r\right)^4 + 3.585153E\text{-}21\left(V_u + V_r\right)^5 \quad (3.2)$$

where V_u is the measured voltage and T_i is the temperature of the droplet during heating or cooling. Data is collected for several channels of equal diameters and the average is used to estimate the measured temperature of the droplet.

Although the thermocapillary pumping could be verified by this experimental process, no post processing can be performed. This necessitated the need for a new design, which incorporates all aspects of the MHE. The design parameters for the new MHE design were based on experimental measurements obtained from the study of the cylindrical channel. The minimum length and width of the rectangular channel were determined from the cylindrical channel.

3.2 Fabrication of MHE

The complete assembly of the MHE is shown in Figure 3.2. Fabrication steps of the MHE are highlighted in Figures 3.3- 3.5. The MHE is fabricated with PZT wafers manufactured by B and H Industries, California. Three sets of wafers of different thicknesses were examined for the fabrication (100μm, 80μm and 60μm). During experimentation, it was discovered that only the sample of 80μm and 100μm could withstand the fabrication rigours. Despite the difficulty in drying the 60μm sample, the vacuum on the spinners distorted the substrate, creating an uneven surface. The substrate eventually failed during the soft bake period of SU-8 as the weight of the photoresist appears to fracture the substrate.

The major equipment used to build the micro heat engine are the IntelVac Nanochrome Deposition System, vacuum spin coaters, vacuum hotplates, photolithography assembly, and Bungard dry film laminator. The equipment is shown in Figures 3.6-3.9. It is important to ensure the highest temperature process is done first during the microfabrication processes, while lower temperature processes are done in descending order. Care must also be taken to show that etching chemical processes are not reactive to deposited metals or photoresist. If a process can attack a layer already patterned on the substrate, a sacrificial layer must be deposited before further processing and removed after processing. The liftoff process appeared most suitable in this research. This involves the deposition of LOR5A beneath the AZ3330 photoresist. LOR5A dissolves in PG remover. By depositing this resist before AZ3330, it creates access for the liftoff process. The fabrication is characterized into 5 major steps:

- Wafer cleaning;

- Fabrication of heaters;
- Back side etching;
- Fabrication of microchannels;
- Sealing of channel.

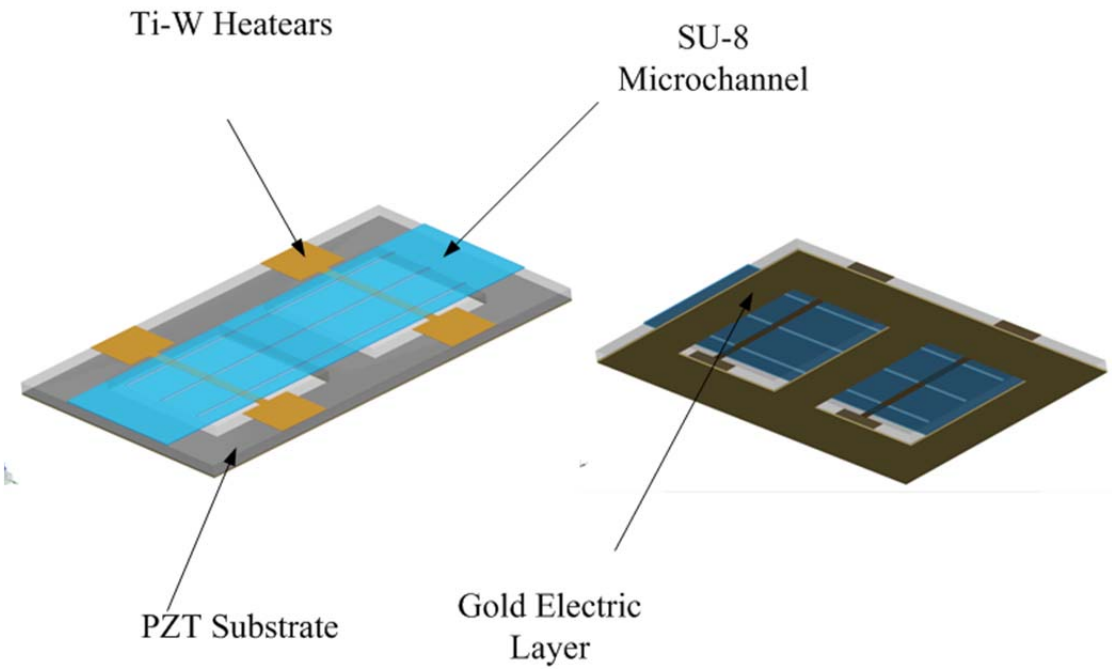

Figure 3.2: Complete micro heat engine assembly

3.2.1 Wafer cleaning

The PZT substrates of different thicknesses were cleaned using an RCA 1 (Radio Corporation of America) cleaning procedure. The cleaning must be done under a fume hood due to the nature of the gases used for the process. Care must also be taken to ensure particles of lead are not inhaled during the cleaning process. The following steps outline the details of the cleaning process.

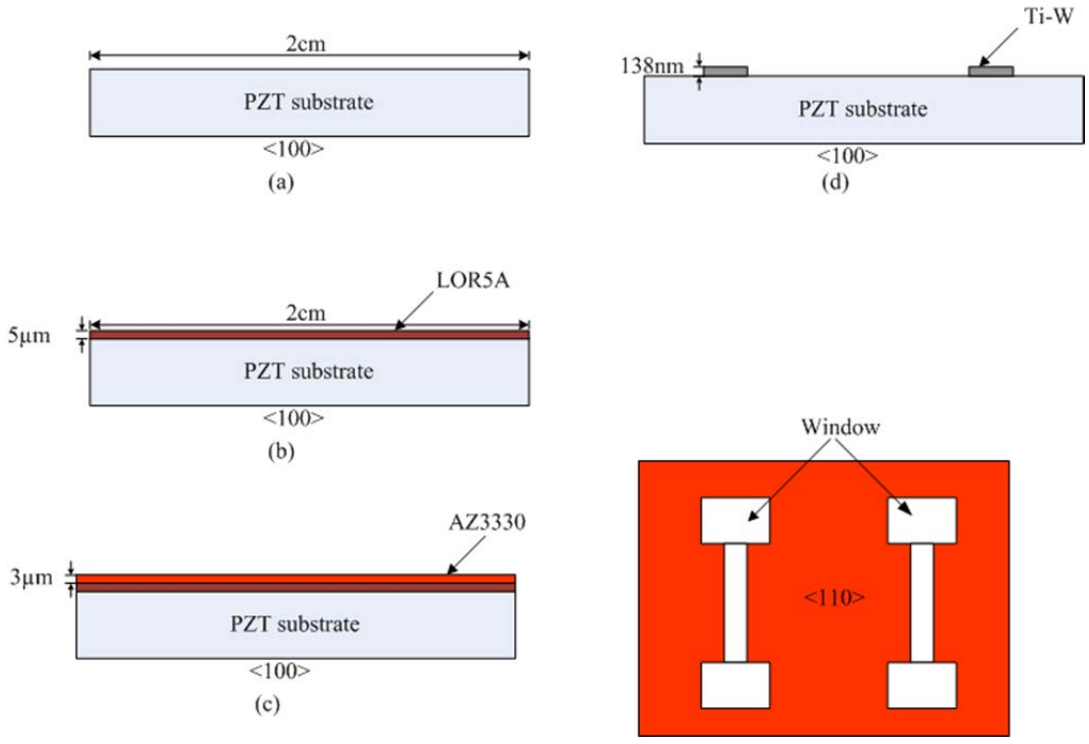

Figure 3.3: Surface micromachining steps for fabrication of Ti-W microheaters using photolithography, sputtering and wet etching

In the process, 650ml of DI-water is dispensed into a beaker and heated on a plate until a temperature of 70^{o}C is attained. Also, 130ml of ammonium hydroxide is dispensed into the beaker of DI-water, while on the hot plate. This can be added at the beginning of the heating cycle. Then 130ml of hydrogen peroxide is added to the mixture of water and ammonium hydroxide, once the required temperature has been achieved (70^{o}C). The resulting solution must be allowed to attain the latter temperature before placing the sample in the beaker. A wafer holder is used to place the samples in the beaker. When processing multiple samples, care must be taken to ensure the sample does not make any physical contact to prevent damage of the surface of the wafer.

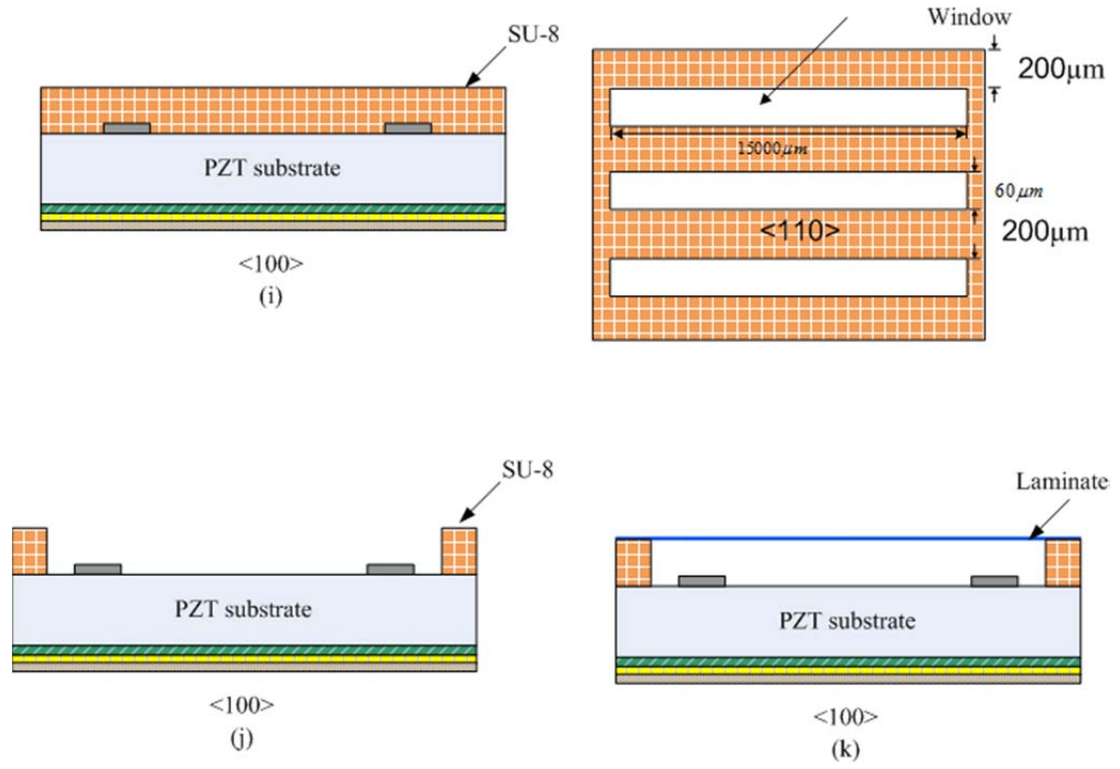

Figure 3.4: Fabrication of SU-8 microchannels using photolithography and sealing of the microchannel using the Bungard dry film laminator

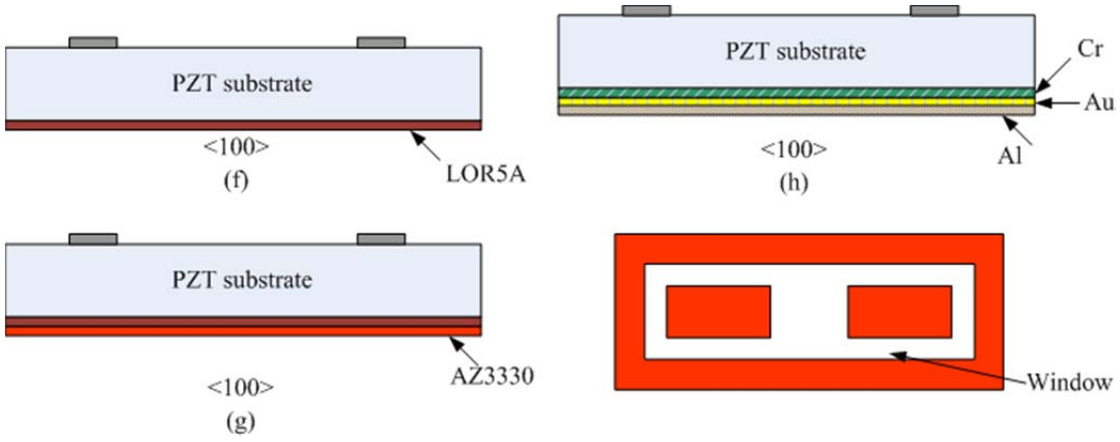

Figure 3.5: Surface micromachining steps for back side of PZT substrate using photolithography, electron vacuum deposition, sputtering, and reactive ion etching

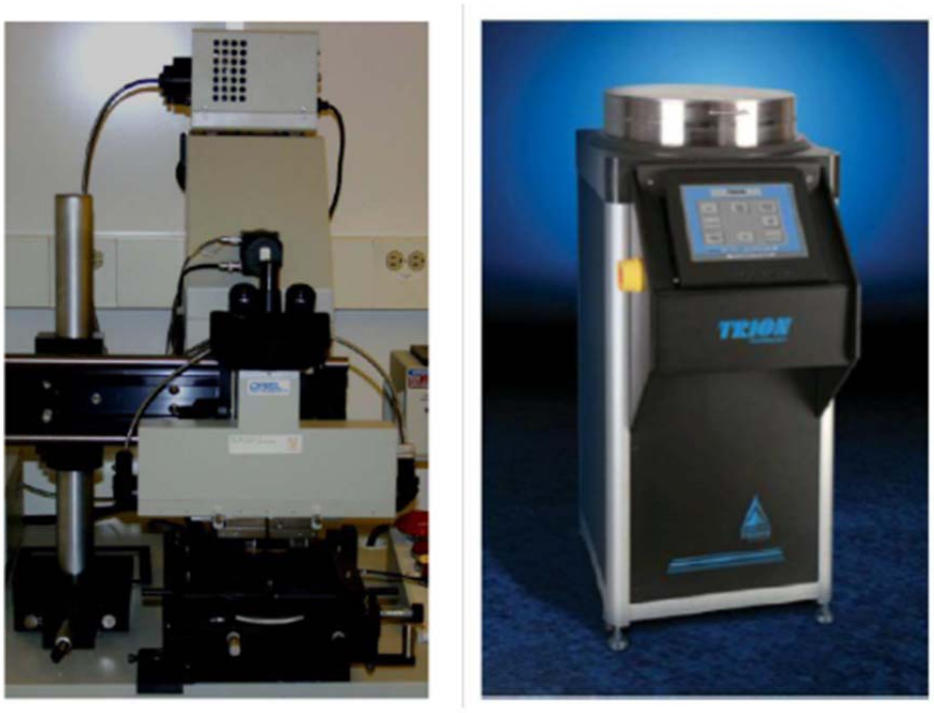

Figure 3.6: (a) UV mask aligner assembly for photolithography; (b) Trion Phantom II Plasma Etcher reactive ion etching

Figure 3.7: a) Vacuum hotplate (b); Spinner and photo resist dispenser

Figure 3.8: IntelVac Nanochrome I for electron beam deposition and DC sputtering

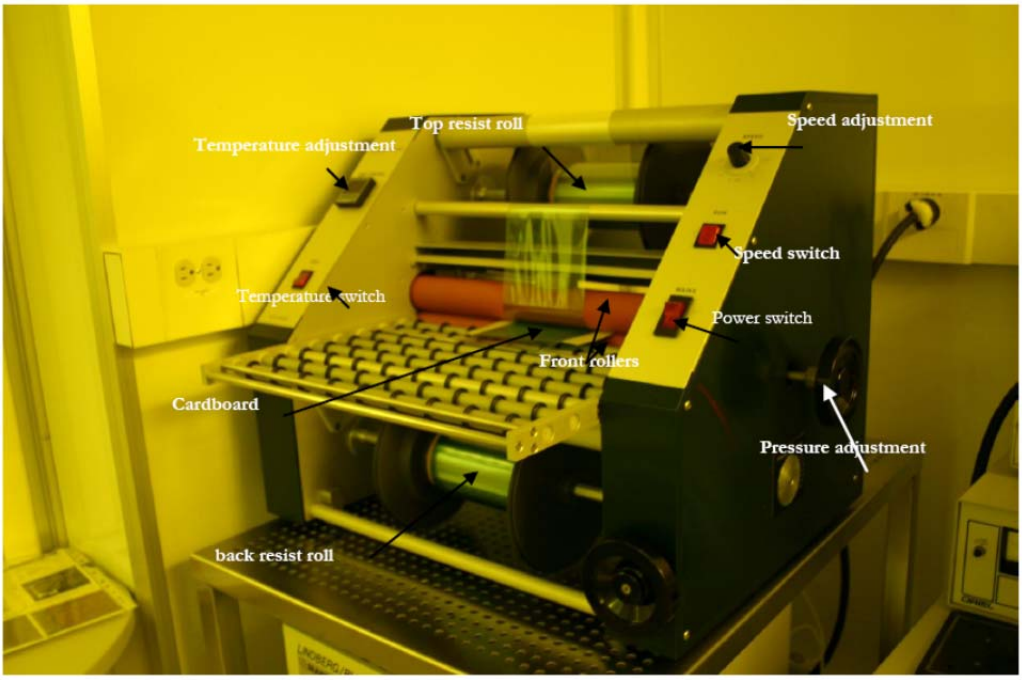

Figure 3.9: Bungard dry film laminator for sealing microchannels

Once the above temperature is reached, the samples are placed in the beaker and allowed to remain in the solution at a constant temperature (70^{o}C) for fifteen minutes. The cleaned substrate is then immersed in a beaker filled with DI-water and allowed to

cool for three minutes. High pressure nitrogen gas is used to dry the substrates, but extreme care must be taken to ensure substrates don't fracture in the process. The sample to be dried is placed on a clean room wipe on a wet bench to avoid any deformation during the drying process.

It is difficult to completely dry the fragile substrate; hence before proceeding to the next step, the substrate should be heated to 120^{o}C for two minutes on the vacuum hot plate and allowed to cool.

3.2.2 Fabrication of microheaters

The heaters were fabricated using Ti-W as the heating element. A combination of photolithography, sputtering, and wet etching are used to fabricate the heater. The sputtering is done in the electron vacuum deposition chamber at 5×10^{-6}Torr. A sacrificial layer is used to outline where Ti-W would be deposited during the sputtering process. AZ3330 positive photoresist from Microchem is used as a sacrificial layer to pattern the heaters. LOR 5A is spin coated on the surface but not developed in order to aid the liftoff process, which is required for the fabrication of the heaters. The best results were obtained when fabrication of the heater is done immediately after the cleaning process. The details of the process are outlined below.

LOR 5A is first dispensed onto the substrate and spin coated at 500rpm for 5s and 3000rpm for 45s. This process is done in one spin cycle. The acceleration must be ramped to 10,000rpm/s to ensure an even distribution of the photoresist on the substrate. A thin layer of about 500nm is formed based on the spin speed. The substrate is then soft

baked for two minutes at 160^{o}C. No exposure or development is required as it is just a sacrificial layer. The substrate in then allowed to cool naturally for about five minutes.

AZ 3330 is deposited onto the cooled substrate and spin-coated at 500rpm for 15s and 4000rpm for 45s in one spin cycle. It is recommended to wait for 30s before initiating the spin process after deposition to ensure even distribution of the photoresist and dispersion of possible bubbles during the dispensing process. A thin film of about 3μm is formed for a spin speed of 4000rpm.

The substrate is soft baked at 90^{o}C for five minutes on a vacuum hotplate and allowed to cool before exposure. The exposure is done with a 365nm-UV wavelength mask aligner (Ultraviolet Illumination System (350 – 450nm) - Model 87000) for 14s. The post exposure baking (PEB) of substrate is then performed at 110^{o}C for three minutes on the vacuum hotplate. The substrate must be cooled before developing the pattern. The development is done using AZ's MIF 3000 developer solution. This development is carried out for 300s. This was the optimal time that gave the best results. This was an important discovery, because the manufacturer's recommended time for development was only 60s. If development is done for only 60s during the liftoff process, the deposited metal is removed along with the resist. The longer development time ensured that LOR5A was completely removed from the patterned surface and allowed the metal to be deposited directly unto the substrate. The development time of 300s is only applicable to the PZT substrate. During initial trials on microscope slides, the development time was about 120s.

The developed substrate is hard baked on the hotplate for two minutes at 110^{o}C and allowed to cool before it is inspected under the microscope. The finished pattern is shown in Figure 3.10.

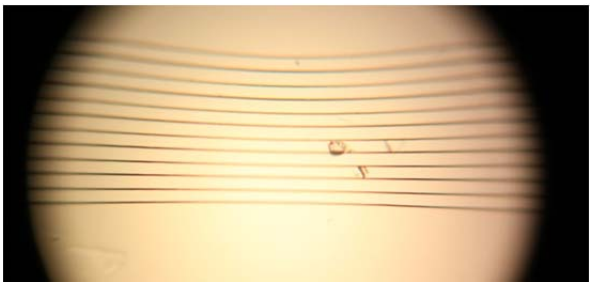

Figure 3.10: Patterning of microheater using LOR 5A/AZ3330 viewed at × 5 magnification with the Reichert Austria stereo microscope

The IntelVac Nanochrome deposition system is used for the sputtering process in a high pressure vacuum chamber. The equipment can be used for sputtering several metals. The metal of interest at this stage of the process required a Ti-W target to be installed in the chamber. The sputtering vacuum chamber is vented to allow for a change of target and inserting the specimen in the chamber. An aluminum holder is required beneath the target to prevent a short circuit between the permanent magnet and the target. A thin layer of paste is required on the cathode to fill the microscopic voids between the target and cathode block.

The chamber is pumped down to the process pressure (5 x 10^{-6}Torr). The sputtering then commences at a rate of 23Angstroms (Å) per minute. Ti-W is sputtered for about sixty minutes to provide a film thickness of about 138nm. This process must be carefully controlled using an Argon flow rate of 20sccm and power of 50W in order to get a uniform deposition. Increasing the power can help reduce the time required for the

deposition, but it was discovered that this leads to excessive internal stresses, which affect the adhesion of Ti-W to the substrate.

The chamber is then allowed to cool for 15 minutes before the samples are removed and inspected under the microscope. The liftoff process should be done immediately after sputtering to prevent oxidation of Ti-W. Two methods were investigated for the liftoff process. The liftoff could either be done by using a heated bath of PG remover or by using PG remover in an ultrasonic bath. The latter process is recommended as the processing time is reduced, hence it is the preferred method for this process. The ultrasonic bath is heated to a temperature of 38^{o}C and the power setting is fixed at 3 Watts.

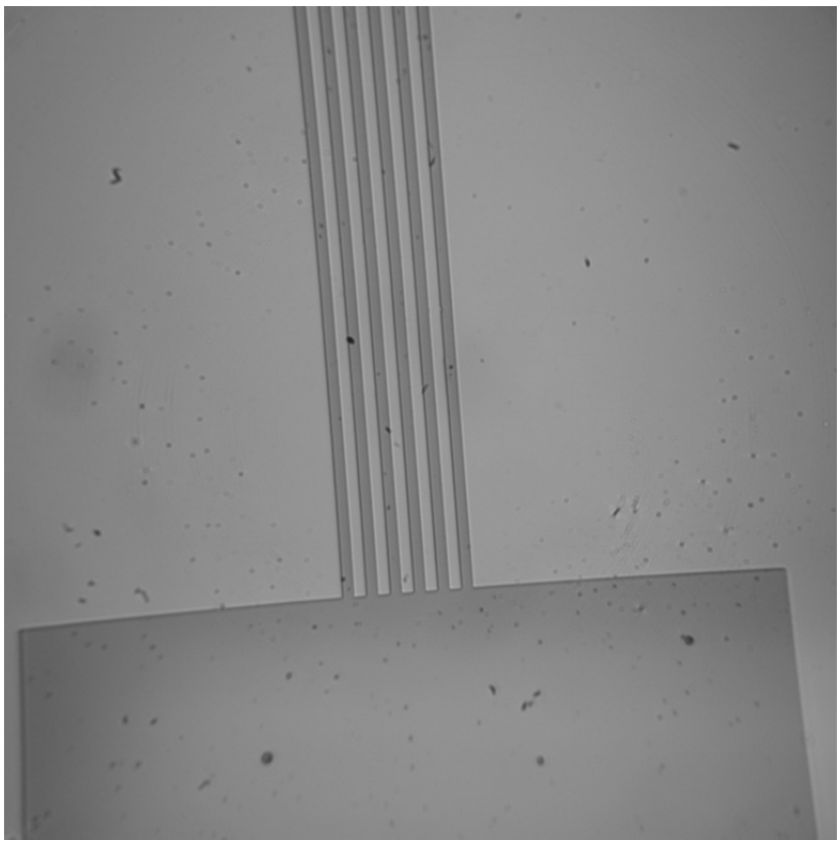

Figure 3.11: Fabricated Ti-W microheaters

The time for the liftoff varied between twenty and forty minutes. The strength of adhesion is suspected to be the reason for the variance in liftoff time. Substrates may collect some dirt before the sputtering process, which could alter the adhesion property.

Once the entire LOR5A/AZ3330 layer is visibly off the substrate, the sample is placed in a fresh beaker of isopropyl alcohol (IPA) to remove any traces of PG remover that might be left on the sample. The sample is allowed to remain in the solution for three minutes before it is dried by nitrogen gas. Further heating may be required to remove any traces of IPA from the surface. This is done on the vacuum hotplate at 120^{o}C for two minutes. The heater can then be inspected under the microscope before further processing. Figure 3.11 shows the completed Ti-W heaters.

3.2.3 Back side etching

The back of the substrate must be etched to allow for flexing of the piezoelectric. The etching pattern also creates packaging support for the microassembly. The back of the substrate is processed using photolithography, sputtering and reactive ion etching (RIE). Three metals are deposited during this process (chrome [Cr], gold [Au], and aluminum [Al]). Chrome acts as an adhesion layer and dielectric layer for the gold deposition. Gold acts as the electric layer, which allows for external connection to the required load. Aluminum acts as a mask for the reactive ion etching process. The steps to achieve the desired results are listed as follows.

LOR 5A is spin coated on the substrate using a similar technique as outlined in section 3.2.2. This thin layer is also used to aid the liftoff process. AZ3330 is also deposited as a sacrificial layer for the deposition of Cr, Au and Al. The process is the

same as outlined in section 3.2.2. The IntelVac Nanochrome deposition system is capable of performing the DC sputtering and electron beam deposition simultaneously. The chamber is vented to allow loading of the Al target and filling of holders for Au and Cr with their respective crucibles for the deposition process. Then 300Å of Cr is deposited using the electron beam deposition, after which 500Å of Au is then deposited using a similar procedure. Al is deposited at 180Å per minute for thirty minutes. The chamber is then allowed to cool for fifteen minutes before it is vented and the samples are inspected under the microscope to ensure even deposition.

The liftoff process is required to expose the portion of the substrate to be etched by the RIE process. The liftoff process is carried out under similar conditions as outlined in section 3.2.2. In order to protect the Ti-W heaters from the RIE process, AZ3330 is spin coated on the front side of the substrate to act as a masking layer. AZ3330 is then deposited using the spinners at 500rpm for 15s and 4000rpm for 45s in one spin cycle. The substrate is then soft baked at 90^{o}C for five minutes. No exposure or development is required since the layer is only used to mask the substrate from the plasma during the RIE process.

RIE is a combination of ion and plasma etching. The selective etching of the surface occurs as a result of a chemical reaction between the surface layer and the chemically reactive plasma. Trion Phantom II plasma etcher is used to carry out the etching for this experiment. The sample is suspended in the chamber in order to produce the isotropic etching finish. The parameters used in the present study are listed as follows:

- Inductive coupled plasma (ICP) power 250W
- Radio frequency (RF) power 200W

- Argon (Ar) flow rate 50Sccm
- Sulphur hexafluoride (SF_6) flow rate 5Sccm
- Etching pressure 50mTorr
- Time 1,080s

3.2.4 Fabrication of microchannels

SU-8 is a negative photoresist, which can be used to produce micro structures of large thicknesses in the order of 25-150µm. SU-8 2025 can produce structures with thicknesses between 25 and 40µm while SU-8 2075 can produces thicknesses between 60 and 240µm. The thickness is dependent on the spin speed. SU-8 has an excellent imaging capability and also thermally stable. This photoresist produces structures with very good vertical walls with a high aspect ratio. Once formed, it cannot be easily dissolved in most organic solvents. In most structures produced with SU-8, hard baking is not required because of its structural stability. The process for processing of SU-8 during this experiment is outlined below.

If the sample is processed immediately after the etching process, it should be allowed to cool before being processed. It is a good practice to rinse the specimen in IPA and subsequently perform drying before beginning the patterning process. If a sample is allowed to stay overnight, the substrate must be heated at 120^{o}C for two minutes before patterning the channels. SU-8 is sensitive to moisture, which affects its adhesion to the surface.

Photolithography is used to process SU-8. The design of the chrome mask for patterning SU-8 is shown in Figure 3.12. The mask design is based on experimental

measurement of droplet width and diameter observed from the cylindrical microchannels fabricated from capillary tubes. The minimum achievable width in the cylindrical microchannels is 16μm while the length was about 1200μm. The minimum design width for the rectangular microchannel is 40μm. This ensures the properly exposed during photolithography, as the UV-Mask aligner requires a minimum tolerance of 15μm for complete exposure. SU-8 is deposited on the substrate and spin coated using the following optimal parameters in one spin cycle:

- 500rpm for 10s with an acceleration of 162m/s^2;
- 2000rpm for 15s with an acceleration of 468m/s^2;
- 4000rpm for 20s acceleration of 468m/s^2.

Edge ridges are always observed after the spin cycle. A knife edge is used to remove the ridges from all sides of the substrate. If the ridges are not removed, uneven exposure will occur, as an air gap will be trapped between the substrate and the chrome mask in the vacuum seal of the mask aligner.

Soft baking is done in two steps for both types of SU-8. The baking time for SU-8 2025 is two minutes at 65^{o}C and five minutes at 95^{o}C, while the baking time for SU-8 2075 is three minutes at 65^{o}C and seven minutes at 95^{o}C. After the baking is completed, the sample should be suspended in air for one minute before being placed on clean wipes on the work bench and allowed to cool naturally. This is necessary to avoid cracks at the edges of the microchannel, which occur as a result of rapid cooling of the substrate. The exposure time for SU-8 using the UV mask aligner is 240s. It is recommended to break

the exposure into 4 cycles of 60s each to reduce the amount of heat absorbed as a result of the UV exposure. This will also prolong the life cycle of the UV lamp.

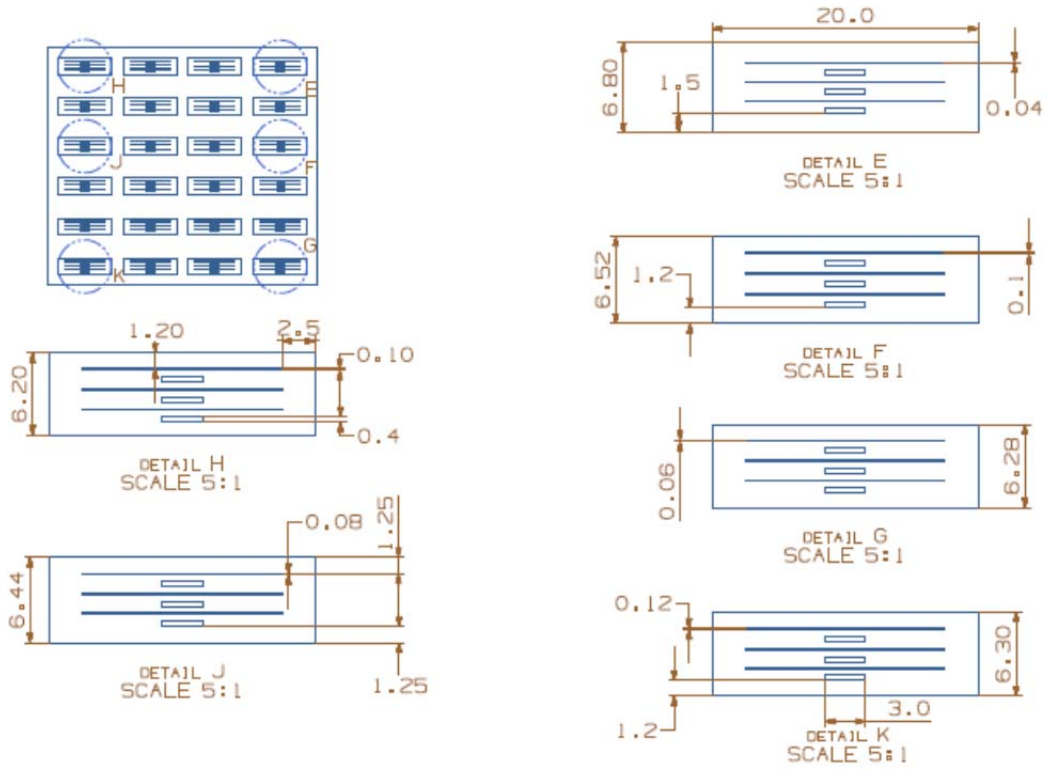

Figure 3.12: Design of 4 × 4 inch chrome mask for photolithography of microchannels (40, 60, 80,100,120 and 140µm widths and 1500µm lengths)

The microscope on the mask aligner is used to ensure that the channels are formed perpendicular to the Ti-W heaters and the electrical contact points of the heater are not covered by the resist.

Once the exposure is complete, the post exposure baking can be commenced. SU-8 2025 is post baked in two steps, one minute at 65^{o}C and five minutes at 95^{o}C. SU-8 2075 is baked for two minutes at 65^{o}C and seven minutes at 95^{o}C. The substrate must also be suspended in air for one minute before it is placed on the clean wipes on the work bench. Development is done after the sample is cooled. SU-8 Developer form Microchem is

used to process the pattern after post exposure baking. A Developer solution is dispensed in a beaker and filled to ensure that the entire substrate is immersed in the solution. The substrate is firmly placed on a wafer holder to ensure no slippage during agitation. Strong agitation is required for development of SU-8 and must be done throughout the development period. Agitation of the sample must be done in the same sequence to ensure even development. Forward and backward stroke movement was chosen for this experiment. The optimal development time for SU-8 2025 is four minutes, while that of SU-8 2075 is six minutes.

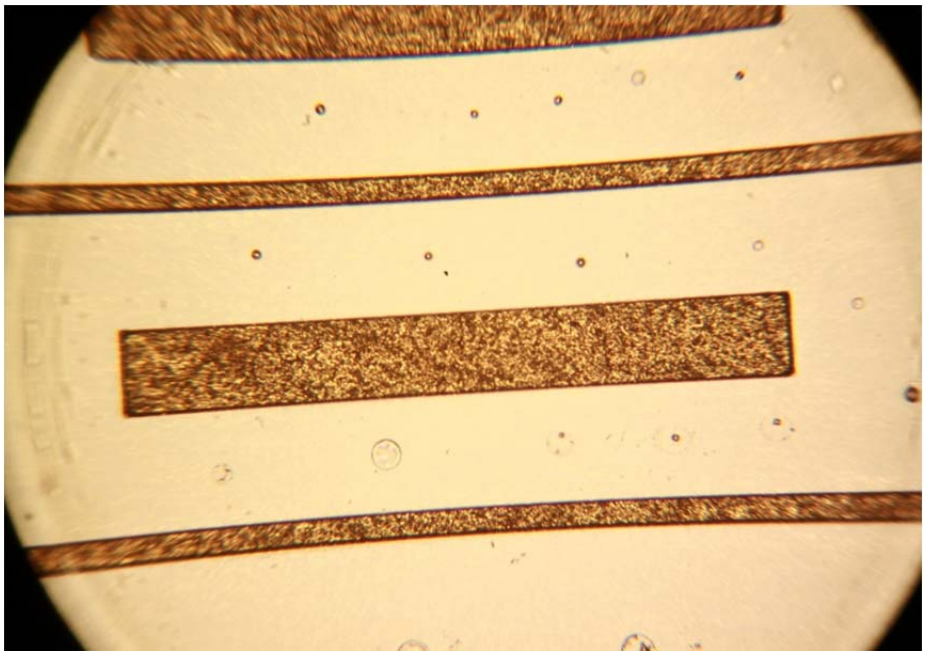

Figure 3.13: Fabricated SU-8 2075 microchannel viewed at × 5 magnification of a Reichert Austria stereo microscope

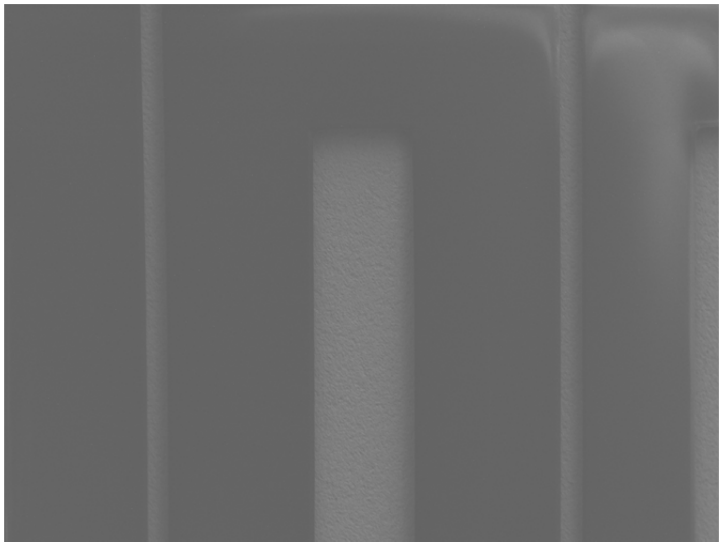

Figure 3.14: Fabricated SU-8 2075 microchannel viewed under a Hitachi 3000 scanning electron microscope

The sample is then immersed in a solution of IPA for three minutes to remove any trace of the developer that might be left on the substrate. High pressure nitrogen gas is used to dry the substrate. The fabricated channel can then be inspected under a microscope. Figures 3.13 and 3.14 show the fabricated microchannel. If any sign of underdevelopment is observed, the previous step can be repeated in intervals of 10s and inspected each time, until a desired pattern is achieved. Care must be taken to avoid undercuts. Over development leads to undercuts in the microchannel.

3.2.5 Sealing of microchannel

Bungard dry film laminator is used to seal the channel and secure the droplet within the channel. The laminator is designed to laminate both sides of the substrate with a thin film photoresist of about 17μm. The thickness of the photoresist cannot be precisely controlled. No patterning was required for the purpose of this experiment. The laminate was left for about five days to ensure proper adhesion to the substrate. Although the photoresist can be heated for immediate adhesion, the droplet will react with the film

during the heating process, leading to an uneven surface. The process followed during this experiment is outlined below.

A Hamilton micro syringe is used to place the droplet on top of the channel. The hydrophobic property of DI-water on SU-8 keeps the water in the required location before the lamination process.

The Bungard laminator is used to force the water droplet into the channel and seal the channel. The laminator is set to a temperature of 95^{o}C and a pressure of 2bar with a roller speed of 0.5m/s. The substrate is placed on a clean room sheet to avoid the lamination of the backside of the substrate and prevent sticking of the roller. Thin strips of clean room paper are placed along the heater on top of the substrate to prevent lamination of the electrical contact points. The completed assembly is allowed to remain in the photolithography room for five days before the protective covering of the laminate is removed. The substrate cannot be allowed to have exposure to the visible light spectrum before the adhesion is complete, as this will alter the properties of the thin film.

The completed microchannel assembly can then be inspected under the microscope. It is expected that the droplet will remain in the channel. However, after several experiments, this could not be achieved. The microchannel was developed without sealing the top of the channel and observed under the microscope. The experiment revealed that the droplet evaporated within 15s of being deposited in the microchannel without any heat addition. This showed that the droplet vaporized before the substrate went through the rollers, which was kept at 95^{o}C. The reason for evaporation of the droplet became an important phenomenon to understand. Subsequent sections of this

thesis will give new insight into the evaporation of a droplet in a closed rectangular microchannel.

3.3 Experimental measurements and uncertainty

Experimental measurements were carried out on three test benches. The first test bench, outlined in section 3.1, was used to observe the displacement of the droplet in a cylindrical microchannel. The second test bench was used to measure the power output of the Ti-W heaters, which were used to supply heat to the MHE. The third test bench was used to observe the droplet evaporation and de-pinning in the rectangular microchannel. The uncertainties with measurements acquired from all three test benches are outlined in this section. Two methods were used to estimate the uncertainties associated with the experimental measurements. Kline and McClintock's [171] method was used for estimating the uncertainties of the power and evaporation process. The ASME standard of uncertainty was used to estimate the estimate the uncertainty in measuring the displacement of the droplet in the cylindrical channel.

3.3.1 Power supply measurement and uncertainty

The voltage and current supplied to the heater were measured by four point probe method. The electrical circuit of the four point probe method is shown in Figure 3.15. A resistance of known value is connected across the direct current (DC) power supply and the current is measured using a DC multimeter. This method is used to determine the current flowing through the resistor (1kΩ) as the voltage is regulated. The resistor and Ti-W heater are connected in series, which means the same amount of current is flowing through the heater and resistor. A second DC voltmeter is connected across the Ti-W

heater to measure the voltage generated. The power output from the heater can be estimated from the measured voltage and sheet resistance across the Ti-W heater.

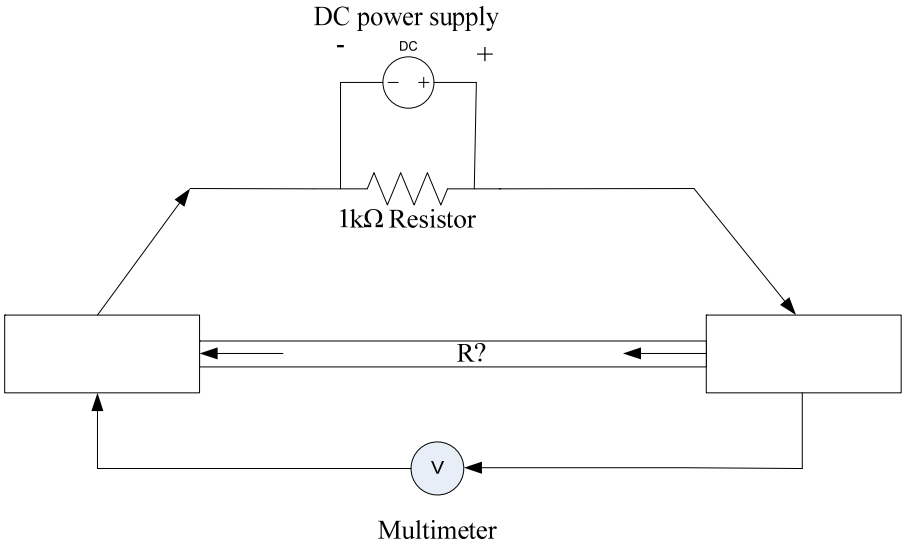

Figure 3.15: Electrical layout of four point probe test to measure the sheet resistance and voltage output of the microheaters

The droplet is observed under a microscope mounted on top of the probe station and a high speed video camera is used to record the motion of the droplet. The substrate in held in position by a vacuum chuck to ensure that no vibrations occur during the voltage measurement. The probe needles are positioned on the contact pads with the aid of a microscope and a stage control mechanism of the probe station. Extreme caution must be taken to ensure the two probes on each pad make no physical contact, as this will sort circuit the device and burn the heater, resulting in an open circuit. The probe station can accommodate a third set of probes, which could be used to measure the voltage generated from the flexing of the piezoelectric membrane.

The uncertainty of the measurement is done in accordance with Kline and McClintock [171] method of estimating the uncertainty in a single sample experiment. This method was used to analyse the voltage and current measured across the heaters.

The measurement of interest is the power output (q), which is a product of the voltage and current (q= VI). The uncertainty associated with measuring the power output can be determined using the following correlation:

$$U_q = \left[\left(\frac{\partial q}{\partial V} e_v \right)^2 + \left(\frac{\partial q}{\partial I} e_i \right)^2 \right]^{1/2} \tag{3.3}$$

Where U_q, is the uncertainty of the single sample measurement and e_v, e_i are the uncertainties associated with measuring the voltage and current, respectively. The calculated uncertainty of the experiment varied between 1 and 5% for the range of data considered in this study. The DC multimeter used to acquire the voltage and current is capable of detecting a current fluctuation on the order of 1×10^{-4}mA, which explains the high accuracy of the data collected.

3.3.2 Evaporation measurement and uncertainty

A 10µl syringe was used to dispense the droplet into the microchannel with the aid of a Reichert Austria stereo microscope in the experimental measurements. A digital video recorder is mounted on the viewing port of the microscope. The images were recorded at a frequency that varied between 25 and 32 frames per second (fps). The DI-water samples were measured mostly at 25fps because the evaporation occurred slower than toluene. The images were measured under two magnification settings (× 5 and × 10), although the microscope had the capability of measuring a magnification of × 150. The

entire width of the channel could only be captured by the digital camera under the latter two settings. The evaporation and de-pinning processes of the droplet were recorded using Stream Pix III imaging software, which allows for digitization and characterisation of the images.

The contact angle, droplet width, and pinning radius can all be measured over time. A UTHSCSA image tool developed by the University of Texas Health Science Center in San Antonio was used to measure pixel displacement and contact angle over the evaporation and de-pinning periods. The imaging tool also reported the mean and standard deviation of the measurements. This standard deviation was used to estimate the uncertainty of the data recorded.

The uncertainty of the measurements was obtained by the Kline and McClintock method [171]. The displacement is a product of the measured width of the channel and the number of pixels ($L = P_i W$). In this case, the independent variables were width and pixels. The uncertainty can be estimated as follows:

$$U_L = \left[\left(\frac{\partial L}{\partial P_i} e_{p_i} \right)^2 + \left(\frac{\partial L}{\partial W} e_w \right)^2 \right]^{1/2} \tag{3.4}$$

where U_L is the uncertainty in a single measurement of the length and e_{p_i}, e_w are the uncertainties associated with measuring the pixel and width, respectively. The uncertainty associated with measuring the evaporation width was estimated to be between 1 and 11% for the number of experiments considered in this study. The uncertainty associated with the de-pinning process varied between 1 and 5%. Although some of the data points for

the evaporation uncertainty measurements fall outside of the confidence interval of 10%, the single sample uncertainty measurement allows this set of data to be discarded during the analysis of the experimental data.

The uncertainty in the time measurement is a function of the frame rate and number of frames. The time *t* is estimated as

$$t = F_N \left(F_R\right)^{-1} \tag{3.5}$$

The uncertainty in measuring time for a single sample can be expressed as

$$U_t = \left[\left(\frac{\partial t}{\partial F_N} e_{F_N}\right)^2 + \left(\frac{\partial t}{\partial F_R} e_{F_R}\right)^2\right]^{1/2} \tag{3.6}$$

where e_{F_N} , e_{F_R} are the uncertainties in measuring the frame number and frame rate, respectively. The uncertainty of the time measurement was found to be about 1%, which is very reliable for analysing the experimental data. The high accuracy is expected as the Stream Pix acquires the images at +/-0.0001 frame rates per second.

3.3.3 Uncertainty of measurement in droplet displacement

The measurement uncertainties were estimated based on a method described by Abernethy *et al.* [172] as more data was available about the precision and bias errors of the devices used for the measurements. The precision and bias errors were obtained for the multimeter (used to measure current flowing to the heater), data acquisition board (for measuring voltage readings from thermocouples), digital calliper (used for measuring the diameter of the microchannel) and the measured voltage from a thermocouple. The

precision error for the measured data is estimated as a function of its standard deviation as follows [172]:

$$U_{P_{measured}} = \frac{S_D}{\sqrt{N}} \tag{3.7}$$

The bias error is a measure of deviation from the mean. This error remains constant throughout the experiment. From observations of the measured data, the mode of deviation from the mean is assumed for the bias error. The precision and bias errors for the devices are obtained from the equipment manufacturers [173-175]. The precision and bias errors of the equipment and measured data are shown in Table 3.1. The total precision error is estimated by:

$$U_p = \sqrt{U_{P_{measured}}^2 + U_{P_{NI}}^2 + U_{P_{DM}}^2 + U_{P_{MM}}^2} \tag{3.8}$$

Similarly the total bias error is obtained by:

$$U_B = \sqrt{U_{B_{measured}}^2 + U_{B_{NI}}^2 + U_{B_{DM}}^2 + U_{B_{MM}}^2} \tag{3.9}$$

The total uncertainty is obtained from the combination of precision and bias errors,

$$U = \sqrt{U_p^2 + U_b^2} \tag{3.10}$$

Table 3.1: Precision and bias errors of experimental temperature measurements

Variables	Precision Error	Bias Error
Voltage readings from thermocouple	1.16μV	25.6μV
Diameter of microchannel	0.5	1μm
Multi-meter (current flow to heater)	0.1mA	0.275 mA

The resulting error in the temperature measurement is estimated to be ± 1.4^{o}C, which is within a 95% confidence interval. The uncertainty for the measured

displacement is a function of the precision of the digital camera used to acquire the image and the error from the image digitization.

Chapter 4 : Entropy generation in electrochemical processes

A new predictive model of entropy production for the electrochemical processes is presented in this chapter. This related to an overall goal of this thesis to develop new predictive tools for Second Law analysis, particularly models to predict entropy generation in electrochemical and microfluidic processes. The effects of temperature and current density on entropy production are investigated with the new formulation. A comparative study is performed with respect to the relationships between current density and overpotential, using Tafel's equation and the newly proposed method, based on the Nernst equation.

4.1 Entropy production in an electrolytic cell

Consider an electrochemical process involving electrolysis of CuCl/HCl to produce hydrogen in Figure 4.1. The electrical circuit is completed by a resistor, ammeter and dc voltage source connected by external wiring from one electrode to another [176]. The electrochemical reaction in the cell can be treated as two half-cell reactions, since the electrochemical reactions occur in two different sections of the cell, i.e., anode and cathode, respectively. In the electrolytic cell, a positive potential is used to drive the reaction in the anodic direction, while a negative potential will drive it towards the cathodic direction. This makes the anode the positive electrode in an electrolytic cell, while the negative electrode is regarded as the cathode. It is assumed that CuCl is supplied continuously to the anode, while HCl is supplied to the cathode. The working electrode is assumed to be platinum (Pt) on a gas diffusion layer (GDL). The electrolyte

used on the anode side of the cell is a mixture of HCl and CuCl, while HCl is adopted on the cathode side.

The reactions are classified as anodic and cathodic reactions. The anodic half-cell reaction for the oxidation of copper (I) to copper (II) can be represented as:

$$2CuCl + 2HCl \rightarrow 2CuCl_2 + 2H^+ + 2e^- \quad (4.1)$$

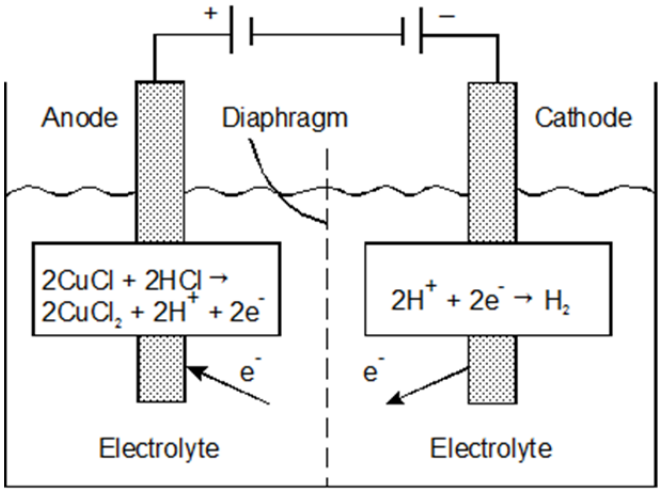

Figure 4.1: Schematic of the electrochemical cell

Similarly, the cathodic half-cell reaction for the reduction of hydrogen protons to hydrogen gas is represented as

$$2H^+ + 2e^- \rightarrow H_2 \quad (4.2)$$

Although both reactions occur separately, they can be combined as one reaction, based on the principles of conservation of charge and electron neutrality [176]. As a result, the overall cell reaction can be written as

$$2CuCl + 2HCl \rightarrow 2CuCl_2 + H_2 \quad (4.3)$$

Introducing an electric field across the electrolyte generates a driving force for the ions dissolved in it. While electrons flow through the electrode, as a result of the applied

current, ions in the electrolyte migrate as a result of diffusive and convective modes of transport. The net flow of ions will be the sum of migrations due to diffusion and convection.

4.1.1 Formulation of voltage losses and mass transfer irreversibility

All overpotentials represent irreversiblities in the system. In an electrolytic cell, more power must be supplied to overcome these irreversibilities, thereby making the actual cell potential greater than the open circuit potential. Alternatively, these irreversibilities are also a consequence of polarization. This is an effect of passing current through an electrolytic cell to make it depart from equilibrium. The magnitude of the decrease in potential from equilibrium is called the overpotential (η_v).

The voltage loss in electrolytic cells includes the activation, ohmic and the concentration (surface) overpotential. Activation and ohmic losses are known to significantly affect the voltage losses across the cell, and hence they should be included in design considerations for the electrolytic cell. The activation losses can be interpreted as the voltage required in overcoming the open circuit voltage of the cell, when no load is connected in the circuit. Ohmic losses occur as a result of the internal resistance of the cell.

The maximum power output of the cell is determined from the change in Gibbs free energy, which is expressed as

$$\Delta G = \Delta H - T\Delta S \tag{4.4}$$

The potential at zero current flow is known as the reversible open circuit voltage (ROCV) across the cell, which can be determined from the relationship between the Gibbs free energy and the electrical work as follows,

$$ROCV = \frac{-\Delta G}{ZF_c} \tag{4.5}$$

where Z is the number of electrons transferred and F_c is Faraday's constant. The deviation of electrode potential from the reversible open circuit voltage is

$$\eta_v = ROCV - \left(V_{ohmic} + V_{activation} + V_{conc}\right) \tag{4.6}$$

4.1.2 Surface overpotential

The driving force in the electrochemical reaction at the electrode of the cell is the surface or concentration overpotential. The rate of reaction can be related to the surface irreversibilities by the Butler-Volmer equation [176]:

$$i = i_o\left[\exp\left(\frac{\alpha_{an}F_c}{RT}V_{conc}\right) - \exp\left(\frac{\alpha_{cl}F}{RT}V_{conc}\right)\right] \tag{4.7}$$

where i is the current density, i_o is the exchange current density, and α is the charge transfer coefficient that varies between 0.1 and 0.5. Equation (4.7) will be approximated at low surface overpotentials using Tafel's model [177] to yield:

$$i = i_o\frac{\left(\alpha_{an} + \alpha_b\right)F_c}{RT}V_{conc} \tag{4.8}$$

The voltage loss (V_{conc}) can then be expressed as

$$V_{conc} = -\left\{\frac{2.303RT}{\left(1-\alpha\right)ZF_c}\right\}\log_{10} i_o + \left\{\frac{2.303RT}{\left(1-\alpha\right)ZF_c}\right\}\log_{10} i \tag{4.9}$$

4.1.3 Ohmic overpotential

Resistance to the flow of ions in the electrolyte, combined with resistance to the flow of electrons through the electrode, then constitutes the ohmic losses. These losses

are considerably higher for high temperature cells, however the cell operates at ambient temperature. The total ohmic resistance is the sum of components from the electrolyte, cathode and anode.

$$V_{ohmic} = i\left(r_{elect} + r_{an} + r_{ct}\right) \tag{4.10}$$

The resistance from the electrolyte is much larger than other terms for the anode and cathode, so only mass transfer within the electrolyte will be considered hereafter.

Consider 1-D mass diffusion within the electrolyte, with $x = 0$ at the edge of the electrolyte. The ohmic resistance can be expressed as follows,

$$V_{ohmic} = i\int_0^{l_e} \frac{dx}{\sigma_e(x)} \tag{4.11}$$

where σ_e refers to the electrolyte conductivity, which can be calculated from

$$\sigma_e(x) = \sigma_{e0}\frac{C_l(x)}{C_{H^+}} \tag{4.12}$$

where C_l is the molar concentration of cuprous chloride (mol/cm^3), C_{H+} is the molar concentration of protons (mol/cm^3) and σ_{e0} is the electrolyte conductivity at unit cuprous chloride content. From Fick's Law [145, 178], the electro-osmotic flux can be determined from

$$D_{AB_e}\frac{dC_l}{dx} = n_d\frac{i}{F_c} \tag{4.13}$$

where n_d is the electro-osmotic drag coefficient. Integrating equation (4.13) over the thickness of the electrolyte yields

$$\int_{C_{l,a}}^{C_{l,c}} dC_l = \int_0^{l_e} \frac{n_d i}{D_{AB_e} F_c} dx \tag{4.14}$$

which becomes

$$C_{l,an} = C_{l,ct} - \frac{n_d i}{D_{AB_e} F_c} l_e \tag{4.15}$$

The result in equation (4.15) represents a molar concentration at the anode/electrolyte interface. Since the diffusive flux is proportional to the molar concentration, Ohm's law requires that the molar concentration increases linearly across the membrane [145], from the previous result in equation (4.15) at the anode to $C_{l,c}$ at the cathode. Therefore,

$$C_l(x) = \frac{n_d i}{D_{AB_e} F_c} x + \left(C_{l,ct} - \frac{n_d l_e i}{D_{AB_e} F_c} \right) \tag{4.16}$$

Alternatively,

$$C_l(x) = C_{l,ct} \left[1 + \frac{i}{i_L} \cdot \left(\frac{x}{l_e} - 1 \right) \right] \tag{4.17}$$

where

$$i_L = \frac{F_c D_{AB_e} C_{l,ct}}{n_d l_e} \tag{4.18}$$

It can be observed that $C_l(0) = 0$ when $i = i_L$. This case of $i = i_L$ represents the limiting current within the electrochemical cell. Substituting equation (4.18) into equation (4.11) gives

$$V_{ohmic} = i\int_0^{l_e}\left[\frac{C_{H^+}}{C_{l,ct}}\Big/\left(1+\frac{i}{i_L}\left(\frac{x}{l_e}-1\right)\right)\right]dx \tag{4.19}$$

which may be integrated and expressed in terms of an empirical coefficient, $r_{elect} = 30\times10^{-6}\,k\Omega cm^2$ [179] to give the following ohmic loss,

$$V_{ohmic} = ir_{elect} \tag{4.20}$$

Diffusion of the electrolyte can be verified using Cottrell's equation [177],

$$i_d(t) = \frac{nF_c AD_{AB_o}^{1/2} C_o}{\pi^{1/2} t^{1/2}} \tag{4.21}$$

where C_o is the bulk concentration, D_{ABo} is the diffusion coefficient and equation (4.21) is used to check if the electron transfer is as result of mass transfer of the electrolyte. Experimental observations are yet to predict the diffusion coefficient for the electrochemical reaction.

4.1.4 Activation overpotential

Activation losses occur due to energy required to start the reaction in the electrolytic cell. Using a good catalyst such as platinum will reduce the activation overpotential. However, platinum is expensive and makes the overall system cost prohibitive. Considerable research is underway to find alternative lower-cost catalysts to make the process more commercially viable. Nernst's equation will be used to estimate the activation potential of the electrolytic cell. The Nernst equation can be used to analyze this cell since it was assumed that the electrolyte will be constantly supplied to the cell. This will make the reactant concentrations much lower than the electrolyte, essentially making the electrolyte uniform in concentration throughout the

electrochemical reaction. Also, since the reaction is relatively fast and reversible, the use of the Nernst equation can be justified in this study. The activation losses are higher at low temperatures, hence a more significant effect on the total voltage loss will be observed. The liquid junction potential and ionic activity coefficient are neglected when writing the Nernst, equation owing to their interdependent relation on the nature of the reacting spices:

$$V_{activation} = \frac{RT}{Z\alpha F_c}\ln\left(\frac{i}{i_o}\right) \tag{4.22}$$

4.1.5 Entropy generation

Entropy generation in the electrolytic cell is a measure of irreversibility and voltage loss within the cell. In other words, voltage losses are a direct result of entropy production within the cell. Hence, entropy generation is a useful robust way to analyze the irreversibilities within the cell. There are other sources of irreversibility within the system, which could impede the overall performance of the cell. These include frictional losses and losses within other devices connected to the cell. The entropy generation associated with overpotentials discussed previously can be expressed as [180]

$$\eta_v = \frac{TS_{gen_{act}}}{2F_c} \tag{4.23}$$

where $S_{gen_{act}}$ is the entropy generation and T is the operating temperature of the cell. Combining equations (4.6), (4.11), (4.22) and (4.23), the following expression for the entropy generation is obtained,

$$S_{gen_{act}} = \frac{2F_c}{T}\left[ROCV - \left(ir + \frac{RT}{Z\alpha F_c}\ln\left(\frac{i}{i_o}\right)\right)\right] \tag{4.24}$$

From equation (4.24), it can be observed that the entropy production is dependent on temperature, current density, exchange current density and charge transfer coefficient.

Unlike other parameters such as overpotential or polarization, entropy production can provide a more robust metric, from which all losses within an electrochemical system can be characterized. For example, entropy production encompasses both irreversible voltage losses of concentration polarization within the electrode, as well as viscous losses induced by frictional irreversibilities of fluid motion within the electrochemical cell. Although this chapter focuses on the surface, ohmic and the concentration overpotentials, the method can be extended to other irreversibilities that include auxiliary equipment linked with the electrochemical cell, such as pumps and heat exchangers. In this way, an entropy-based design tool can be used to minimize irreversibilities and energy input required for the overall system.

4.2 Results of entropy production in an electrolytic cell

In this section, predicted results of voltage losses and entropy production will be presented. The operating parameters (Table 4.1) are intended to replicate conditions of experimental studies conducted by Atomic Energy of Canada Limited (AECL) [181] on nuclear-based hydrogen production with a thermochemical copper-chlorine cycle [136, 137]. Figure 4.2 illustrates the effect of varying current density on the overpotential for different ohmic resistances. The negative values correspond to a reverse direction of current flow, with hydrogen generated at the expense of electrical energy input, so the system is consuming rather than generating electricity, as per the case with a fuel cell. The equilibrium potential of about 1.009 mV was calculated based on the Gibbs free energy.

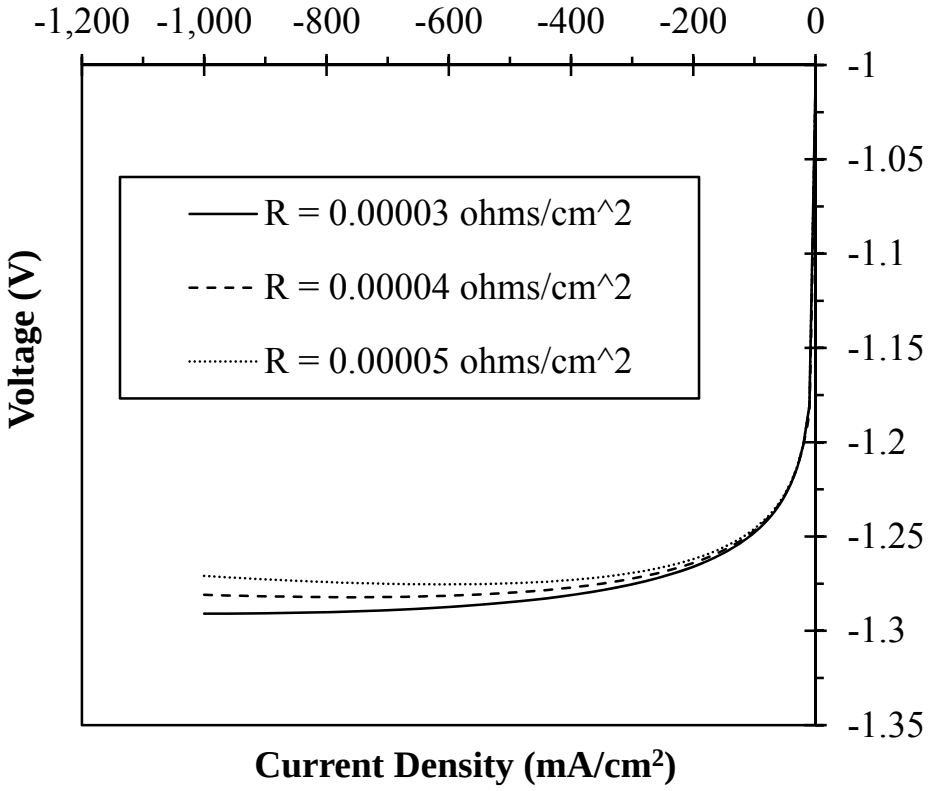

Figure 4.2: Effects of current density on the overpotential for varying ohmic resistances

A decrease in current density between 0 and 250mA/cm^2 results in a steep increase of voltage across the cell. This trend is observed for all ohmic resistances in this study. The increase in voltage amounts to about 26% of the ROCV. There is no significant difference in voltage rise, between current densities of 0 and -400mA/cm^2 for the three cases of ohmic resistance under investigation. Beyond this range of current density, a more significant difference in voltage can be observed. The maximum difference between the ohmic resistances was about 1.5%. The operating temperature of the electrochemical cell has a significant effect on the entropy generation in Figure 4.3. The entropy generation for the three temperatures is nearly equal until about 100J/kgK.

Beyond a current density of 200mA/cm^2, the rate of change of entropy production is not significant for the range of temperature under consideration.

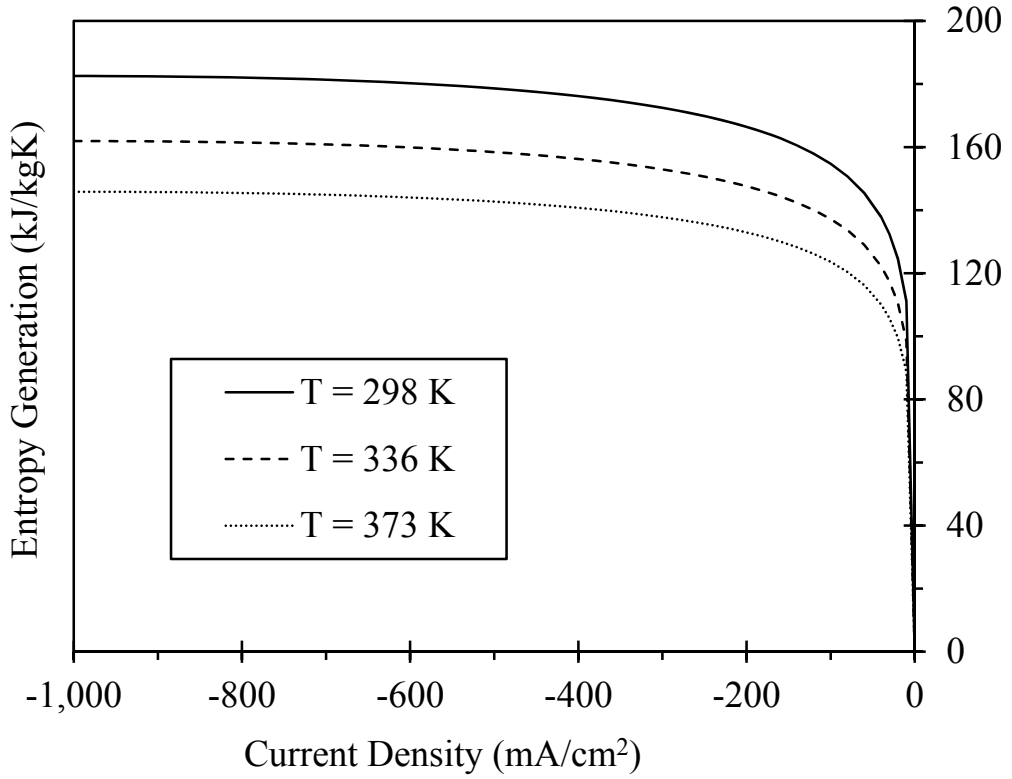

Figure 4.3: Effects of varying cell temperature on the entropy production of CuCl/HCl electrolysis

It can be inferred that some level of equilibrium has been attained for the electrochemical reaction. When the temperature of the cell varies from 298K to 373K, the entropy generated decreases by about 25%. This implies that increasing the cell temperature reduces the energy required by the electrochemical cell. For a cell temperature of 298K, a percentage increase of 58% was observed between a current density of 10mA/cm^2 and 400mA/cm^2, while the increase beyond this range is only about 3.6%. An optimization within this range of current density, with cost as the objective

function, would indicate the best current density to operate the electrolytic cell with the working fluid of cuprous chloride.

Table 4.1: Operating conditions in the electrochemical cell

Operating parameters	**Value**
Temperature of the cell, T (K)	373.15
Exchange current density, i_o (A/cm^2)	0.07
Activation potential, η_v (mV)	0.515
Electrons transferred in the reaction, Z	2
Charge transfer coefficient, α	0.5
Molar mass of mixture, M (kg/kmol)	0.17048
Universal Gas constant, R (J/molK)	8.314
Faraday's Constant, F_c (C/mol)	96,500
Concentration of CuCl (mol)	1.5
Concentration of HCl (mol)	6
Reaction Order, γ	0.5
Reversible Open Circuit Voltage, $ROCV$ (mV)	-1.009

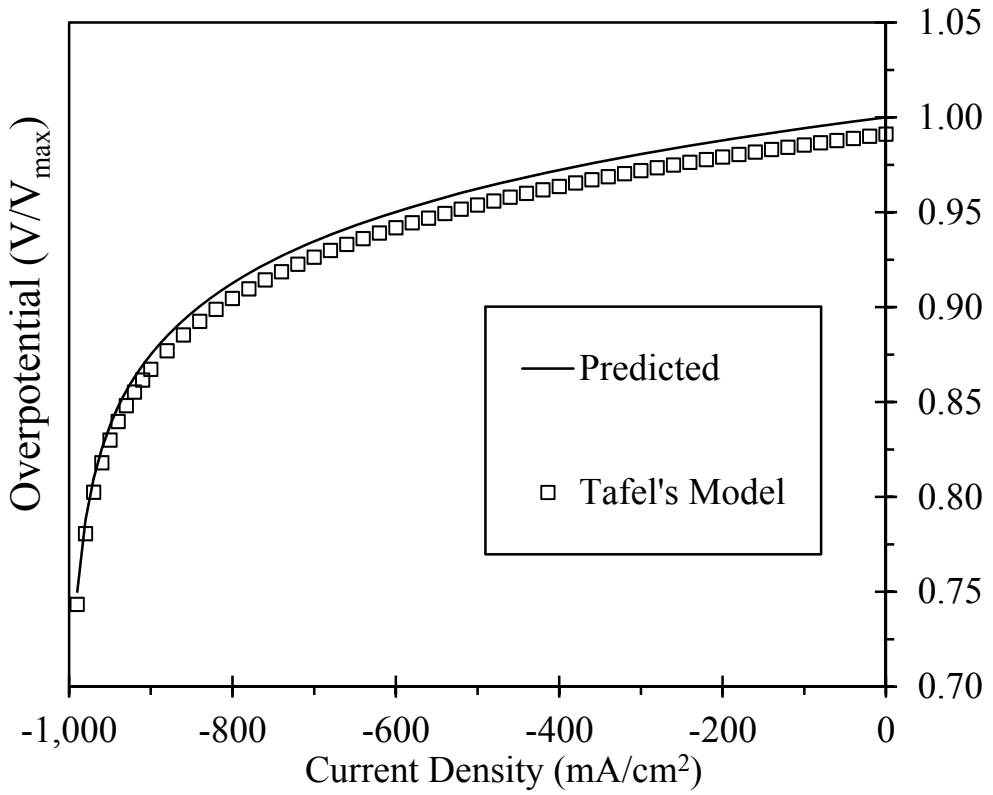

Figure 4.4: Comparison between predicted results and Tafel's model for CuCl/HCl electrolysis

Table 4.2: Comparison between predicted and measured results [181]

Operating parameters	**Measured**	**Predicted**
Operating temperature of cell (T)	298.15K	298 K
Activation potential (V_{act})	0.277mV	0.261 mV
Current density (i)	250mA/cm^2	250 mA/cm^2
Reversible open circuit voltage (ROCV)	0.414 mV	0.515 mV

A comparison between Tafel's model [176] and the current new formulation is presented in Figure 4.4. Close agreement between the results provides a useful validation

of the current formulation, as the maximum difference between both methods is only about 0.08%.

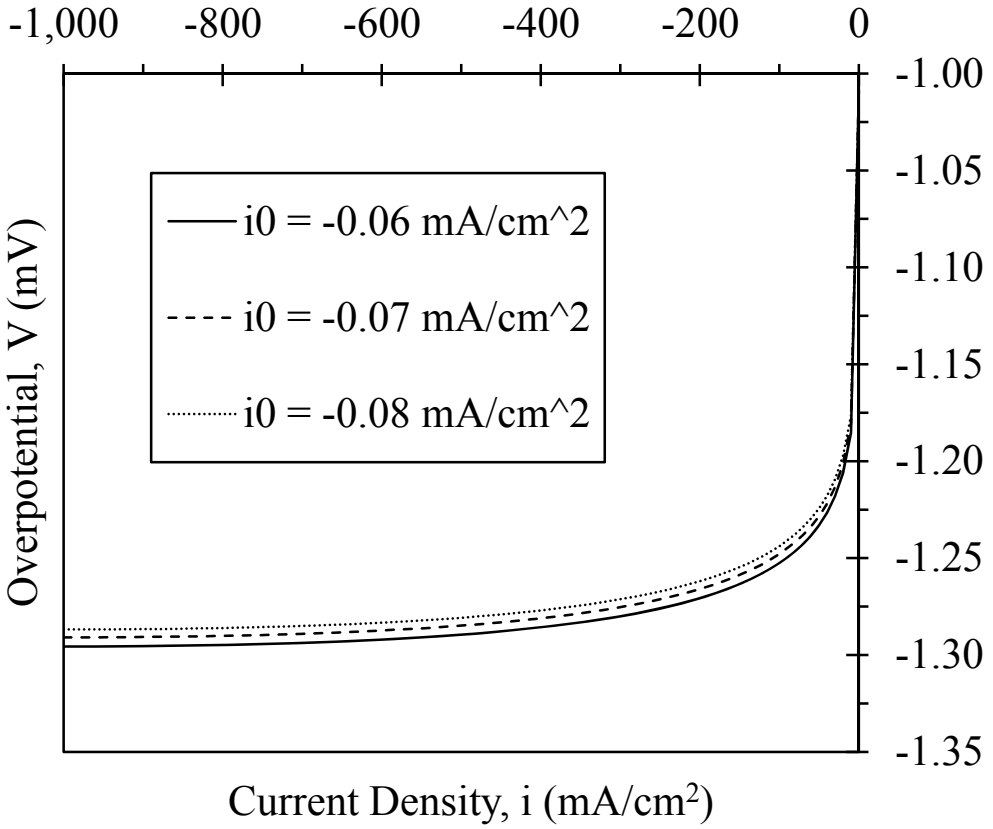

Figure 4.5: Effects of varying exchange current densities on the overpotential

This comparison serves as a useful verification of the model for predicting entropy production during the oxidation of cuprous chloride. In addition, Table 4.2 shows that the magnitudes of the predicted overpotential in the new formulation show close agreement with experimental half-cell data reported previously for cuprous chloride electrolysis [181]. The activation overpotential was measured experimentally [181] and compared against predicted results in Table 4.2. It can be observed that the activation potential shows only about a 6% difference between the experimental activation potential and the predicted results. This relatively small difference may have occurred due to the

measured uncertainty of ROCV, as well as other forms of copper ions or impurities present in the cell [181].

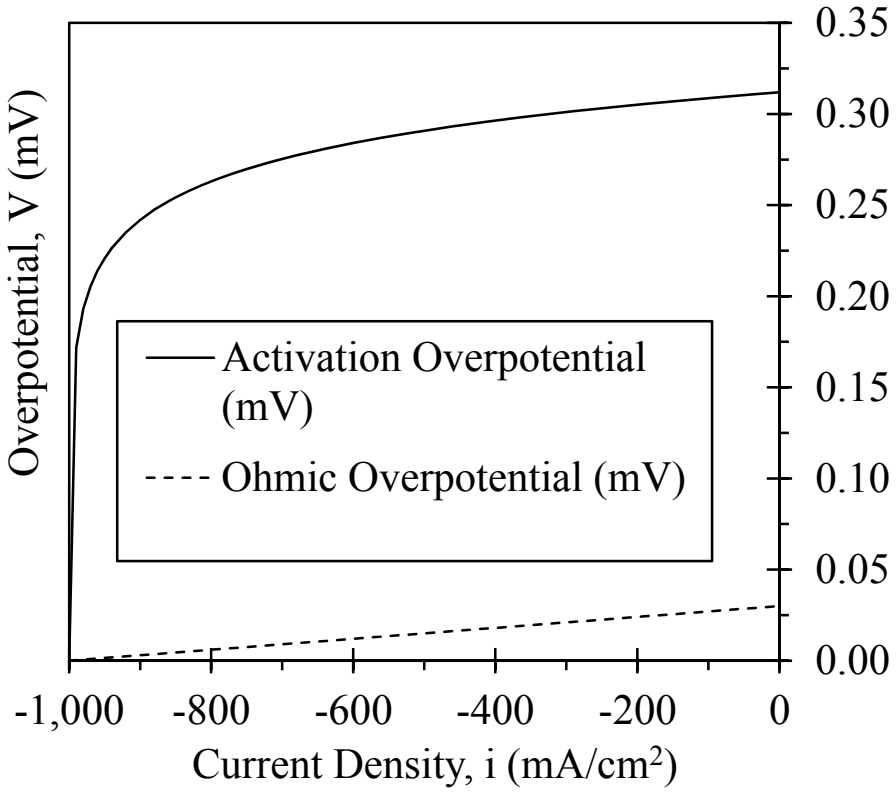

Figure 4.6: Comparison between the predicted activation and ohmic overpotentials

A varying exchange current density has little or no effect on the overpotential of the cell, as shown in Figure 4.5. The maximum difference in overpotential between any of the exchange current densities is only about 0.7%. This difference is similar to results observed by varying the ohmic resistance of the electrochemical cell. Unfortunately, there is no data available (to the author's knowledge) with respect to the relationship between the ohmic resistance and the exchange current density of the electrochemical cell. The activation overpotential is much greater than the ohmic overpotential, as indicated in Figure 4.6. The change in current density significantly affects the activation overpotential. This increase in overpotential is about 81%, when compared with its value

at the lowest current density. The activation overpotential is a major contributor to the overall overpotential, which is not only observed from the trends in Figure 4.6, but also previous trends in Figure 4.3.

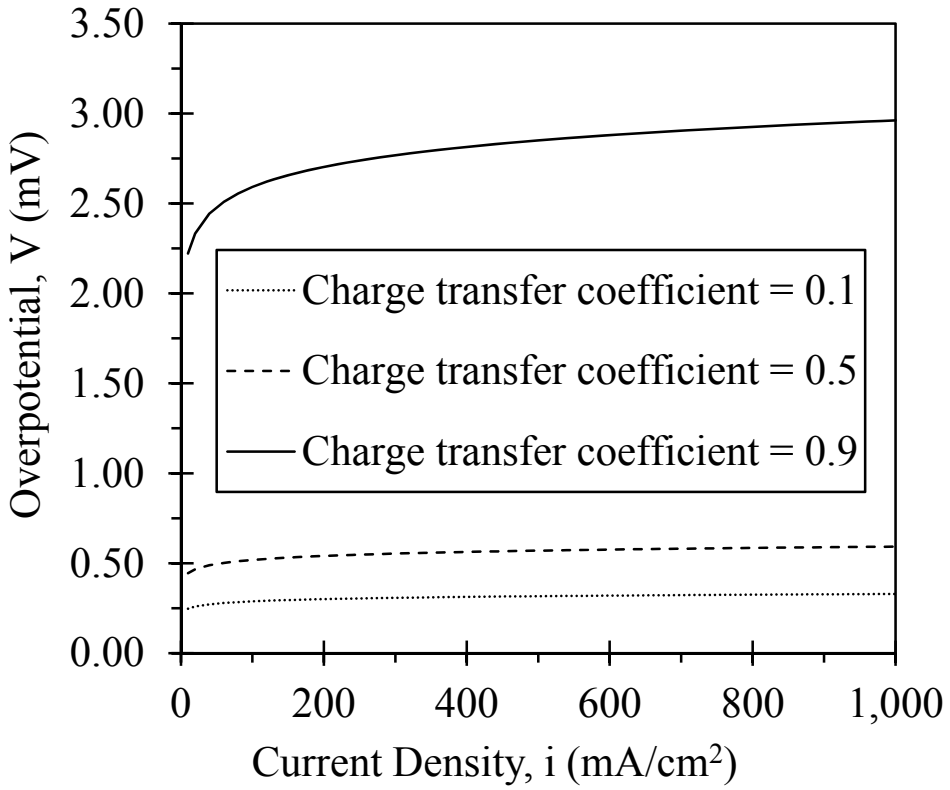

Figure 4.7: Effects of varying charge transfer coefficient on the predicted overpotential of CuCl electrolysis

The ohmic overpotential can be neglected at high current densities, but it has a significant effect at lower current densities (0 – 700mA/cm^2). The ohmic resistance is about double its value at the minimum current density, when compared to the maximum current densities. The ohmic resistance increases linearly with current density, as expected by the relationship of Ohm's Law. The predicted effects of charge transfer coefficient on the overpotential, with changes in the current density, are shown in Figure 4.7. For a higher charge transfer coefficient, a larger overpotential is obtained.

This trend is consistent with past studies of Newman and Thomas [176]. The percentage increase in overpotential with current density is larger at a higher charge coefficient. The largest percentage difference in overpotential for any of the three charge transfer coefficients is about 36%. These results provide useful new insight into the performance and operation of cuprous chloride electrolysis, as a key electrochemical step within a copper-chlorine cycle of hydrogen production.

Chapter 5 : Droplet dynamics and entropy generation in microchannels

Analytical models will be developed in this chapter to examine important physical phenomena that affect the operation of the MHE (as described in chapter 3). An analytical model is used to better understand the droplet motion in the micro heat engine. Experimental results of Odukoya *et al.* [182-184], showed that earlier analytical models by Glockner and Naterer [1,2] over predict the droplet displacement. This thesis extends those past studies, to include surface tension hysteresis during initial start-up of droplet motion, modeling of the simultaneous effects of thermocapillary, pressure, and friction forces on the droplet displacement, and resulting thermal and friction irreversibilities, as determined by entropy and the Second Law.

In this chapter, a new model is also presented for thermocapillary droplet transport in microchannels, including minimization of the entropy generation with respect to Reynolds number, to determine the optimal flow conditions for droplet transport through the microchannel. The effects of surface roughness on viscosity and local Reynolds number are determined and used to improve the transient model of droplet velocity. The transient nature of the velocity of the droplet is also compared to the Poiseuille flow assumption and its effect on voltage production in the MHE is examined in this study.

The droplet motion in the MHE will lead to a pressure gradient in the air gap in the channel making the piezoelectric membrane flex at the bottom of the channel. The effect of the pressure gradient on the deflection of the piezoelectric membrane has not

been studied in past literature to the best of the knowledge of the author. This thesis applies known models of the deflection of a thin membrane [185] to determine the effects of the pressure gradient in the air gap across the microchannel on the piezoelectric membrane. The deflection of the membrane can be used to estimate the voltage produced in the micro heat engine (MHE). The efficiency of the micro heat engine is also modeled in this section.

New models for predicting the evaporation and de-pinning of DI-water and toluene in rectangular microchannels are also presented in this chapter. Controlling the evaporation rate in the closed microchannel will guide the design process of the MHE.

5.1 Droplet displacement

In order to examine the processes, a relatively straightforward fabrication technique was initially based on deformation of a glass capillary tube used to produce the microchannel without the piezoelectric membranes. An experimental setup was developed to investigate the effect of heat transfer on a micro droplet in a closed microchannel. Simulations were also performed to validate the results from the experiments.

Consider a droplet positioned between two air pockets in a closed circular microchannel (see Figure 5.1). There is a uniformly distributed cyclic heat source around the droplet. During heat input, thermocapillary forces induce fluid motion from left to right. Heat transfer to one end of the droplet leads to temperature variations within the liquid. This leads to internal recirculation within the droplet as shown in Figure 5.1. The direction of the two rotating cells is a result of the heating of the droplet on the left end of

the channel. The molecular motion of the droplet drives the droplet from the hot temperature heat source to the cold region and within the two half-cell regions.

Thermocapillary pumping arises when such variations, and differences between contact angles at both ends of the droplet, contribute to an effective pressure difference across the liquid. This difference induces fluid motion within the microchannel. When the droplet moves from left to right, the air pressure increases in the right section of the microchannel and decreases in the left section. The increased pressure on the right end of the channel is used to deflect the piezoelectric membrane located at the cold end of the microchannel. The deflection of the piezoelectric membrane induces a change in the crystallographic structure of the membrane, which generates electric voltage in the process. During the cooling period when the heat source is turned off, these relative air pressures drive fluid back towards the initial equilibrium position of the droplet. In the MHE, the heat sources have been imbedded at the two ends of the channel to generate a cyclic heat source for continuous voltage generation from ends of the microchannel. The cyclic heat source could be readily connected to several microchannels in parallel. In this way, microfluidic transport within a larger network of microchannels could be effectively controlled by thermocapillary pumping.

Internal fluid motion within the droplet is governed by the Navier-Stokes equations, subject to appropriate boundary pressures at both ends of the droplet. An external pressure is generated when the droplet moves in the microchannel. In practical applications, the external pressure can be used when triggering a sensor, activating a switch or operating a flow control device in a microdevice. In Figure 5.1, $P_{c,L}$ is the capillary pressure on the left side of the droplet, $P_{c,R}$ is the capillary pressure on the right

side of the droplet, θ is the contact angle between the liquid and solid wall and H is the channel height. The droplet is hydrophilic if the droplet is the wetting fluid, in which case $\theta < 90$. On the other hand, the droplet is considered hydrophobic if the surrounding fluid is the wetting fluid, for which $\theta > 90$. In Figure 5.1, θ is the contact angle and P represents pressure. The subscripts L and R refer to the left and right edges of the droplet, respectively. The contact angle is measured through the fluid of interest. If the contact angle is measured through the wetting fluid, it is always less than 90 degrees.

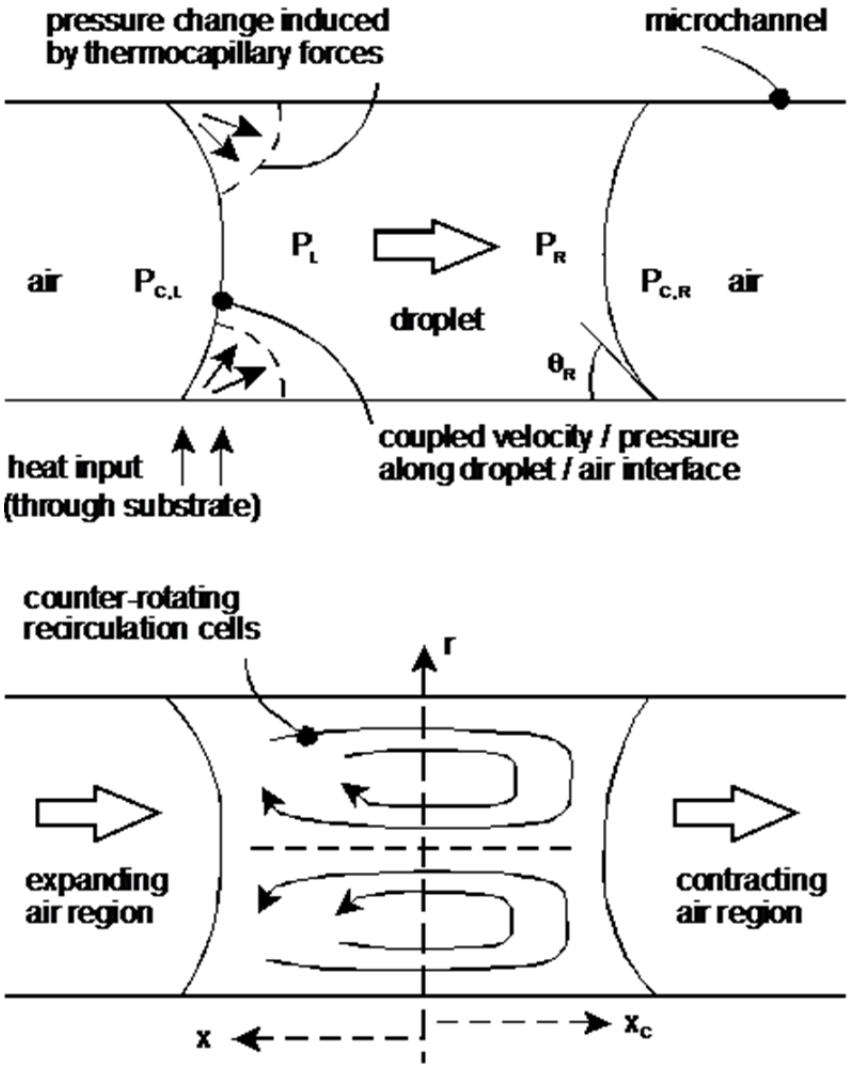

Figure 5.1: Schematic of closed circular microchannel with a uniform heat source

During the change of surface tension across the droplet, the resulting pressure difference induces bulk motion internally within the liquid. The change of surface tension at the heated meniscus with temperature, T, can be represented by $\sigma = A - BT$, where A and B are constants (i.e. A = 75.83dyn/cm and B = 0.1477dyn/cmK for water). A desirable feature of the working fluid is a high change of surface tension with temperature, which would generate the largest pressure difference for a given heat input. For example, water and H_2O_2 have high coefficients of B (most desirable). But surface tension must overcome friction within the droplet. When divided by dynamic viscosity, other fluids (such as toluene) become more effective as a working fluid. The working fluid should generate a high tension-induced pressure difference, in excess of a fixed frictional resistance within the liquid.

The surface tension along the receding meniscus of the droplet in Figure 5.1 decreases with increasing temperature. As a result, it decreases when the receding end of the droplet is heated, which lowers the capillary pressure and causes relaxation of the meniscus. The net decrease in capillary pressure is slightly offset by a corresponding increase associated with a smaller receding contact angle. In order to maintain a constant droplet volume, the advancing contact angle (θ_R) increases, thereby resulting in a decrease of interfacial capillary pressure and accompanying increase in P_R. The resulting pressure gradient within the droplet is reflected through a change in the shapes of the menisci at both receding and advancing edges of the droplet.

In other to analyze the detailed fluid motion, the laws of conservation of mass, momentum, and energy should be solved. These equations can be represented in partial differential equation form as follows:

$$\frac{\partial \rho}{\partial t}+\frac{\partial \rho}{\partial x_i}\left(\rho u_i\right)=0 \tag{5.1}$$

$$\frac{\partial}{\partial t}\left(\rho u_i\right)+\frac{\partial}{\partial x_i}\left(\rho u_j u_i\right)=\rho F_i-\frac{\partial p}{\partial x_j}+\frac{\partial}{\partial x_j}\tau_{ji} \tag{5.2}$$

$$\frac{\partial}{\partial t}\left(\rho e\right)+\frac{\partial}{\partial x_i}\left(\rho u_i e\right)=-p\frac{\partial u_i}{\partial x_i}+\tau_{ji}\frac{\partial u_i}{\partial x_j}+\frac{\partial q_i}{\partial x_i} \tag{5.3}$$

Equations (5.1), (5.2), and (5.3) represent the mass, momentum, and energy equations, respectively: u_i represents the flow velocity, ρ is the local density, P is the pressure, τ is the stress tensor, e is the internal energy, F is the body force, and q is the heat flux. The type of problem and boundary conditions affect the assumptions made to obtain analytical or numerical results. Gravity does not have a significant effect at the micro scale, hence the gravity force component in equation (5.2) will be neglected. These equations are applicable to both gases and liquids. The boundary conditions associated with Poiseuille flow, used to analyse the flow in the closed circular microchannel, are given as follows:

$$\mu\frac{d^2u_x}{dy^2}=\frac{\partial p}{\partial x}=\text{constant} \tag{5.4}$$

$$u_y = u_z = 0 \tag{5.5}$$

$$\frac{\partial p}{\partial y}=\frac{\partial p}{\partial z}=0 \tag{5.6}$$

$$p=p\left(x\right) \tag{5.7}$$

The viscosity of the fluid can have a significant effect on the flow of the liquid. Past studies have examined whether the viscosity at the micro level and macro level are equivalent. Gad-el-hak [186] has performed an extensive review of the experimental measurements of viscosity in microchannels. In order to analyse fluid flow in channels, two major assumptions are commonly made; the stress is directly proportional to the strain rate, and the heat flow across the fluid is proportional to the temperature gradient (Fourier law of heat conduction). The Newtonian assumption would become invalid once the strain rate is approximately double the molecular interaction frequency.

The predominant mode of heat transfer in this problem will be axial transient conduction. Fourier's law of heat conduction can be expressed as:

$$\rho c_p \frac{\partial T}{\partial t} = \frac{\partial}{\partial x}\left(k\frac{\partial T}{\partial x}\right) + \frac{\partial}{\partial y}\left(k\frac{\partial T}{\partial y}\right) + \frac{\partial}{\partial z}\left(k\frac{\partial T}{\partial z}\right) + \dot{q} \tag{5.8}$$

where c_p is the specific heat capacity at constant pressure and $\dot{q}$ is the volumetric heat source. The boundary conditions are required to fully represent the heat transfer problem. The boundary conditions in this study will be explained in detail in section 5.2. The thermal conductivity is assumed to be constant for each different medium (air and water). The heat transfer is assumed to be significant only in the axial direction (x).

5.2 Heat transfer formulation

Consider a droplet positioned between two enclosed air regions in a closed circular microchannel (see Figure 5.1). There is a uniformly distributed cyclic heat source around the receding end of the droplet, so that heat is transferred across the

circumference of the channel. A time scale to characterize heat conduction through a droplet in a microchannel is characterized as follows:

$$t_d = \frac{D^2}{4\alpha} \tag{5.9}$$

where $\alpha = k/(\rho c_p)$ is the thermal diffusivity (1×10^{-6} m^2s^{-1}), and for example, t_d is about 256μs for a 16μm channel. If t_d is lower than the phonon relaxation time (1ps), the continuum equations of heat transfer are no longer applicable to microchannels [187]. Since the estimated value of t_d is larger than the phonon relaxation time, the continuum equations will be used in this study. Liu and Garimella [188] verified experimentally that the continuum equations of fluid flow can be used under these conditions.

The predominant mode of heat transfer in the microchannel is conduction. Previous studies [2] have shown that conduction has a much more significant effect on the temperature distribution across the channel than convection. Conduction occurs in both the radial and axial directions across the droplet. But the heat transfer in the axial direction is much larger than the radial direction, due to the ratio of the droplet height to its length. The microchannel will be divided into three regions: air/substrate region (left side), droplet/substrate region (middle), and air/substrate region (right side). Since the droplet is analysed when it crosses a point along the channel, the analysis is reduced to two regions.

Assuming the droplet is divided into two sections at the left end of the droplet, the two regions of concern are the air/substrate and droplet/substrate regions. The two regions are assumed to be quasi one-dimensional semi-infinite regions. Each region is assumed to have its own heat source so that the temperatures on the right and left of the point along the channel are equal. The heat transfer between the substrate and the

environment will be neglected, since the axial direction is assumed to be most significant for heating of the droplet. An exact solution of the temperature distribution within the droplet, subject to a constant surface heat flux, can be obtained as [189, 190]:

$$T(x,t) = T_i + \frac{2q_s''}{k}\sqrt{\frac{\alpha t}{\pi}}\exp\left(\frac{-x^2}{4\alpha t}\right) - \frac{q_s'' x}{k} erfc\left(\frac{x}{2\sqrt{\alpha t}}\right) \tag{5.10}$$

where $\text{erfc}\, x/\left(2\sqrt{\alpha t}\right)$ is the error function. When x = 0 and appropriate boundary conditions are applied, equation (5.10) becomes

$$T(0,t) = T_i + \frac{2q_s''(\alpha t/\pi)^{\frac{1}{2}}}{k} \tag{5.11}$$

which is extended to two different regions. The left and right temperature distributions can be determined from:

$$T_L(0,t) = T_i + \frac{2q_{s,L}''(\alpha_L t/\pi)^{\frac{1}{2}}}{k_L} \tag{5.12}$$

$$T_R(0,t) = T_i + \frac{2q_{s,R}''(\alpha_R t/\pi)^{\frac{1}{2}}}{k_R} \tag{5.13}$$

Equation (5.11) is modified based on the experimental measurements in the present study as follows:

$$T(0,t) = T_i + \frac{2q_s''\left(\frac{a\,\alpha\, t}{\pi}\right)^{\frac{1}{2}}}{k} \tag{5.14}$$

where a is an empirical factor. In this study, the factor was determined experimentally as 0.00208. It depends on the initial temperature of the droplet (13.5^{o}C in this study). The factor is estimated based on discrete scaling of the Biot number (Bi), which characterizes temperature uniformity within the droplet.

$$a = 3.33Bi = 3.33\left(\frac{h_o L_c}{k}\right) \tag{5.15}$$

Equation (5.14) is required to estimate the temperature of the droplet once the time scale of heat input exceeds 0.0005s.

At the interface of the air/substrate and droplet/substrate regions, the temperatures are approximately equal:

$$q''_{s,L}\frac{(\alpha_L)^{1/2}}{k_L} = q''_{s,R}\frac{(\alpha_R)^{1/2}}{k_R} \tag{5.16}$$

This implies that the total heat flux q''_s is

$$q''_s = q''_{s,L} + q''_{s,R} \tag{5.17}$$

Substituting equation (5.17) into equation (5.16), the following expression is obtained for the heat flux on the left side:

$$q''_{s,L} = \frac{q''_s(\alpha_R)^{1/2}/k_R}{(\alpha_L)^{1/2}/k_L + (\alpha_R)^{1/2}/k_R} \tag{5.18}$$

The microchannel is represented as a composite region for both right and left sides of the boundary of equal temperatures. The left side has a layer for the substrate at the bottom, air in the middle and the substrate at the top, while the right side has a similar composition but with a water droplet in the middle. The thermal conductivity of the composite can be determined as a function of the height of the air, droplet and substrate, relative to the total height:

$$k_L = k_a\left(\frac{D_a}{H_t}\right) + k_{sub}\left(\frac{H_{sub}}{H_t}\right) \tag{5.19}$$

where D is the diameter of the channel. Similarly the thermal conductivity of the right side can be determined from:

$$k_R = k_d\left(\frac{D_d}{H_t}\right) + k_{sub}\left(\frac{H_{sub}}{H_t}\right) \tag{5.20}$$

The thermal diffusivity is also a function of the ratio of the height of each part of the composite material, relative to its total height, leading to

$$\alpha_L = \frac{k_L}{\rho_a c_{p,a} D_a / H_t + \rho_s c_{p,s} H_s / H_t} \tag{5.21}$$

Similarly, the thermal diffusivity of the right side can be determined from:

$$\alpha_R = \frac{k_R}{\rho_d c_{p,d} D_d / H_t + \rho_s c_{p,s} H_s / H_t} \tag{5.22}$$

The following section will use this heat transfer formulation to predict the displacement and motion of the droplet within the microchannel.

5.3 Formulation of droplet motion

The predictive model developed in section 5.2 yields an approximation of the temperature during the heating period. Droplet displacement in a microchannel has been studied previously by Glockner and Naterer [2, 191] and Baikov *et al.* [192]. In this thesis, unlike past studies, the displacement of the droplet is analysed in three separate stages. The heat applied to the droplet generates an initial force necessary to overcome the internal friction and surface tension within the droplet, known as surface tension hysteresis. The second stage is a transition period until the droplet moves with a constant acceleration. The last stage occurs when constant acceleration is achieved and the droplet motion can be approximated by Poiseuille flow. The force exerted on a droplet in a

closed circular microchannel, based on a slug flow approximation (i.e., droplet modelled as a single lumped mass), can be expressed as

$$F = GA\left[\left(\frac{\sigma\cos\theta}{D}\right)_R - \left(\frac{\sigma\cos\theta}{D}\right)_L\right] + AR\left[\left(\frac{m_a T_a}{V_a}\right)_L - \left(\frac{m_a T_a}{V_a}\right)_R\right] + \frac{32}{D^2}\mu A u_b \Delta x \tag{5.23}$$

where $G = 4$ for a circular microchannel, θ is the contact angle and μ is fluid viscosity. The terms on the right side of the equation represent the thermocapillary, external air, and frictional forces, respectively. The contact angle between the droplet and channel wall was obtained by close examination of the immersed droplet under a scanning electron microscope. The gravity forces are negligible with respect to thermocapillary forces, since the Bond number ($Bo = \rho g D^2/\sigma$) is very small. In the experiments, it is shown that the droplet returns to its original position when the heating is removed, meaning that the droplet moves due to heating and not gravity. Gravity effects (if any) would only affect the initial configuration of the droplet inside the capillary and not its movement, since gravity is present before the heating is applied.

The velocity and displacement of the droplet can be determined by integration of the equation of motion of the droplet, thereby yielding

$$u = u^o + F\,\frac{\Delta t}{m} \tag{5.24}$$

$$x = x^o + u\Delta t \tag{5.25}$$

where m is the mass of the droplet, and u^o and x^o are the velocity and displacement at the previous time step. The change of surface tension σ is estimated based on the temperature change across the droplet: $\sigma = \xi - BT$, where ξ= 0.07583N/m and $B = 4.177\times10^{-4}$ N/m K [2].

5.4 Entropy generation in the microchannel

Entropy generation of droplet motion and heat transfer in the microchannel will be determined by considering a differential channel length as a control volume, and performing an energy balance across the control volume as follows,

$$\dot{m}dh = \dot{q}_s^{'}dx \tag{5.26}$$

where $\dot{q}_s^{'}$ [W/m] is the rate at which heat is transferred to the fluid stream by a finite wall - bulk fluid temperature difference, ΔT [128]. There is a constant uniformly distributed heat flux applied to the droplet. The entropy balance across the droplet can be written as

$$\frac{d\dot{S}_{gen}}{dx} = \dot{m}ds - \frac{\dot{q}_s^{'}dx}{T(t)+\Delta T} \tag{5.27}$$

Using equation (5.26) and the Gibbs equation, equation (5.27) can be written as

$$\dot{S}_{gen}^{'} = \frac{d\dot{S}_{gen}}{dx} = \frac{\dot{q}_s^{'}dT}{T^2(t)\left(1+dT/T(t)\right)} + \frac{\dot{m}}{\rho T(t)}\left(-\frac{dP}{dx}\right) \tag{5.28}$$

where the temperature *T(t)*, is a function of time, and *dP/dx* is the pressure gradient across the liquid droplet, determined as follows from the net force on the droplet,

$$\frac{\Delta P}{\Delta x} = \frac{F}{A} - \left(P_s + P_a\right) \tag{5.29}$$

Here, P_s and P_a are the resultant pressures from the change in surface tension, and change in pressure in the air columns, respectively.

The change in air pressure is derived from the ideal gas law as

$$P_a = R\left[\left(\frac{m_a T_a(t)}{V_a}\right)_R - \left(\frac{m_a T_a(t)}{V_a}\right)_L\right] \tag{5.30}$$

The change in pressure as a result of a change in surface tension is obtained from the following Laplace's equation for the surface tension.

$$P_s = G\left[\left(\frac{\sigma\cos\theta}{D}\right)_R - \left(\frac{\sigma\cos\theta}{D}\right)_L\right] \tag{5.31}$$

The change in pressure can be written in terms of the viscous force as:

$$\frac{dP}{dx} = \frac{128\mu\dot{m}}{\pi\rho D^4} \tag{5.32}$$

Substituting for the Reynolds number in equation (5.32), where $\mathrm{Re}_D = \frac{4\dot{m}}{\mu\pi D}$ and rearranging equation (5.28), the entropy generation per unit length becomes

$$\dot{S}'_{gen} = \frac{\dot{q}'_s \Delta T}{T^2(t)} + \frac{1}{\rho^2 T(t)}\left(\frac{\pi^3\mu^5\,\mathrm{Re}_D^4}{2\dot{m}^2}\right) \tag{5.33}$$

The change in temperature (ΔT) across the droplet can be related to the heat flux through the expression for convective heat transfer ($q'_s = \pi Nuk\Delta T$). Substituting for ΔT in equation (5.33), an expression for entropy generation, in terms of the Nusselt number (*Nu*), is obtained. The correlation for laminar flow for the Nusselt number (Nu) as a function of Reynolds number (*Re*) and Prandtl number (*Pr*) is $Nu = 0.453\,\mathrm{Pr}^{1/3}\,\mathrm{Re}^{1/5}$ [189], which is substituted into equation (5.33) to yield the following expression:

$$\dot{S}'_{gen} = \frac{0.70\dot{q}'^2_s\,\mathrm{Pr}^{-0.33}\,\mathrm{Re}_D^{-0.5}}{kT(t)^2} + \frac{15.50\mu^5 R\mathrm{e}_D^4}{\dot{m}^2\rho^2 T(t)} \tag{5.34}$$

The optimum Reynolds number is determined by differentiating equation (5.34) with respect to the Reynolds number and equating it to zero, yielding:

$$\mathrm{Re}_{Dopt} = 0.3166\left(\frac{\dot{m}^2\rho^2\dot{q}_s^{'2}}{\mu^5 kT(t)}\right)^{0.2222} Pr^{-0.073} \tag{5.35}$$

The optimal Reynolds number from equation (5.35) is substituted into equation (5.34) to obtain the minimum entropy generation. The following duty parameter is a non-dimensional parameter to characterize Re_{opt},

$$B_o = \frac{\dot{m}\dot{q}_s^{'}\rho}{\mu^{5/2}(kT(t))^{1/2}} \tag{5.36}$$

Once $\dot{m}$ and $\dot{q}_s^{'}$ are established, B_o can be adjusted to obtain the optimal geometrical configuration of the microchannel to minimize the net entropy production of droplet motion. An expression can also be obtained for the entropy generation number, based on a dimensional ratio of the actual entropy generation to its minimum value, in terms of the Reynolds number.

$$N_s = \frac{\dot{S}_{gen}^{'}}{\dot{S}_{gen_{\min}}^{'}} = 0.889\left(\frac{\mathrm{Re}}{\mathrm{Re}_{opt}}\right)^{-0.5} + 0.111\left(\frac{\mathrm{Re}}{\mathrm{Re}_{opt}}\right)^{4} \tag{5.37}$$

The next section investigates the effects of surface roughness on the droplet flow in the microchannel. This is another irreversibility, which could affect the performance of the MHE.

5.5 Surface roughness formulation

Surface roughness affects the momentum near the wall of a microchannel. This will affect the velocity profile of the flow when it is in the laminar region. Mala and Li [151] suggested a modified roughness viscosity model, which will account for the momentum change along the wall of microchannels. The modified fluid viscosity is the

sum of roughness viscosity and fluid viscosity. The apparent viscosity can be represented as

$$\mu_{app} = \mu_R + \mu_f \tag{5.38}$$

The apparent viscosity can be used to model the flow of water in a microchannel. Qu *et al.* [126] developed an analytical model to determine the ratio of the roughness viscosity to the fluid viscosity, expressed as:

$$\frac{\mu_R}{\mu} = A_p \,\mathrm{Re}_K \times \frac{\left(R_h - l_{\min}\right)}{K}\left[1 - \exp\left(-\frac{\mathrm{Re}_K}{\mathrm{Re}}\frac{\left(R_h - l_{\min}\right)}{K}\right)\right]^2 \tag{5.39}$$

where A_p is the coefficient of roughness viscosity and is determined by an empirical correlation of the experimental data, Re_K is the local roughness Reynolds number, and l_{min} is the shortest distance between the peaks of the roughness elements and the channel wall,

$$A_p = 5.8\left(\frac{R_h}{K}\right)^{0.35} \times \exp\left[\mathrm{Re}^{0.94}\left(5.0\times10^{-5}\frac{R_h}{K} - 0.0031\right)\right] \tag{5.40}$$

where K is the height of the roughness element and R_h is the hydraulic radius. The height of the roughness element must be determined experimentally. From equations (5.39) and (5.40), it can be observed that the channel dimensions and velocity of the droplet will have a significant effect on how the roughness affects the viscosity of the fluid. The apparent viscosity is determined by examining the substrate under a scanning electron microscope to determine the profile of the surface roughness. A profilometer is used to estimate the roughness height. The estimated viscosity is substituted into equation (5.23) to obtain a better correlation between the theoretical and experimental results. A Dektak profilometer was used to measure the roughness height of the substrate.

5.6 Transient velocity formulation

Unsteady viscous flow occurs when a sudden pressure gradient is applied to a fluid flow through a channel. Several geometries have been investigated in past literature [193-196], ranging from circular, rectangular, and non-circular geometries. The sudden pressure gradient can be induced by a uniformly distributed heat source via conduction through the substrate. If the heat source is continuous over time, the flow will approach a steady state and the transient effect can be negligible. The short period observed in the experiments of the MHE suggest that the droplet motion never actually reaches steady state, necessitating the investigation into its short time flow nature. Szymanski [193] developed the solution of the flow in circular tube. A solution to flow along parallel channels was developed by Rouse and Arpaci *et al.* [194, 195]. Solutions to circular and rectangular configurations can be found in publications by Muller *et al.* and Erdogan *et al.* [197, 198].

Most of these solutions are numerical. A simplified and analytical model which could be used for arbitrary configurations was developed by Muzychka and Yovanovich [198]. This thesis extends the latter model to predict the transient velocity in a closed microchannel. There is no known model (to the author's knowledge) that predicts the transient start-up flow in closed microchannels.

Consider a rectangular microchannel with an average velocity $\bar{u}$ and cross sectional area A. The transient velocity can be estimated from the spatial integral of the instantaneous velocity of the droplet.

$$\bar{u} = \frac{1}{A}\iint_A u dA \tag{5.41}$$

Using the general Poisson equation, the instantaneous velocity distribution can be written as

$$\frac{1}{\nu}\frac{du}{dt}=\frac{1}{\mu}\frac{\Delta P}{L}+\nabla^2 u \tag{5.42}$$

Based on the Muzychka and Yovanovich analogy [198, 199] of a short time flow scale as observed in the case of the MHE, the dimensionless velocity as t→ 0 can be written as

$$u^*=\frac{\overline{u}}{\psi\frac{1}{\mu}\frac{\Delta P}{L}}=\frac{\nu t}{\psi^2} \tag{5.43}$$

where ψ is an arbitrary length scale. Close to the boundary layer, a mass balance between diffusion and storage leads to

$$\frac{1}{\nu}\frac{d\overline{u}}{dt}\sim\frac{\overline{u}}{\delta^{*2}}\rightarrow\delta^*\sim\sqrt{\nu t} \tag{5.44}$$

Poisson's equation in equation (5.42) is solved in the region of the boundary layer based on the boundary conditions of $u^*(0)=0$ and $u^*(t)=t^*$ for a short time. Using the Stokes equation for momentum transport, the boundary layer thickness can be estimated as

$$\delta^*=\frac{2}{\pi}\sqrt{\nu t}\approx 1.128\sqrt{\nu t} \tag{5.45}$$

The length is determined from the hydraulic radius for a rectangular microchannel and can be taken as $\psi = 4A/p$, where A is the cross sectional area and p is the wetted perimeter. Muzychka and Yavanovich [198] recommended the use of $\psi=\sqrt{A}$ for arbitrary cross sections. Using the start-up velocity and modifying the equation of motion in equation (5.24), an expression can be obtained for the velocity in a closed

microchannel. The acceleration of the droplet is determined by the net change in air pressure in the closed channel, while the transient instantaneous velocity can be determined by a temporal integration of the equation of motion. The transient velocity in a closed channel can be written as

$$u(t)=\left[\psi^2\frac{1}{\mu}\frac{\Delta P}{L}\right]\left[t^n+\left(\frac{P_\varsigma\sqrt{A}}{p}\right)^n\right]^{1/n}+\left[R\left[\left(\frac{m_aT_a(t)}{V_a}\right)_R-\left(\frac{m_aT_a(t)}{V_a}\right)_L\right]\right]\frac{t}{m_d} \tag{5.46}$$

where P_ς is the Poiseuille number of the flow. The asymptotic value of n is determined from the aspect ratio of the channel. Extending the asymptotic correlation of Churchill and Usagi [200] to a closed channel where u_∞ tends to zero, the values n can be estimated from:

$$u^*=\left[\left(u_o^*\right)^n+\left(u_\infty^*\right)^n\right]^{1/n} \tag{5.47}$$

Once the transient velocity is known, its effect on voltage production can be estimated from the analytical model for the voltage production from the MHE. The next section highlights the analytical modeling of the voltage generation of the MHE and also its efficiency.

5.7 Electricity generation model

The sum of the strain energy due to deformation and internal stresses yields the total strain energy on the piezoelectric membrane. The strain energy due to bending can be neglected for very thin films if the deflection is much greater than the thickness of the membrane [201]. Tabata *et al.* [202] used the energy minimization approach to determine the load-deflection in thin rectangular membranes. The relationship between pressure on

the membrane and the thickness of the membrane can be determined by the following relationship:

$$P = \frac{t_{pzt}}{b^2} w_m \left[C_1 \gamma_o + \frac{f(\nu)}{b^2} \frac{E}{1-\nu} w_m^2 \right] \tag{5.48}$$

where t is the thickness of the membrane, b is the width of the membrane, γ_o is the residual stress in the membrane, ν is Poisson's ratio, E is Young's modulus of the membrane, and C_1 and f(ν) are geometry dependent constants.

The effect of the droplet motion on the piezoelectric membrane is modeled as a uniformly distributed pressure that is applied to a thin membrane. This requires determination of the bending moment of each layer about a neutral axis relative to the piezoelectric membrane. The general equation for determining the pressure due the stresses in the longitudinal and transverse directions across the membrane is given as follows:

$$P = \frac{12}{E t_{pzt}^2 (1-\nu)} \left(\frac{\partial^4 w_m}{\partial x^4} \frac{\partial^4 w}{\partial x^4} + 2 \frac{\partial^4 w_m}{\partial x^2 \partial y^2} + \frac{\partial^4 w_m}{\partial y^4} \right) \tag{5.49}$$

Re-arranging equation (5.49), the deflection of the membrane can be expressed in terms of pressure exerted on the membrane. The pressure gradient across the channel is determined from the force balance across the microchannel droplet. The net force on the membrane consists of the thermocapillary force, frictional force and resultant air pressure across the droplet. The force exerted on a droplet in a closed rectangular microchannel, based on a slug flow approximation [121-125] (droplet modeled as a single lumped mass) can be expressed as:

$$F = GA\left[\left(\frac{\sigma\cos\theta}{H}\right)_R - \left(\frac{\sigma\cos\theta}{H}\right)_L\right] + AR\left[\left(\frac{m_a T_a}{V_a}\right)_L - \left(\frac{m_a T_a}{V_a}\right)_R\right] + \frac{12}{H}\mu A u_b \Delta x \tag{5.50}$$

where G = 2 for a rectangular microchannel, Θ is the contact angle and μ is fluid viscosity. The terms on the right hand side of the equation represent the thermocapillary, external air and frictional forces, respectively.

The voltage produced by the piezoelectric membrane is a measure of the potential difference across the membrane. The deflection of the membrane is a measure of the change in pressure in the microchannel. The deflection can be related to the stress and strain in the piezoelectric membrane as follows,

$$D = dT + \Phi V_e \tag{5.51}$$

where D, d, T, Φ, V_e are the electrical polarization, piezoelectric coefficient matrix, applied mechanical stress, electric permittivity matrix, and the induced electric field. Since no electric field is induced to generate the voltage, equation (5.51) can be reduced to a matrix of the following form.

$$\begin{bmatrix} D_1 \\ D_2 \\ D_3 \end{bmatrix} = \begin{bmatrix} d_{11} & d_{12} & d_{13} & d_{14} & d_{15} & d_{16} \\ d_{21} & d_{22} & d_{23} & d_{24} & d_{25} & d_{26} \\ d_{31} & d_{32} & d_{33} & d_{34} & d_{35} & d_{36} \end{bmatrix} \begin{bmatrix} T_1 \\ T_2 \\ T_3 \\ T_4 \\ T_5 \\ T_6 \end{bmatrix} \tag{5.52}$$

where,

$$d_{ij} = \begin{bmatrix} 0 & 0 & 0 & 0 & 584 & 0 \\ 0 & 0 & 0 & 584 & 0 & 0 \\ -171 & -171 & 374 & 0 & 0 & 0 \end{bmatrix}$$

The piezoelectric matrix coefficient depends on the nature of the piezoelectric material used in the fabrication. The choice of piezoelectric material for this fabrication will be PZT-5. The T_1, T_2, and T_3 variables are the normal stresses, while T_4, T_5, and T_6 are the shear stresses in the channel. The mechanical stress is occurs when heat is applied to the droplet and it is directly related to the change in pressure across the channel. The effect of the shear stress on the membrane is expected to be relatively small for the current design. The efficiency of the MHE can be estimated relative to the voltage produced from the piezoelectric membrane.

The maximum deflection of the piezoelectric membrane will occur at the center of the membrane. This displacement can be expressed as:

$$w_{m_{center}} = \frac{\beta P b^4}{E_{comp} t_{pzt}^{\ 3}} \tag{5.53}$$

where β is a constant related to the ratio of the length to width of the membrane and P is the uniform pressure on the membrane. The width of the membrane is represented by b, E is Young's modulus of elasticity, and t_{pzt} is the thickness of the membrane. The relationship in equation (5.51) can be extended to the mechanical stress on the membrane in the direction of the membrane [185],

$$T_i = \frac{\chi P_{ij} b^2}{t_{pzt}^2} \tag{5.54}$$

where χ is a constant based on the ratio of the length to the width of the membrane. The estimated values of χ (0.1386) and β (0.0138) [185] are constant for any ratio of the length to width of the membrane, but they differ at the maximum normal stress. Substitution of equation (5.54) into equation (5.52) can be used to estimate the generated voltage from the membrane.

The net in-plane stress can be used to determine the location of the neutral axis, which is the point at which the stress makes the bending effect negligible. The position Z_n is determined by taking account of each layer from the bottom to the top of the membrane, yielding:

$$Z_n = \frac{\sum_i \left(Z_i E_i A_i\right)}{\sum_i E_i A_i} \tag{5.55}$$

where Z_i is the height of each material from the base of the structure, A_i is the cross sectional area of each material and E_i is the Young's modulus of elasticity for each material. The Young's modulus of elasticity of the composite structure is determined based on the ratio of the moment of inertia to the total moment of inertia.

$$E_{comp} = \sum_i E_i \left(\frac{I_i}{I_{total}}\right) \tag{5.56}$$

The piezoelectric membrane deflection can be approximated as the bending of a simply supported beam under load. Murralt [203] and Cho *et al.* [201] showed that the electromechanical coupling factor could be approximated as:

$$k_p^2 = \frac{8}{\pi^2}\frac{G^2}{K}t_{pzt}\frac{\left(d_{31}/s_{11}^E\right)^2}{\varepsilon_{33}^T\left(1-\frac{d_{31}^2}{s_{11}^E\varepsilon_{33}^T}\right)} = \frac{Energy\ converted}{Energy\ input} \tag{5.57}$$

where G is the leverage factor, and K is the bending modulus. The leverage factor can be determined relative to the neutral axis as:

$$G = \left(t_{sub} - Z_n + \frac{t_{pzt}}{2}\right) \tag{5.58}$$

The bending modulus is determined from an integration of the moment per unit length about the neutral axis using appropriate boundary conditions [201].

$$K = E_{sub}t_{sub}\left(\frac{t_{sub}^2}{3} - t_{sub}Z_n + Z_n^2\right) + \alpha t_{pzt}\left(t_{sub}^2 - 2Z_n t_{sub} + t_{sub}t_{pzt} + Z_n^2 - Z_n t_{pzt} + \frac{t_{pzt}^2}{3}\right) \tag{5.59}$$

where

$$\alpha = \frac{1}{s_{11}^E\left(1-\frac{d_{31}^2}{s_{11}^E\varepsilon_{33}^T}\right)} \tag{5.60}$$

The predicted efficiency of the MHE can be determined from the relationship between the electromechanical coupling factor and the quality factor of piezoelectric membrane. The energy input in the experimental setup will be equivalent to the heat supplied to the electric heaters to generate the droplet motion. This can be estimated based on the resistance of the heaters and current supplied to the heaters. The efficiency of the system, based on experimental measurements, can be estimated by the ratio of the

power supplied to the heaters to the energy generated by the piezoelectric membrane under a resistive load.

$$\eta = \frac{\frac{1}{2}\left(\frac{k_p^2}{1-k_p^2}\right)}{\frac{1}{Q_f}+\frac{1}{2}\left(\frac{k_p^2}{1-k_p^2}\right)} = \frac{Energy\ converted}{Energy\ input} = \frac{I_{in}^2 r_{heater}}{V_{D_{out}}^2 / r_{pzt}} \tag{5.61}$$

The efficiency determined from the experimental measurement could be compared with analytical approximation of the efficiency based on the coupling coefficient. The power density of the energy harvester will determine its viability.

5.8 Droplet evaporation model

When a droplet is injected into a microchannel, it takes the shape of the channel. This is dependent on the wetting properties of the fluid. It can either have a concave or convex meniscus with the substrate of the channel. If the droplet is much smaller than the channel dimension, it will adhere to the edge of the channel. The model here is developed for the hydrophobic case, as per the experiment. The model can also be extended to the hydrophilic case, since the main difference will be the contact angle and the volume associated with the concave meniscus. Consider the cross section of the channel and the droplet shown in Figure 5.2.

The transient diffusion mass transfer equation can be used to express the rate of evaporation of the droplet into the surrounding vapor. This can be expressed from Fick's law of diffusion as follows,

$$-M_D = \frac{\partial \rho_D}{\partial t} = D_{AB}\frac{\partial^2 \rho_D}{\partial x^2} \tag{5.62}$$

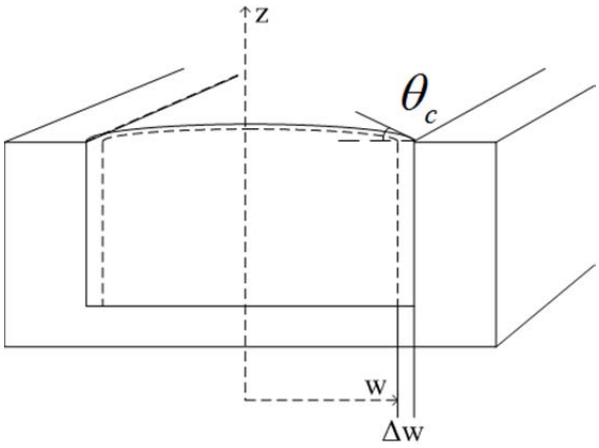

Figure 5.2: Schematic of evaporation process in a closed rectangular microchannel

subject to the following boundary conditions:

$\rho_D = \rho_w \; at \; t = 0 \; for \; 0 \le x \le w$
$\rho_D = \rho_{air} \; at \; z = 0 \; for \; t>0$
$\rho_D = \rho_w \; at \; z = w \; for \; t>0$

Non-dimensionalizing the equation of mass transfer yields

$$\frac{\partial Y}{\partial t} = D_{AB} \frac{\partial^2 Y}{\partial x^2} \tag{5.63}$$

Where $Y = \frac{\rho_D - \rho_{air}}{\rho_w - \rho_{air}}$ with the new boundary conditions set as

$Y = Y_0 \; at \; t = 0 \; for \; 0 \le x \le w$
$Y = 0 \; at \; z = 0 \; for \; t>0$
$Y = Y_0 \; at \; z = w \; for \; t>0$

The general solution of this partial differential equation can be obtained using separation of variables and expressed as:

$$Y = \left[c_1 \cos(\lambda x) + c_2 \sin(\lambda x) \right] e^{-D_{AB}\lambda^2 t} \tag{5.64}$$

Applying the boundary conditions, the constants c_1 and c_2 can be determined to find the following solution:

$$\mathrm{Y}=\frac{4\mathrm{Y}_0}{(2\mathrm{n}+1)\pi}\sum_{\mathrm{n}=0}^{\infty}\left[\sin\left(\lambda x\right)\right]e^{-D_{AB}\left(\frac{2n+1}{L}\right)^2 t} \tag{5.65}$$

Now the change in density with time can be expressed as

$$\rho_D(\mathrm{t})=\frac{4\mathrm{Y}_0\left(\rho_w-\rho_{air}\right)}{(2\mathrm{n}+1)\pi}\sum_{\mathrm{n}=0}^{\infty}\left[\sin\left(\lambda x\right)\right]e^{-D_{AB}\left(\frac{2n+1}{L}\right)^2 t}+\rho_{air} \tag{5.66}$$

From the equation of mass transfer, one can write the change in volume with time as

$$\frac{dV}{dt}=-\frac{D_{AB}}{\rho_w}\int_A\frac{d\rho_D}{dx}\cdot dA=\frac{dV}{dx}\cdot\frac{dx}{dt}=A.\frac{dx}{dt} \tag{5.67}$$

Since the cross sectional area is assumed to be constant as the droplet evaporates along the width of the channel, the rate of evaporation relative to the width of the droplet can be derived from a numerical integration over the channel width.

$$x=-\frac{D_{AB}}{\rho_w}\int\left[\frac{4\mathrm{Y}_0\left(\rho_w-\rho_{air}\right)}{L}\sum_{\mathrm{n}=0}^{\infty}\left[\cos\left(\frac{2n+1}{}\pi x\right)\right]e^{-D_{AB}\left(\frac{2n+1}{L}\right)^2\pi^2 t}\right]dt \tag{5.68}$$

Equation (5.68) is used to predict the change in width of the droplet with time, assuming the droplet spans across the entire width of the channel. The experimental results show that a thin layer exists between the main part of the droplet and the wall. This layer is called the “pinned film”, which starts to evaporate after the main part of the droplet has evaporated.

5.9 Droplet de-pinning model

A thin film of the droplet is attached to the bottom of the channel and it is distinct from the bulk of the droplet. This separation occurs along the contact line of the main

droplet. The process by which this layer evaporates is known as “de-pinning”. Unlike the evaporation process, the de-pinning process starts from the center of the channel and progresses in both directions simultaneously towards the wall. Figure 5.3 shows the de-pining process. The phenomenon is a highly complex process to predict. It occurs in a similar way as evaporation. A semi-empirical approach will be used to analyse the evaporation of the pinned film. The conservation equation of the pinned film can be written as

$$\frac{\partial w}{\partial t} + \nabla \bullet \left(wU \right) = -j\left(r \right) = -D_{ab} \nabla \phi \tag{5.69}$$

where w is the width of the channel, D is the diffusivity , ϕ is the concentration and j(r) is the evaporation rate per unit area. The general equation of average velocity over the width can be expressed as [161]

$$U(w,t) = \frac{w^2}{3\eta} \nabla \bullet \left(\sigma \Delta w - \rho g h + \varphi(h) \right) \tag{5.70}$$

The gravity cannot have an effect at this scale, as the capillary length $l_c = \sqrt{\frac{\sigma}{\rho g}}$ is much less than 1.08mm. The term containing gravity can be neglected in equation (5.70).

$$U(w,t) = \frac{w^2}{3\eta} \nabla \bullet \left(\sigma \Delta w + \varphi(h) \right) \tag{5.71}$$

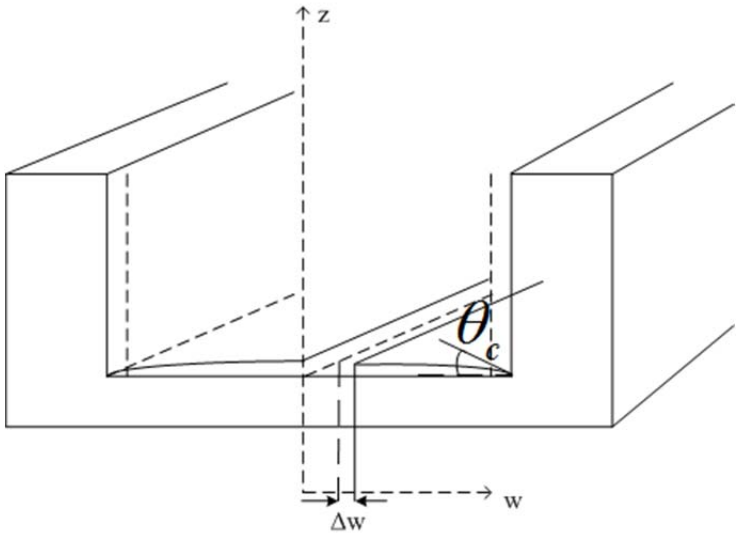

Figure 5.3: Schematic of de-pinning process in a closed rectangular microchannel

The evaporation rate of the droplet has been shown by Deegan [163], Cachile *et al.* [170] and Poulard *et al.* [161] to be proportional to the change in pinning radius based on the instantaneous time and final time. It can be represented as

$$j(r) \sim \left(w_o - w(t)\right)^{-\kappa} \tag{5.72}$$

where

$$\kappa = \frac{\pi - 2\theta_c}{2\pi - 2\theta_c} \tag{5.73}$$

Here θ_c is the contact angle of the droplet and the contact line at the beginning of the de-pinning process. Extending these models to the case of pinning in a rectangular microchannel, the expression can be written for the change in volume with time as

$$\frac{dV}{dt} = \frac{d}{dt}(wyz) + \frac{d}{dt}\left[\frac{\pi w^3 \theta_c}{4}\right] \tag{5.74}$$

Here *w*, *y,* and *z* are the width, length and depth of the film, respectively. Since θ_c is assumed to be constant, based on the particular wetting fluid, and the cross sectional area (*yz*) is also constant, the expression can be reduced to

$$\frac{dV}{dt} = yz\frac{dw}{dt} + \frac{\pi\theta}{4}\frac{dw^3}{dt} \tag{5.75}$$

Since the evaporation rate can also be related to mass transfer across the boundary, the change in volume becomes

$$\frac{dm}{dt} = \rho\frac{dv}{dt} = -j.A(r) \sim A.\left(w_o - w(t)\right)^{-\kappa} \tag{5.76}$$

Combining equations (5.75) and (5.76), the change in pinning radius becomes

$$w = \int \frac{A}{\rho}\left(\frac{\left(w_o - w(t)\right)^{-\kappa}}{yz + \frac{3w_o\pi\theta}{4}}\right)dt \tag{5.77}$$

An expression is determined for $w(t)$ in order to integrate over a known time interval to determine the change in the pinning radius. A method of asymptotic analysis will be used to find $w(t)$, by an assumption based on observations of the experiment of the profile of the pinning displacement. From the experimental observations in this study, *w(t)* is determined to have a correlation as follows:

$$w(t) = \frac{w_o}{2}\left(t_f - t_i\right)^{\kappa} \tag{5.78}$$

The value of κ is dependent on the type of fluid used. A value of 0.3 was derived for DI-water and a value of 0.6 was obtained for toluene based on a similar asymptotic analysis as performed by Cachile *et al.* [170].

The following chapter highlights results from the analytical simulation and experimental results. Experimental results are compared with the predicted models to validate the analytical modeling.

Chapter 6 : Results and discussion

Various numerical studies were performed before the completion of the experiments to investigate the fluid transport and heat transfer characteristics of droplet motion in the microchannel. A schematic of the problem configuration is shown in Figure 1.1. Effects of entropy generation, temperature gradient, transient heat flux and surface roughness will be presented in this chapter. The results will be presented in this chapter along with other analytical models that predict the voltage generation and efficiency of the MHE. Experimental results for power output from the microheater will be presented and compared with predicted results from analytical modeling of the heaters. Experimental and analytical results of the evaporation and de-pinning of the droplet in the microchannel will also be presented.

6.1 Droplet motion in a cylindrical microchannel

In this section, predicted and measured results of droplet temperature and displacement will be presented and discussed. The problem parameters and thermophysical properties are shown in Table 6.1 for droplet motion in a fabricated glass microchannel. Figure 6.1 shows a comparison and close agreement between the predicted and measured temperatures for a 16 μm diameter microchannel. As heat is transferred to the left end of the droplet, the thermocapillary force causes the droplet to move toward the closed end on the right side of the droplet, as shown in Figure 1.1.

The droplet recirculation is symmetric about the centerline of the channel. This occurs in the upper and lower halves of the channel, when the droplet moves from left to right. The ambient start-up temperature is 13.5^{o}C when the heating cycle begins, then

heating is applied and the temperature of the droplet increases with time, and peaks at about 32.5°C.

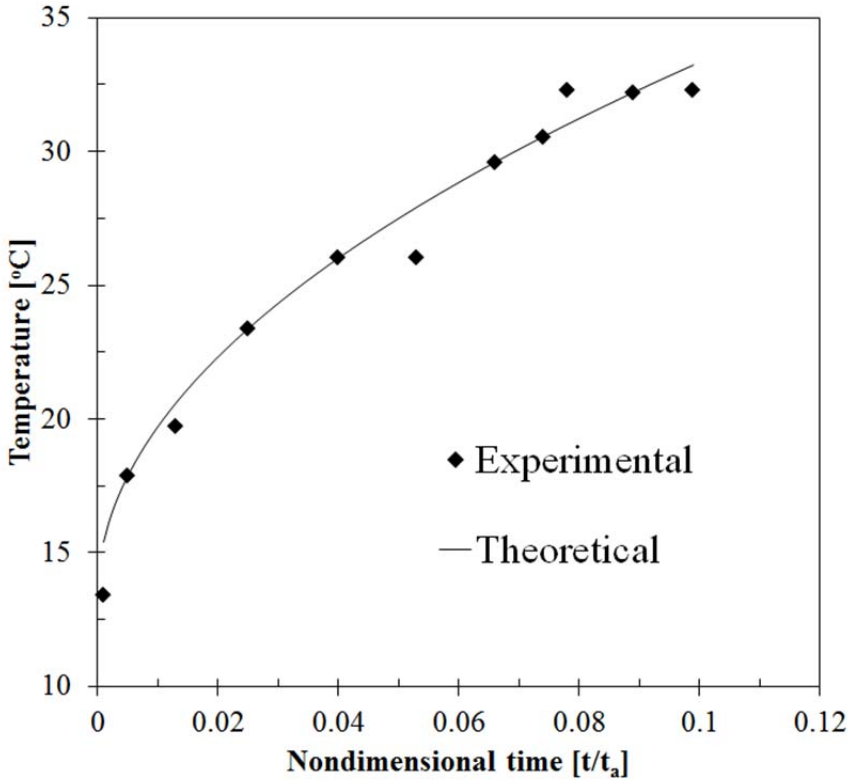

Figure 6.1: Comparison of predicted and experimental results for a 16μm diameter channel

The temperature of the droplet increases over the range of non-dimensional time in Figure 6.1. This close agreement provided useful validation of the predictive model.

The displacement of the droplet increases with time. After about 10s, no further movement of the droplet was observed, as it reached an equilibrium position. This position is a critical point, since the droplet may vaporize if additional heat is applied. The assumptions in the present model for the temperature distribution would no longer be valid if further heating is applied and the droplet is allowed to vaporize, since the flow conditions would become a two-phase flow system.

Table 6.1: Problem parameters and thermophysical properties

Property	Value
Thermal conductivity droplet	0.606W/mK
Diameter of channel	16 μm
Height of droplet	0.13 μm
Height of substrate	0.00113m
Thermal diffusivity	$1 \times 10^{-6} m^2 s^{-1}$
Thermal conductivity of air	0.0263W/mK
Thermal conductivity substrate	0.96W/mK
Heat transfer coefficient	$4.81 W m^2/K$
Heat flux	$3.423 W/m^2$
Density of droplet	$998 kg/m^3$
Density of substrate	$2{,}500 kg/m^3$
Density of air	$1.16 kg/m^3$
Length of channel	0.02262m

The measured temperature is proportional to the supply voltage. A maximum supply voltage of 700μV is supplied from a 10Ω resistor. An increase in current leads to an increase of temperature. The maximum current supplied to the heater is about 70mA. The heat flux in the simulation is determined based on the current supplied and the resistance, per unit length of heater coil. The predicted droplet motion in the circular microchannel uses measured parameters from the experiments. The heat flux is needed to make a comparison between experimental and predicted results. The heat flux depends on the electrical current supplied to the heater (I) and resistivity of the heater wire (ε) as follows:

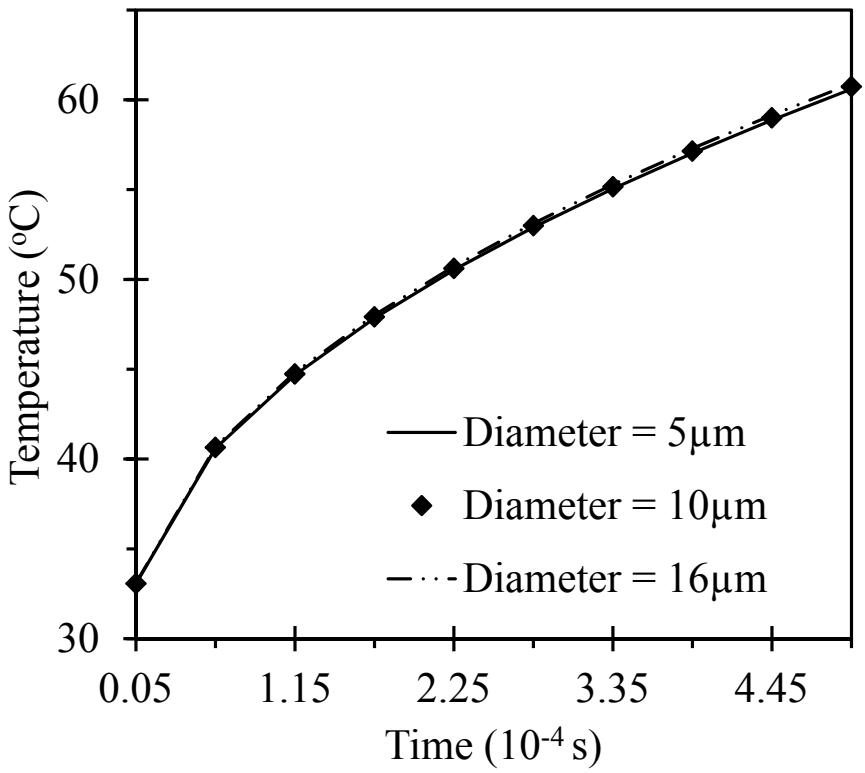

Figure 6.2: Predicted temperature change in different microchannels of varying diameters

$$q_s'' = I^2 \frac{\varepsilon l}{A} \tag{6.1}$$

where l is the length of the heater wire (circumference of the channel) and A is the cross-sectional area of the heater wire.

The simulated channel diameters in Figure 6.2 indicate that a change in channel diameter does not have a significant impact on the temperature change across the droplet. The advantages of thermocapillary pumping are better in smaller channel dimensions, since the effect of the frictional force is minimized and the capillary force is maximized. The temperature of the droplet increases with time, when the droplet is exposed to the heat source. The increase in temperature occurs very rapidly. Although experiments have shown a different order of magnitude than the timescale of analytical modelling, a

response time of less than 10s indicates that the droplet's response to a temperature change is very rapid, which makes it well suited for thermal sensing applications.

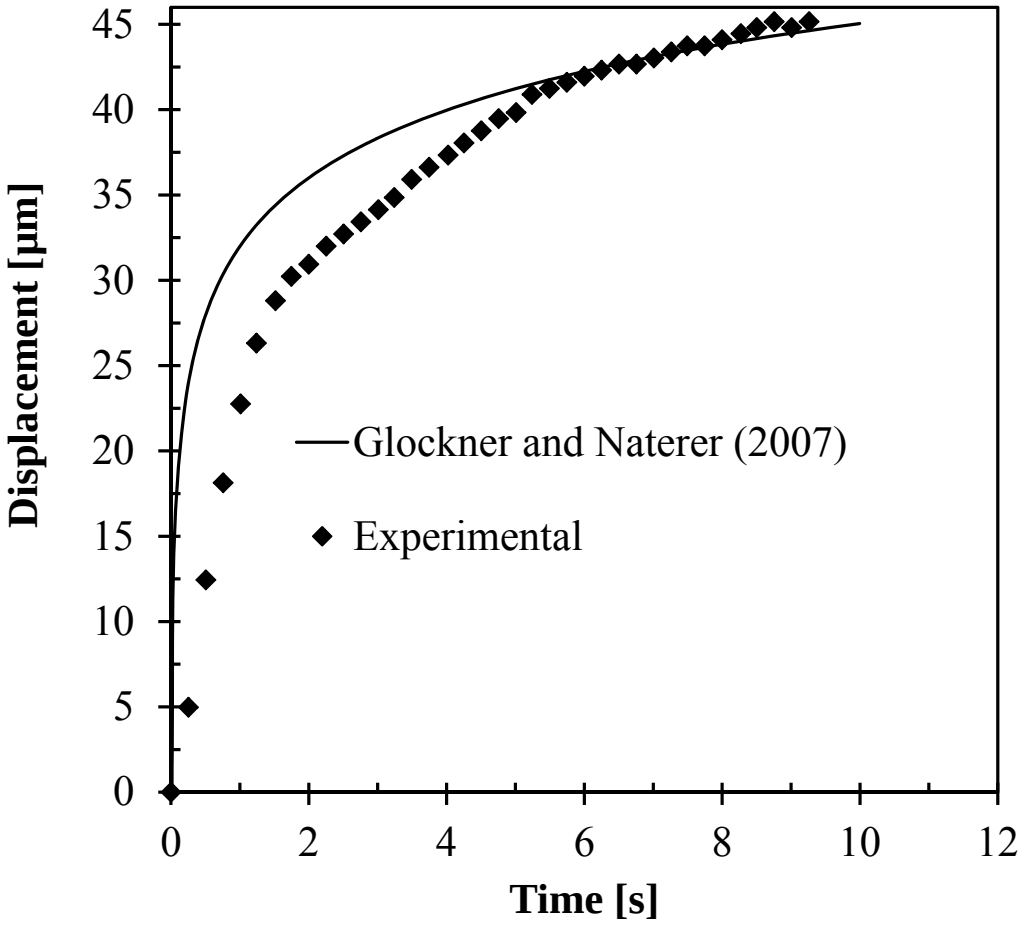

Figure 6.3: Comparison between measured and predicted droplet displacement (16μm diameter channel; supply voltage of 700μV)

Figure 6.3 shows a comparison between the results of the present model and measured data for the displacement of the droplet in a closed microchannel. The speed of the droplet after the initial heat input to the channel is rapid, but it decreases once the effect of back pressure from the opposite end of the closed channel increases. The initial speed of the droplet over a period of 2.3s is about 13μm/s. Once the droplet reaches a uniform velocity, the displacement is accurately predicted by Equations (5.24) and (5.25).

However, during the transition period between the initial droplet acceleration and subsequent stage of uniform velocity, the force balance over-predicts the droplet displacement, because the droplet motion has not yet reached a uniform velocity.

Also, the method neglects the activation energy needed to first overcome the frictional resistance of the droplet, before the droplet begins moving. It also provides a useful and reasonably accurate model over the entire range of droplet motion, including the transition between initial and uniform velocity stages.

6.2 Effect of surface roughness

The main effect of surface roughness on flow in the microchannel is altering the "effective viscosity" of the droplet. Any changes in viscous force will affect the pressure gradient across the channel as can be seen from equation (5.23). The effective viscosity is inversely proportional to the Reynolds number of the flow of the droplet in the microchannel. Although the percentage variation is only about 1.5 % for the range of Reynolds number in this study, the impact at this scale can have a significant effect on the frictional force. The effective viscosity increases as the Reynolds number increases for open channel flow [151], but the reverse occurs for the closed channel. This is due to the restraint of the fluid flow as the droplet moves towards the right end of the channel. The effect of the viscosity decreases towards the centre of the droplet, due to diminishing effects of the boundary layer in the radial direction. The frictional force variation for different local roughness Reynolds numbers (Re_{ek}) is indicated in Figure 6.4. The choice of Re_{ek} is based on measurement of the roughness height, which varies from 2-3μm as measured for different samples of the PZT substrate. The frictional force increases with

an increase in the roughness height as observed in Figure 6.4, which is a result of the increase in local roughness mean velocity.

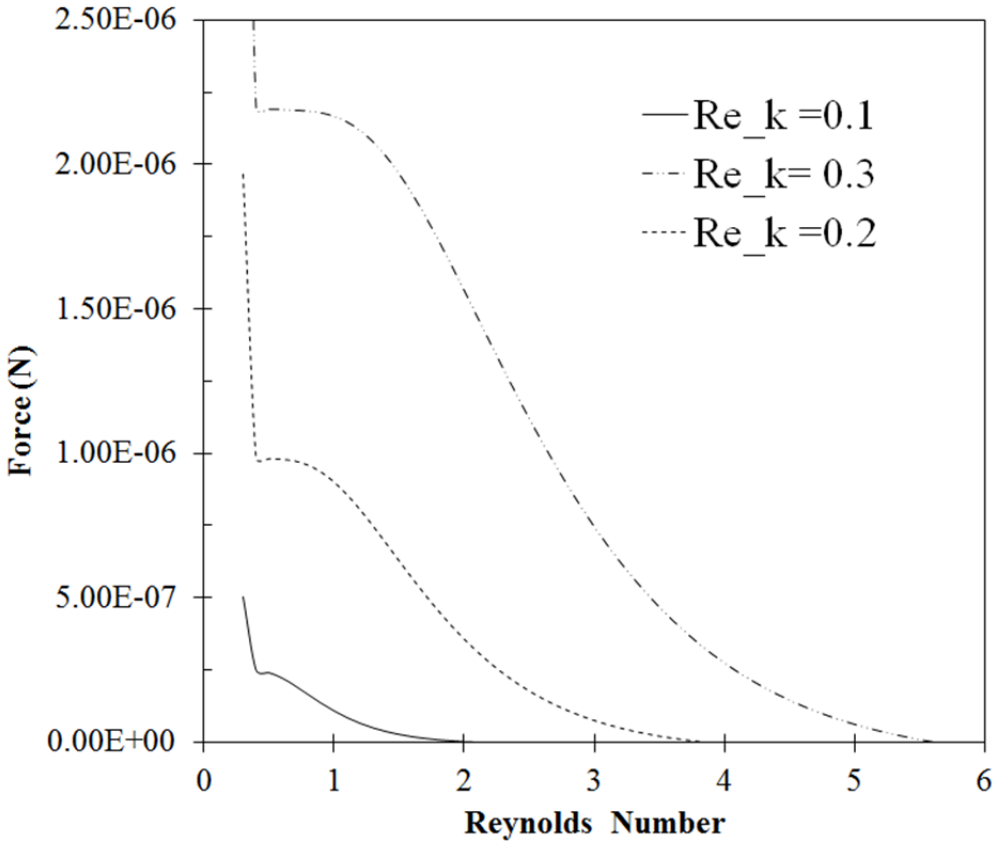

Figure 6.4: Effect of local roughness Reynolds number on frictional force in a closed circular microchannel (16μm closed microchannel)

The frictional force is doubled for an increase of Re_{ek} from 0.1 to 0.3. This further indicates the importance of the effect of surface roughness on the droplet displacement in the microchannel. The frictional force is inversely proportional to the bulk Reynolds number of the flow. The average bulk velocity increases with Reynolds number, thereby reducing the impact of the frictional force on the bulk motion of the droplet. The frictional force is much smaller than other forces acting in the microchannel, as can be observed in Figure 6.5. The capillary force is the main force that drives the motion of the droplet.

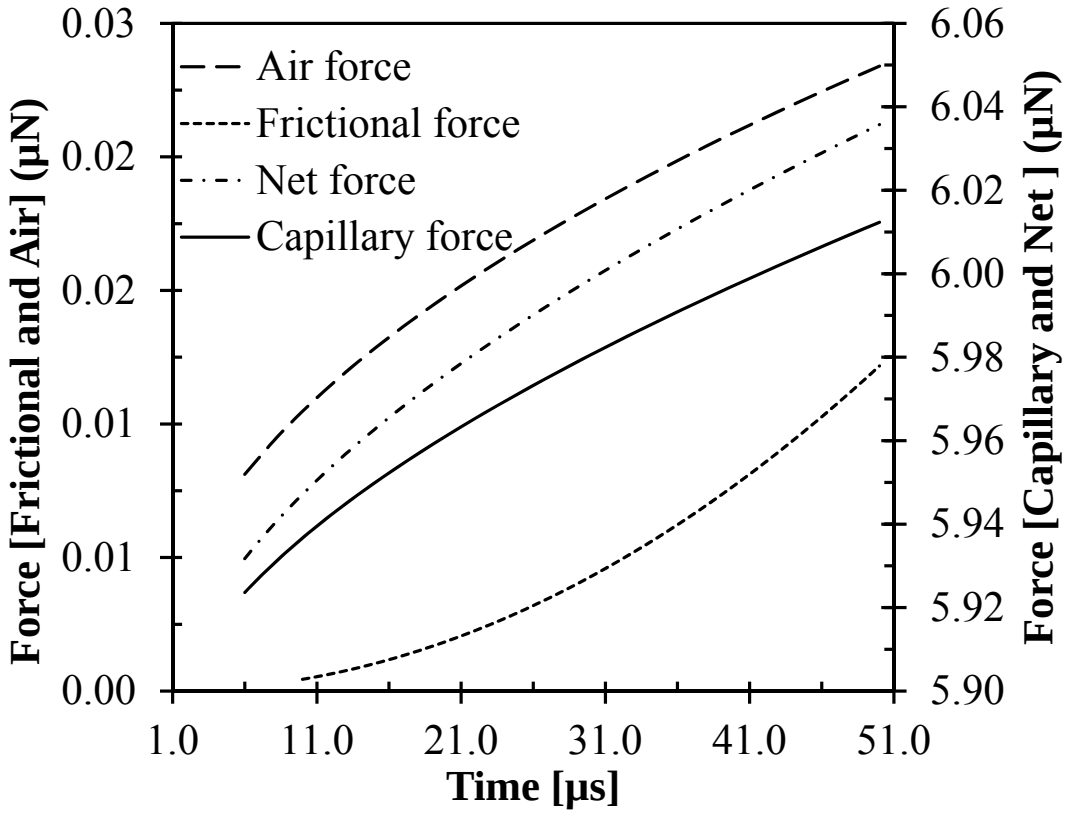

Figure 6.5: Distribution of forces during a heating cycle of the MHE

As expected, it increases rapidly as heat is added to the droplet. The air force and frictional force act in opposite directions of the capillary force as the droplet moves toward the right end of the channel. The combined effect of air and frictional forces reduces the bulk velocity of the droplet to zero. The frictional force leads to irreverisbilities in the MHE, to investigate the combined effect of irreversibilities and entropy generation in the MHE. The next section examines the entropy production in the micro heat engine.

6.3 Entropy generation in a cylindrical microchannel

Friction and thermal irreversibilities are characterized by the entropy production rate. These have significance for understanding and controlling the energy conversion

mechanisms in practical applications of the microchannel device. The effect of the Reynolds number on the entropy generation in the microchannel is shown in Figure 6.6. The entropy generation decreases with an increase in Reynolds number. The entropy generation is slightly lower as the droplet moves further away from the heat source due to the increased external air pressure and reduced acceleration of the droplet.

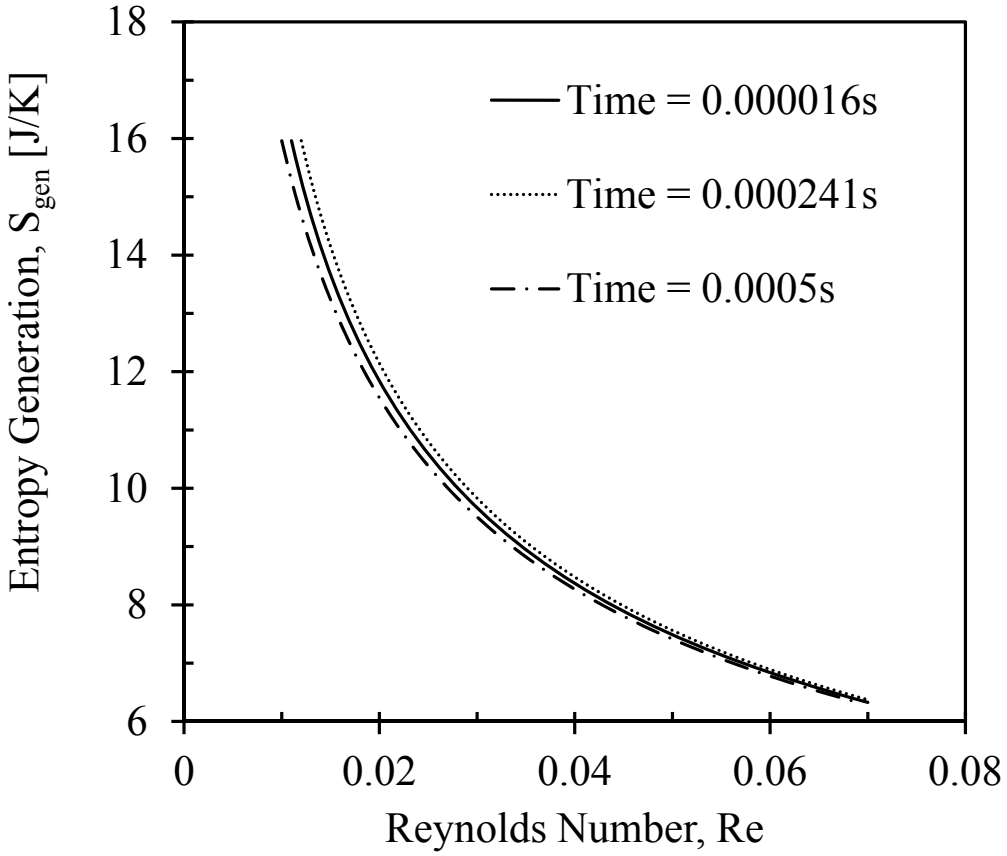

Figure 6.6: Entropy generation at different times for droplet flow in a circular microchannel (16 micron diameter channel)

The entropy generation as a result of heat transfer is highest at the initial displacement of the droplet. When the droplet moves away from the heat source, the velocity is reduced due to the closed end of the channel on the right side.

At low Reynolds numbers, the thermal irreversibilities are higher because a high temperature difference occurs over as shorter length for a fixed heat flux. The optimum Reynolds number for the closed channel is directly proportional to the change of B_o as indicated in Figure 6.7. The optimal diameter increases at higher values of B_o, consistently with previous results of Bejan [128].

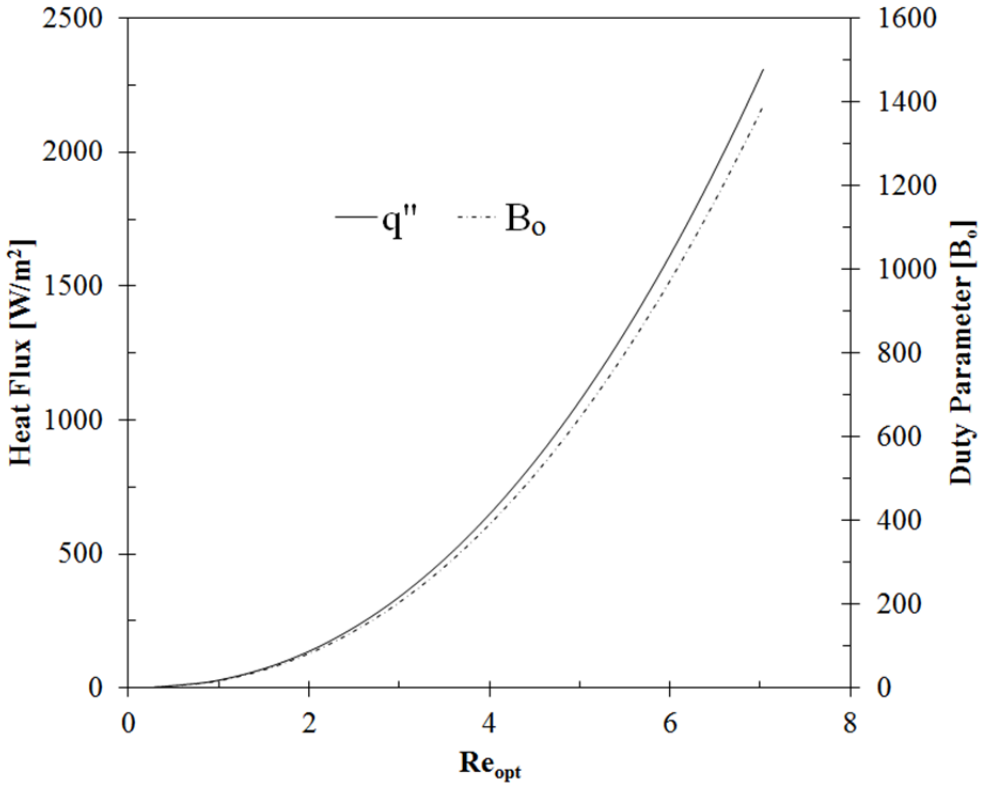

Figure 6.7: Effect of duty parameter on the optimum Reynolds number

The effect of changing the heat flux as a result of the change in B_o is also shown in Figure 6.7. The optimum Reynolds number for the closed microchannel is dependent on the product of the heat flux and mass flow rate, as can be observed from equation (5.35). However, since the heat flux is constant, there exists a unique Re_{opt} in each case, which can be used to design the microchannel for minimum entropy generation.

The time elapsed has little effect on the entropy generation number. The total change in entropy generation number over the range of time is about 2.65%. When Re is less than the optimum Re, the entropy generation as a result of heat transfer is larger. When Re is larger than the optimal Re, the viscous stress has a more significant effect on entropy generation due to more dissipated kinetic energy as a result of the increased velocity and friction over a larger surface area. This yields an optimal Reynolds number in a certain range where the effect of droplet velocity will minimize the entropy generation.

The effect of time elapsed is more pronounced, as the difference in the ratio of the diameters, over the range of time, is about 5.5%. At the initial stage of droplet motion, the effect of heat transfer is larger on entropy generation, as compared to the latter stage of droplet motion. The effect of viscous stress is more significant at 0.0005s, as compared to the initial motion of the droplet. The entropy generation number shows a trade-off between heat transfer irreversibilities and frictional irreversibilities near the optimal Reynolds number. This trade-off is used to optimize the dimensions of the channel.

A change in heat flux will also increase the interface temperature at the receding end of the droplet, which will lead to an increase of entropy generation across the channel. Increasing the heat flux may also make the droplet vaporise before the actual thermocapillary pumping occurs. The type of application would influence the heat flux required and supplied to the system. In this study, a minimum heat flux which will provide a maximum speed of the droplet is preferred. A comparison was also made to determine the effect of different fluids on the entropy generation number in the closed microchannel. Figure 6.8 shows a comparison of water, toluene and mineral oil for the

entropy generation number, with respect to time. The velocity and Reynolds number are changing with respect to time. Mineral oil produces the maximum entropy generation number, with respect to time. The minimum difference in magnitude of entropy generation number of mineral oil is about 74% larger than the entropy produced by using a toluene droplet, when observed at 0.0005s.

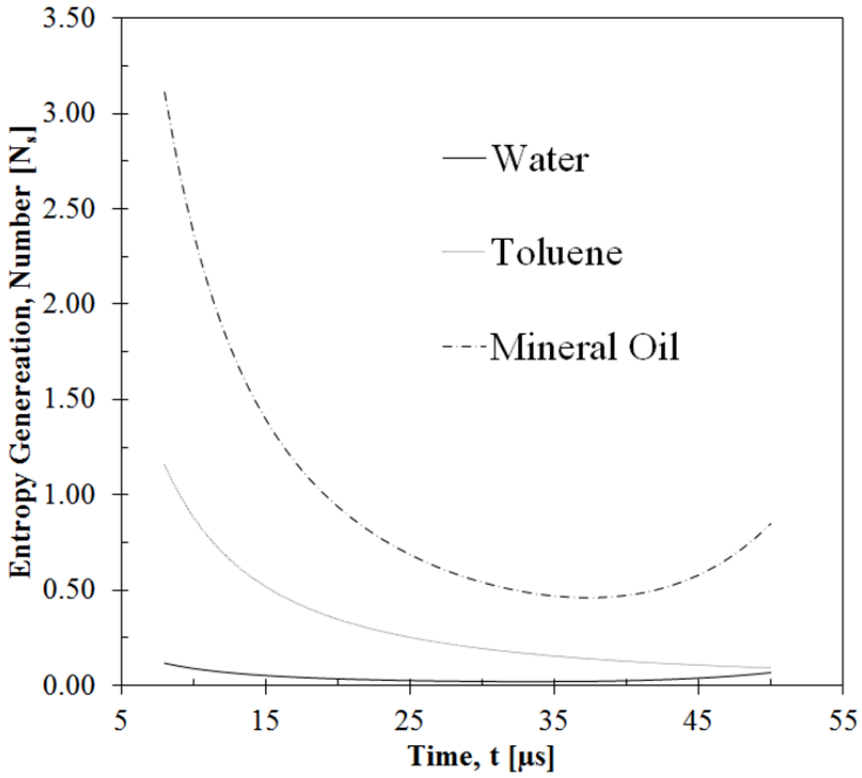

Figure 6.8: Entropy generation for different droplet compositions in a closed microchannel

When a toluene droplet is compared with the water droplet, a maximum 33% difference in entropy generation number is observed over the range of time. This can be attributed to the difference in specific heat capacity between both fluids.

The effect of droplet displacement on the entropy generation number is compared for various fluids in Figure 6.9. The most pronounced effect of displacement on the

entropy generation number occurs when mineral oil is used as the working fluid. The viscous stress on the droplet is larger when mineral oil is used as a working fluid. This increases the entropy produced when the droplet is displaced along the channel.

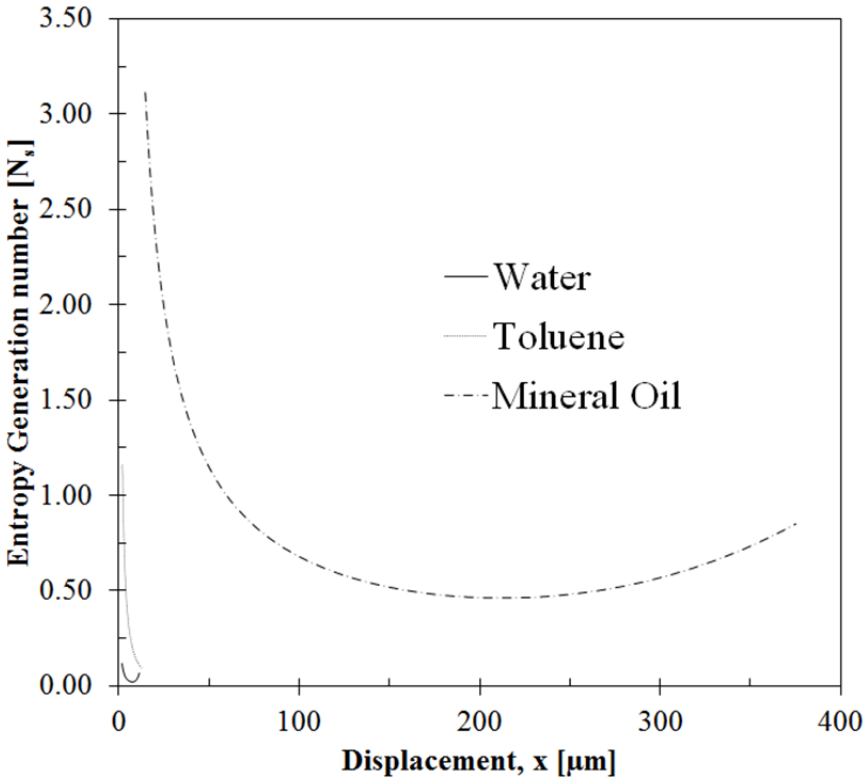

Figure 6.9: Entropy generation for different fluid droplets

The effect of displacement on entropy generation number is minimal between toluene and water. This indicates a possibility of using both fluids interchangeably, depending on the application. The actual entropy production with water as a working fluid is the lowest (see Figure 6.8). The entropy generation number is an important parameter to determine the optimal sizing of the microchannel.

The entropy generation number for closed and open microchannels in the laminar flow regime is compared in Figure 6.10. The entropy generation number in an open channel with the same amount of heat input is larger than results for a closed channel.

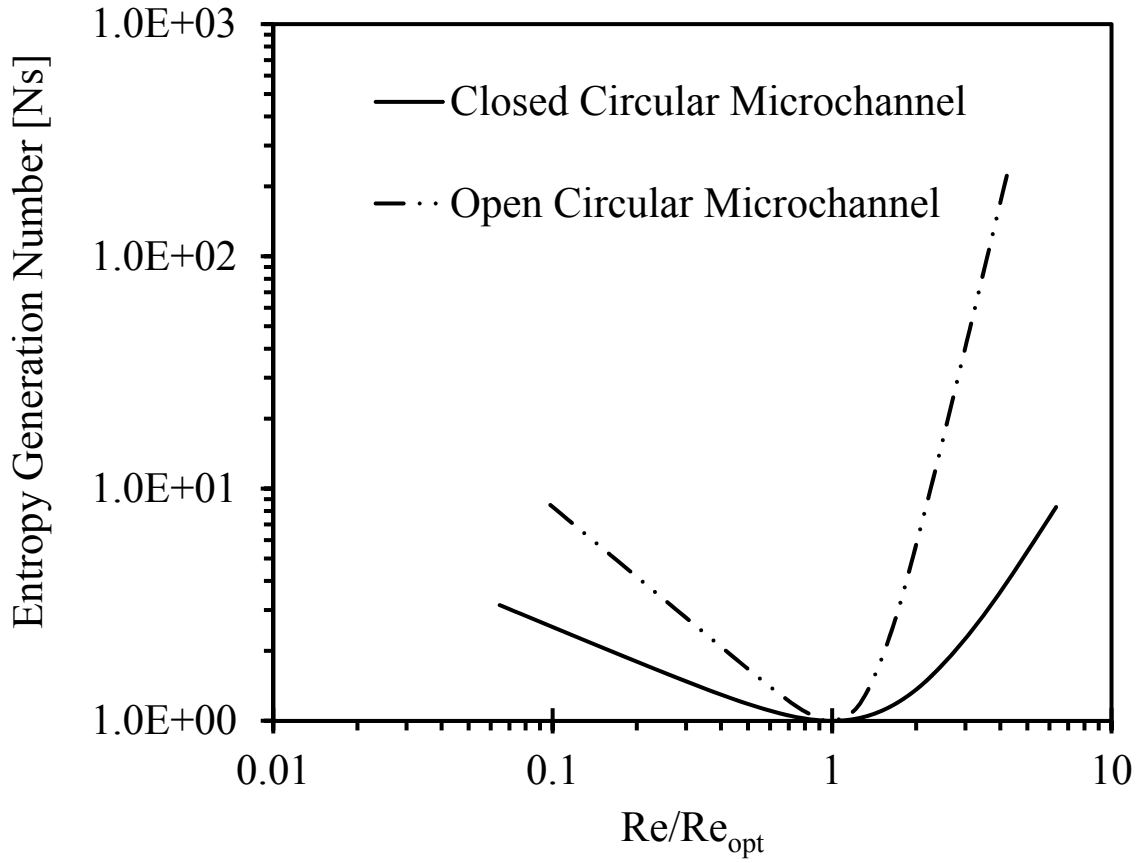

Figure 6.10: Entropy generation number in closed and open circular channels in the laminar flow regime

The model of Ratts and Rauts [133] for circular channel laminar flow is used to predict the entropy generation number in the open channel. The contribution of fluid friction to the entropy production has a more significant effect in the open microchannel, compared to the closed microchannel, where both thermal and friction irreversibilities are more similar. The effect of the resultant air pressure from the closed ends of the microchannel is responsible for the difference in entropy generation in the closed and open microchannels.

Minimizing the entropy generation will increase the energy efficiency of the intended application, which in this study is the MHE. The MHE uses the cyclic heating and cooling of the droplet to generate fluid motion and electric voltage from deflection of a piezoelectric membrane beneath the channel.

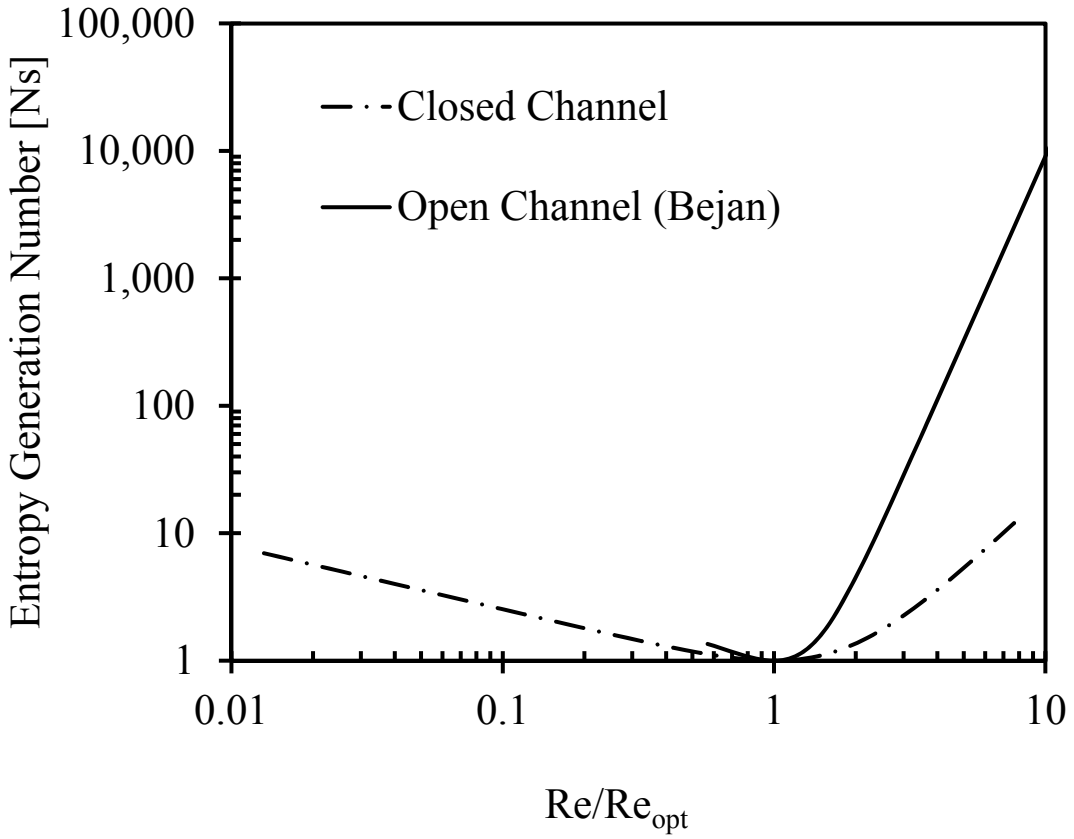

Figure 6.11: Entropy generation number of laminar and turbulent flow regimes for open and closed microchannels

Reducing the entropy production will increase the system efficiency and life cycle of the piezoelectric layer of the MHE.

The entropy generation number in the closed microchannel is compared to an open microchannel using Bejan's data for fully developed flow as shown in Figure 6.11. The comparison was made with equivalent problem parameters for the closed

microchannel, but the pressure drop across the droplet is only due to thermocapillary and frictional forces on the droplet. The Hagen-Poiseuille flow model was used to predict the frictional forces in the open microchannel.

The optimum Re differs significantly in terms of the order of magnitude, thereby making it difficult to provide conclusive information on the heat transfer contribution to the entropy generation. Below and above the optimum Re, the open microchannel flow has a larger entropy production as compared to the closed microchannel. The contribution of frictional irreversibility to entropy production is significant in both cases.

Once the irreversibilities in the MHE have been analysed, the results from this section were used for modelling of the voltage generation and efficiency of the MHE. Section 6.4 investigates the voltage production in the MHE and the possible efficiencies that can be achieved.

6.4 Voltage production and efficiency of MHE

Results will be presented for simulation of the droplet displacement in a closed 60 × 60 × 15,000μm rectangular microchannel. The properties used for performing the simulation can be found in Table 6.2. Figure 6.12 shows the effect of droplet displacement on the pressure exerted on the piezoelectric membrane and temperature of the droplet.

The change in pressure is rapid with initial displacement of the droplet, but the rate of change decreases due to the external air pressure from the closed end of the channel. The total pressure change is about 0.1kPa, which can be justified by the magnitude of deflection in the piezoelectric membrane as observed in Figure 6.13. The

maximum deflection is about 13µm, which is obtained from the piezoelectric with the largest thickness.

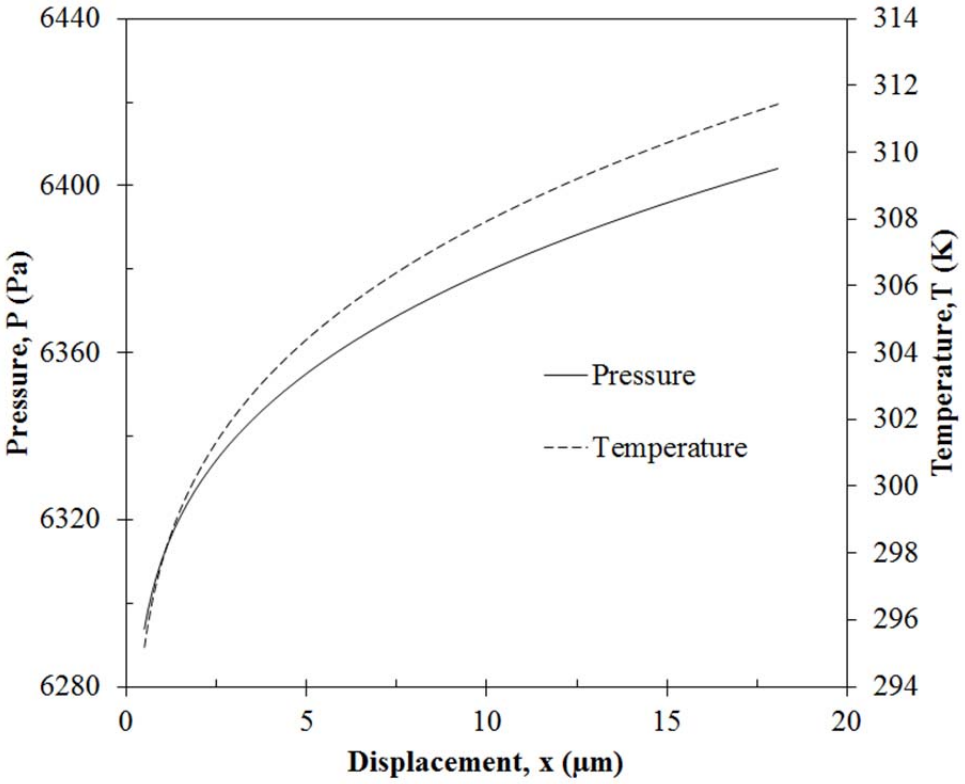

Figure 6.12: Effects of droplet displacement on temperature and pressure in the MHE [rectangular cross section (60 × 60µm)]

The change in deflection occurs in steps. It remains constant for a certain range of displacement for the different thicknesses. The overall change in deflection increases with a larger displacement of the droplet.

However, when the various thicknesses are considered for a specific displacement, the change is doubled between a thickness of 500 and 700nm, but only about 77% between 300 and 500nm. The voltage produced as a result of the deflection of the membrane was compared for the three thicknesses in Figure 6.14. The voltage

produced in the MHE is proportional to the thickness of the membrane, whereby the largest thickness produced the highest voltage, which varied between 1.2 and 1.3μV.

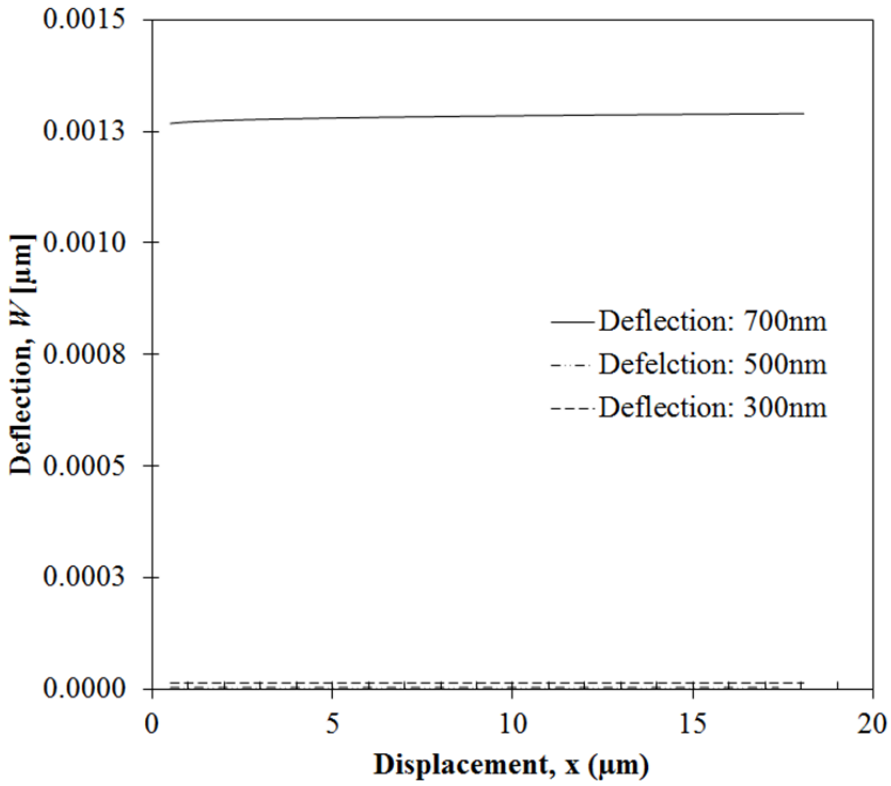

Figure 6.13: Effect of piezoelectric membrane thickness on deflection of rectangular thin membrane

The change in voltage for the range of displacements is about 1.7%. A steady supply can be achieved within a reasonable confidence interval. The lowest voltage produced was observed in the 300nm membrane, with a value of 0.5mV. The latter suggests that the thickness of the membrane can be used to control the application in which the MHE can be utilized. The voltage production is affected by the bulk velocity of the droplet. The transient velocity was investigated in order to predict the impact on the voltage production in the MHE. The predictive model was validated against past data by Muzychka [198].

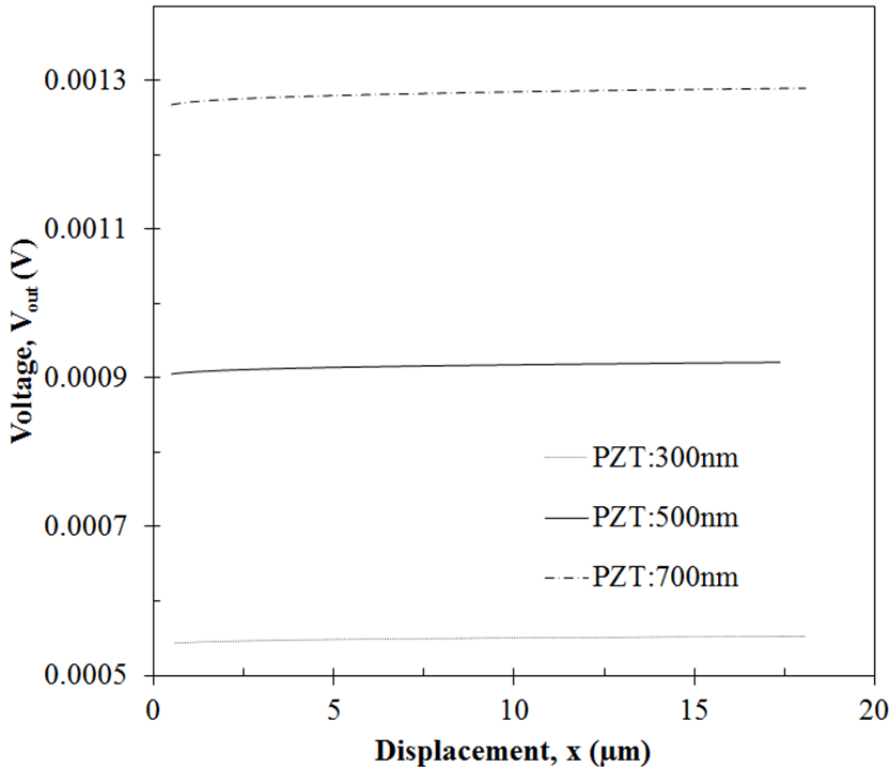

Figure 6.14: Effect of displacement of the microdroplet on the voltage produced for different piezoelectric heights

The dimensionless velocity was compared for different characteristic length scales, which affect the Reynolds number of the flow (Figure 6.15). For different aspect ratios, the trends show good agreement with Muzychka's model. The friction factor was also modelled in terms of the aspect ratio. Muzychka [198] correlation for the friction factor showed that when the aspect ratio is varied, the friction factor eventually attains an asymptotic value. Figure 6.16 verifies this claim. The correlation for the friction factor was derived based on Muzychka [198].

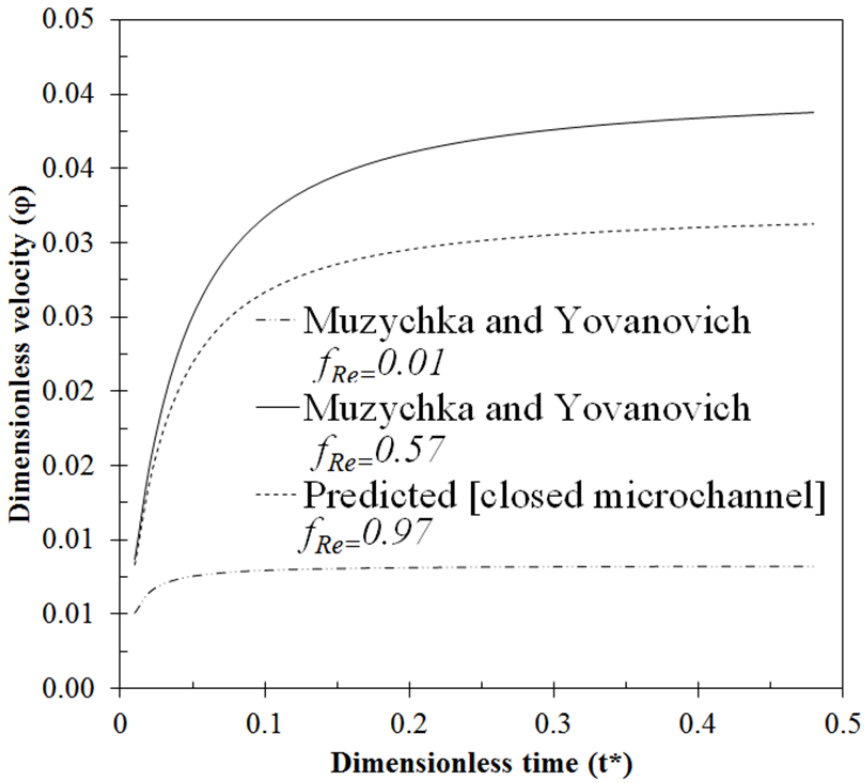

Figure 6.15: The effect of friction factor on dimensionless velocity for open and closed microchannels.

$$f_{\mathrm{Re}_{\sqrt{A}}} = \frac{12}{\sqrt{\Upsilon}(1+\Upsilon)\left[1-\frac{192\Upsilon}{\pi^5}\tanh\left(\frac{\pi}{2\Upsilon}\right)\right]} \tag{6.2}$$

where Υ is the aspect ratio of a rectangular channel. The transient velocity is compared with Poiseuille flow in Figure 6.17. It can be observed that the Poiseuille flow assumption overpredicts the bulk velocity of the droplet. At early time, the difference in velocities is minimal but a significant deviation is observed at about 30μs. The droplet quickly attains a maximum velocity in the transient model and but also decreases much faster than the Poiseuille flow assumption.

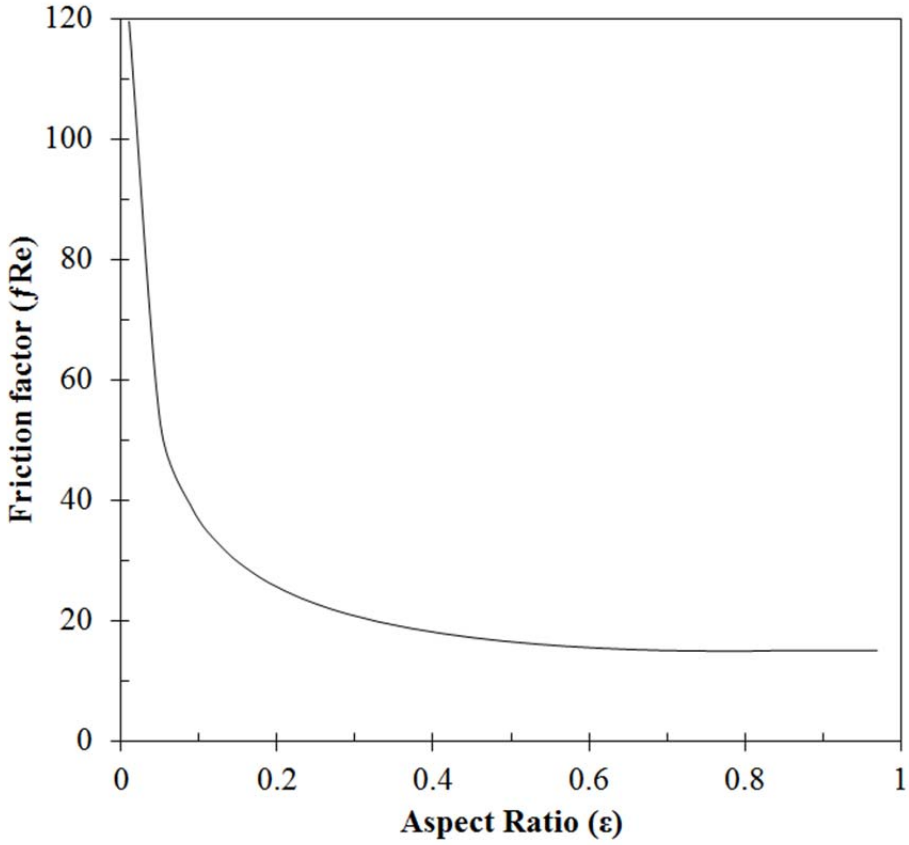

Figure 6.16: The effect of aspect ratio on friction factor in microchannels

The maximum variation in the velocity when the droplet is advancing is about 33%. The droplet stops in about half the time observed as the Poiseuille flow assumption, which indicates a faster response time will be achieved in the MHE. Over predicting the velocity of the droplet affects the predicted voltage from the MHE. Figure 6.18 shows a comparison of the effect of the transient and Poiseuille flow assumption on voltage production in the MHE. The output voltage is overpredicted by the steady flow assumption by almost double its transient result. The corrected voltage can then be used to estimate the efficiency of the MHE. The effect of the displacement of the droplet on the efficiency of the MHE is shown in Figure 6.19. It can be observed that the trends are

similar to the observation in Figure 6.14. Thus, the voltage production is directly proportional to the system efficiency. The maximum efficiency is about 1.67% for the 700 nm membrane for the largest droplet displacement.

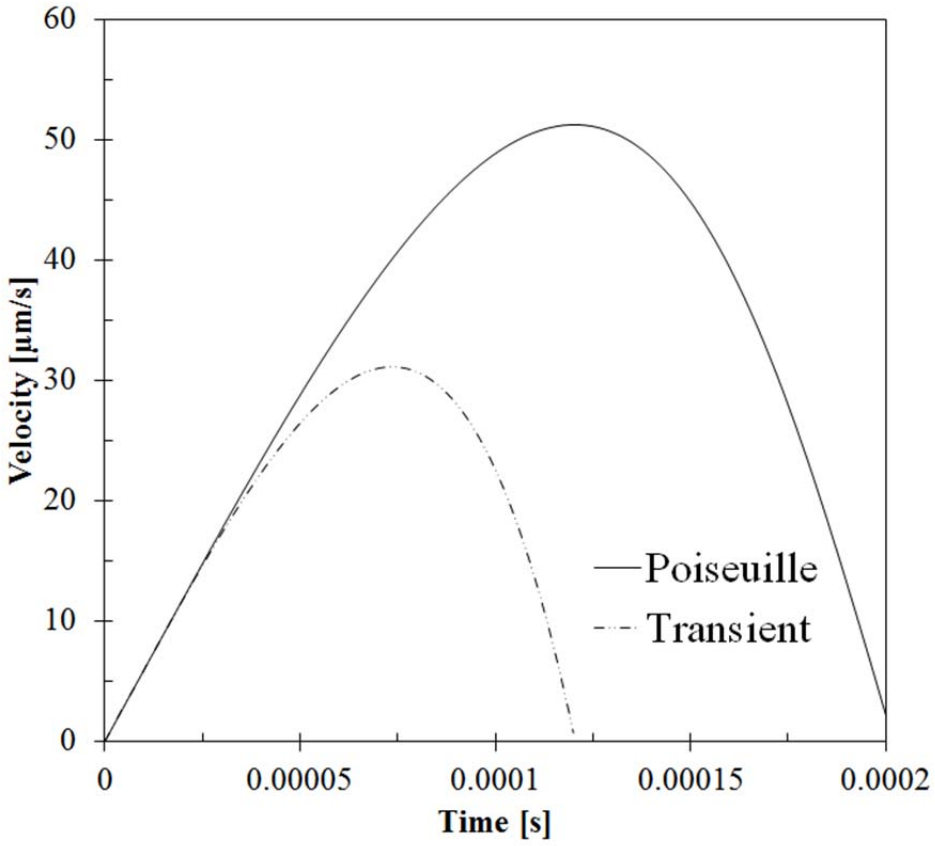

Figure 6.17: Comparison of the effect of the Poiseuille flow assumption and transient velocity in the MHE [rectangular cross section (60 × 60µm)]

The minimum efficiency observed is about 0.7% for the 300nm membrane. The total change in efficiency is about 0.02% for the range of droplet displacements. It should be noted that a compromise must be made between efficiency and cost of the material and fabrication.

A comparison was done between the dimensionless voltage produced from the MHE and the bimorph energy harvester [154] (see Figure 6.20). The effect of pressure on the voltage produces similar trends in both energy harvesters. The power produced from the bimorph harvester was about 10 orders of magnitude greater than the power produced from the PZT membrane.

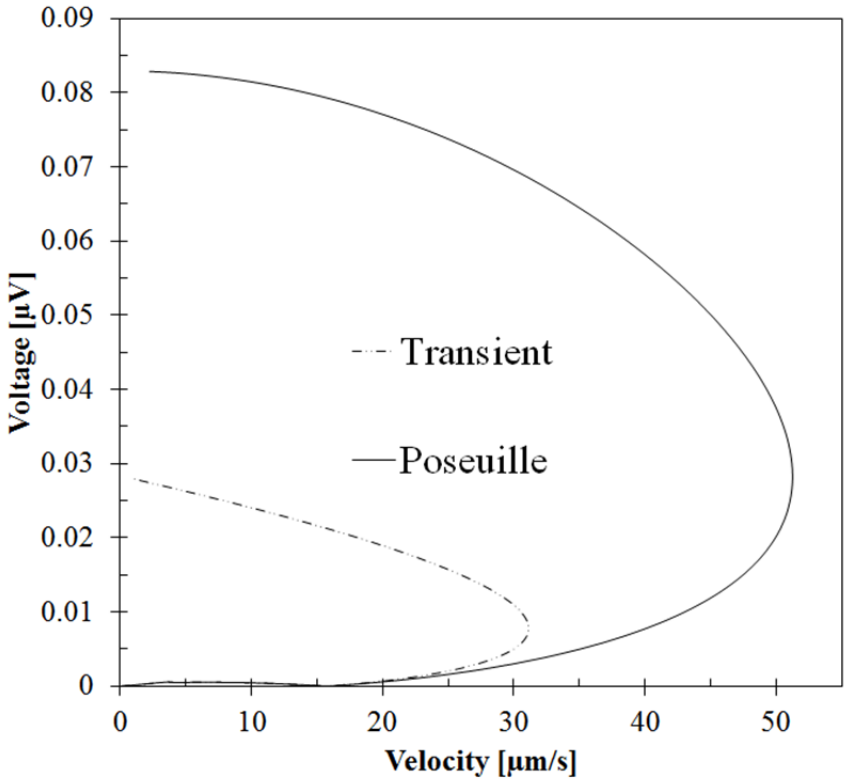

Figure 6.18: Comparison of the effect of the Poiseuille flow assumption and the transient voltage generated in the MHE [rectangular cross section (60 × 60µm)]

The thickness/length ratio is much larger in the bimorph cantilever, which will also require a large loading to produce any deformation. Figure 6.21 shows a comparison for different piezoelectric membranes for similar dimensions to the PZT membrane. The zinc oxide (ZnO) piezoelectric produced the maximum voltage of about 7.6µV for the deformation considered in this study. These results may not be accurate for ZnO and

lithium niobate ($LiNbO_3$) as the true voltage generation will depend on the nature of the deposited materials on the substrate. These were considered for PZT. $LiNbO_3$ was originally tested as a substrate for the MHE, but etching it without damaging the existing patterns could not be achieved.

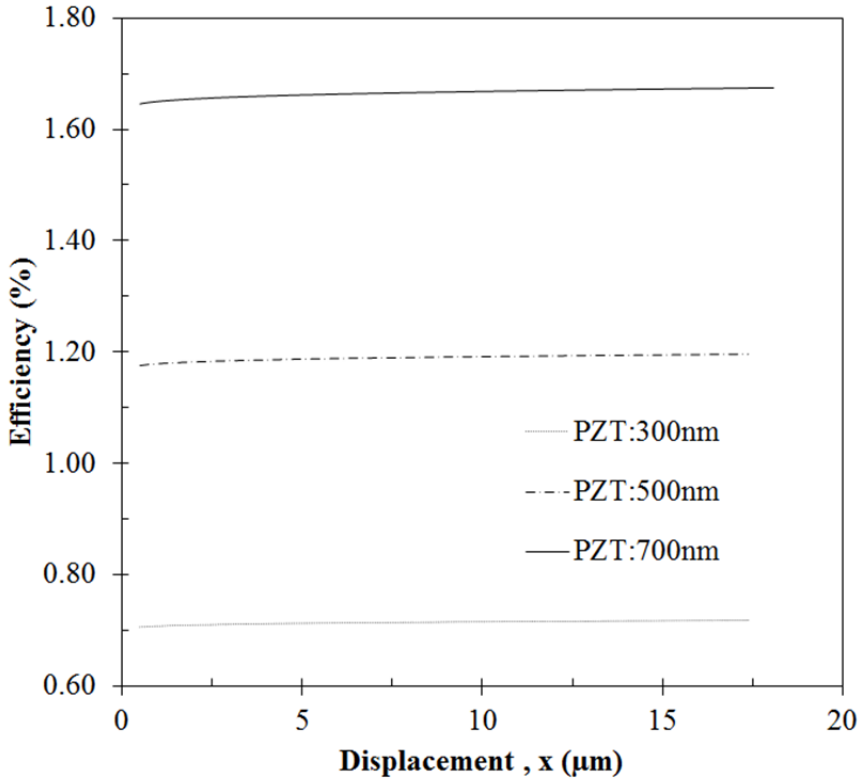

Figure 6.19: Effect of droplet displacement on the efficiency produced in a MHE for various heights of piezoelectric membranes

The substrate is supplied for a thickness of 500µm and etches only in a heated bath of hydrogen fluoride, which is toxic and will etch almost any metal deposition. The etching $LiNbO_3$ also leaves a very irregular surface finish, which cannot be controlled and will result in high surface roughness. The fabrication of the MHE was not as successful as initially anticipated.

Table 6.2: Parameters and thermophysical properties for rectangular channel with PZT substrate

Property	**Value**
Conductivity of droplet	0.606W/mK
Height of droplet	60μm
Height of air	60μm
Height of substrate	500 μm
Thermal diffusivity	$4.588m^2s^{-1}$
Thermal conductivity of air	0.0263W/mK
Conductivity of substrate	0.96W/mK
Heat transfer coefficient	$4.82Wm^2/K$
Heat flux	$3.423W/m^2$
Density of droplet	$998kg/m^3$
Density of substrate	$2,500kg/m^3$
Density of air	$1.16kg/m^3$
Length of channel	15mm

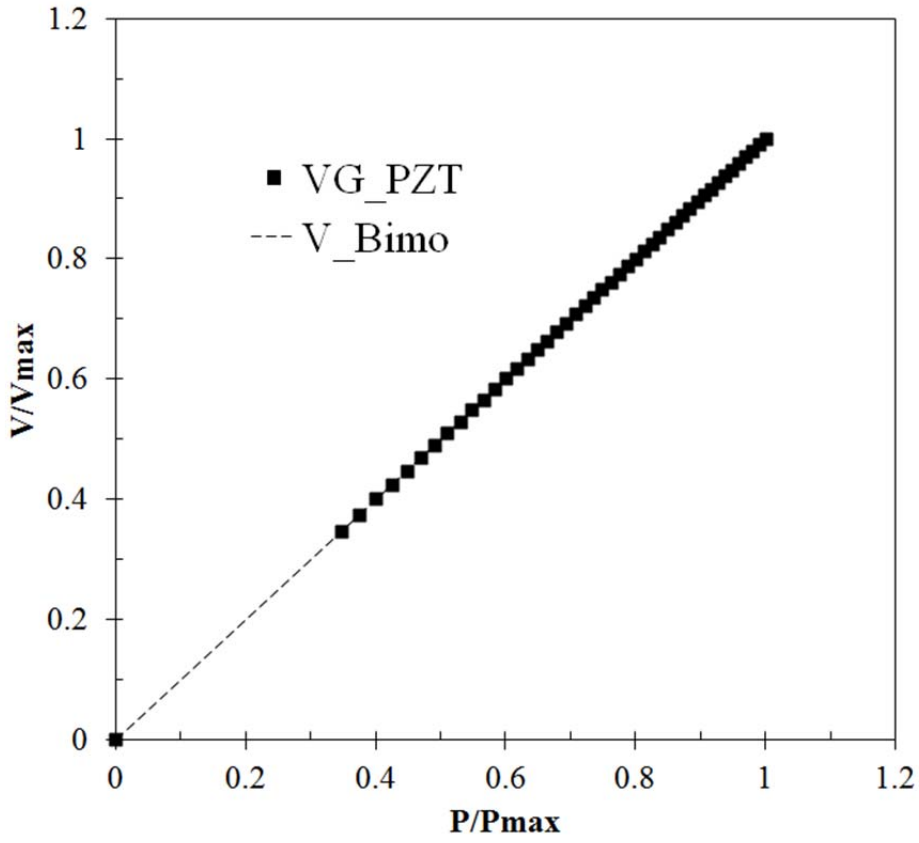

Figure 6.20: Dimensionless comparison of voltage output from a cantilever bimorph membrane energy harvester (Kimberly *et al.* [154]) and the MHE [rectangular cross section (60 × 60μm)]

Sealing the microchannel after injecting the droplet was drawback in the fabrication process. Evaporation of the droplet during the sealing process was a setback in successfully analysing the experimental efficiency of the MHE.

Despite these challenges, experimental data was obtained to analyse the power supplied to the MHE. Also, and experimental results were obtained to analyse the evaporation process. The next section presents and discusses the experimental and predicted results from the MHE.

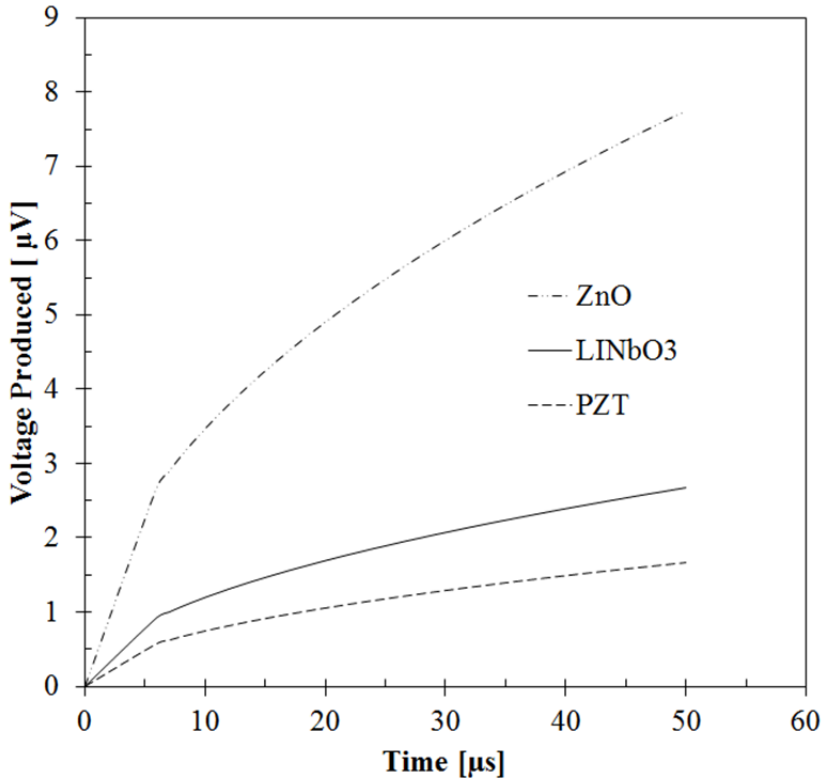

Figure 6.21: Effect of different types of piezoelectric films on voltage produced in the MHE [rectangular cross section (60 × 60µm)]

6.5 Experimental and predicted results of microheaters

A four point probe test was used to determine the sheet metal resistance of Ti-W. The resistivity of Ti-W sputtering deposition varies with residual stress as a result of the deposition process and the pressure at which it is deposited (5.6×10^{-6}Torr). The resistance can be estimated based on the sheet metal resistance.

$$R = \rho\left(\frac{L}{w}\right) \tag{6.3}$$

where ρ is the sheet metal resistive obtained from the four probe measurement, and w and L are the width and the length of the heater, respectively. Based on the estimated

resistance in equation (6.3), the actual heat flux transferred to the heater is estimated from the measured contact area of the heaters and channels.

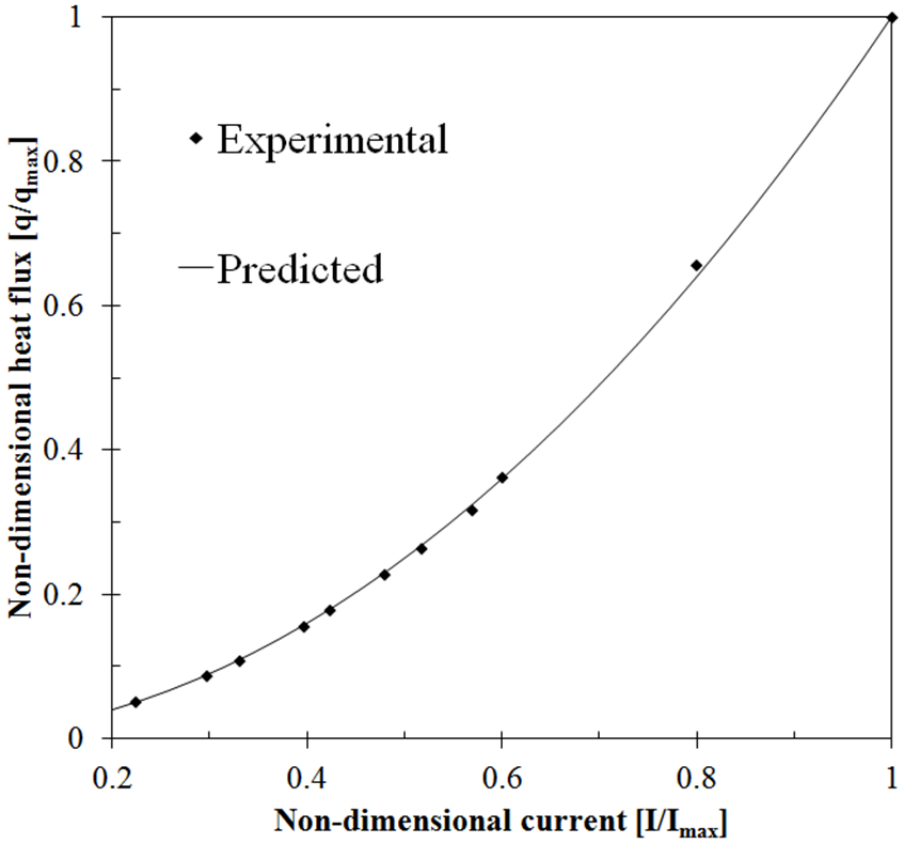

Figure 6.22: Comparison of experimental and analytical results of heat supplied to the MHE

The predicted model uses equation (6.1) to estimate the expected resistance of Ti-W. The resistivity cited in past literature [204] is used to estimate the heat flux into the system. The measured resistivity of Ti-W from the experiment varies between 21 and 31Ω/m^2 for a deposition of 138nm. A previous study at the CIRFE Lab for the same sputtering target was reported as 40Ω/m^2 for a 50nm deposition.

The resistance is inversely proportional to the thickness of the deposition. Figure 6.22 shows a non-dimensional comparison between experimental and analytical data for

the power supply to one microchannel. This is analogous to the non-dimensional heat flux supplied to one microchannel.

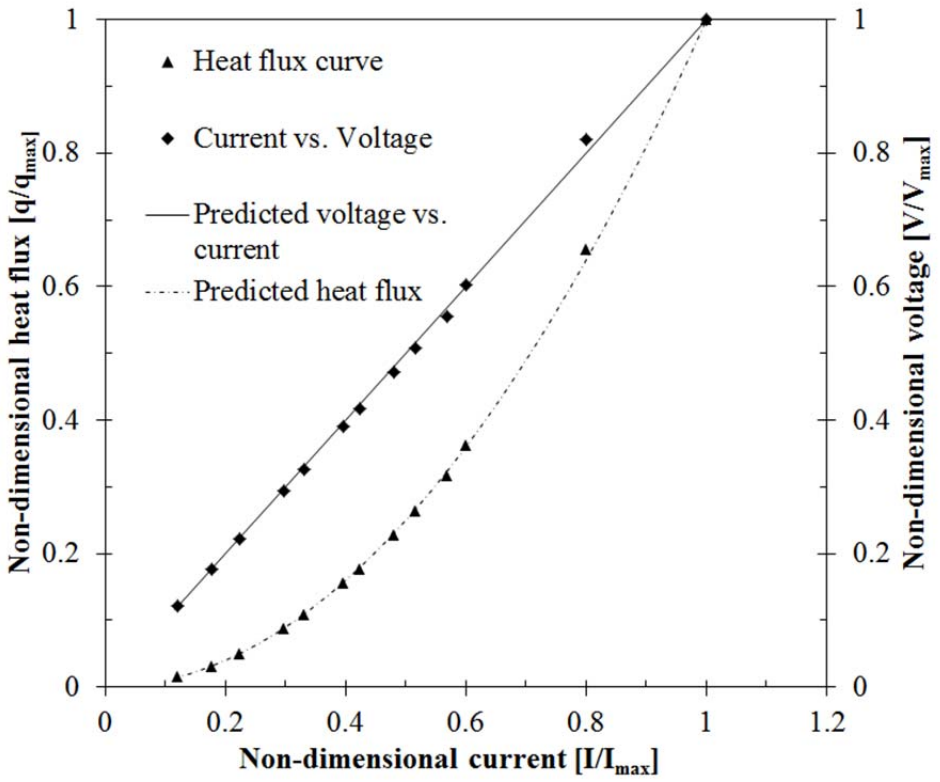

Figure 6.23: Comparison between experimental and analytical measurements of the heat flux and voltage supplied to the MHE

The heat flux curve in Figure 6.22 shows the relationship between voltage and power supplied to the heaters. The experimental and predicted results have good agreement. The deviation from the predicted results can be associated with the irreversibilities in the connections and heat losses to the substrate and surroundings. A non-dimensional comparison is done by the measured voltage, current and heat flux in Figure 6.23. The resistance of the Ti-W heater was estimated to vary between 893-918kΩ for the range of measured voltages across the heater. This is used to estimate the actual sheet resistance of Ti-W. The predicted and experimental measurements are in good

agreement for the range of voltages in the four point probe test. The maximum variation in the resistance is only about 2.7%, which indicates the uniformly distributed heat flux could be achieved for a wide range of heat input. The measured heat flux supplied to each microchannel was between 1.2 and 120μW/m^2. Continuous supply of voltage did not show any motion in the channel. This led to a study of the physical phenomenon associated with droplet evaporation in the microchannel. The next section shows results from evaporation of the droplet in the microchannel.

6.6 Experimental and predicted results of droplet evaporation

This section presents results on the evaporation of a droplet in a rectangular microchannel. Two different wetting fluids were investigated to examine the evaporation in the microchannel. Earlier investigations by Glockner and Naterer [1, 2] suggested that the two best fluids for thermocapillary pumping were toluene and water. Toluene was initially not recommended as a viable fluid because it is toxic. It is particularly interesting to note that toluene is completely wetting when injected into the SU-8 channel. DI-water was used for this experiment to avoid the effects of the electric double layer caused by charges present in regular water.

DI-water is partially wetting when injected into the microchannel, making it partially hydrophobic in this test case. The pattern of evaporation of DI-water and toluene is shown in Figures 6.24 and 6.25 respectively. When DI-water is injected into the microchannel, the bulk fluid is separated from the pinned film as shown in Figure 6.24(a), due to the hydrophobic nature of the fluid with the SU-8 vertical walls. After about 0.92s, the bulk fluid spreads across the width of the channel, reducing the separation distance between the bulk fluid and the pinned film as shown in Figure

6.24(b), due to the evaporation of the bulk fluid. In other to maintain constant volume, the droplet spreads along the width of the microchannel. After about 3.32s (Figure 6.24), the rate of change in width of the bulk fluid reduces significantly, when comparing the change in width with that observed in Figure 6.24(d), which represents the end of the evaporation of the bulk fluid.

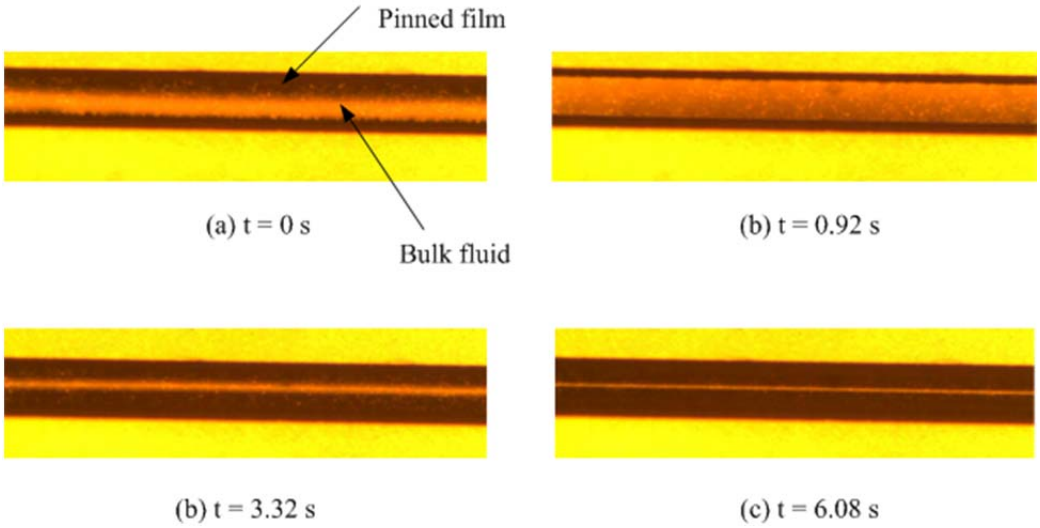

Figure 6.24: Evaporation of a DI-water droplet in Su-8 2075 between 0 and 6.08 s

The evaporation of the bulk fluid in the case toluene evolves in a different pattern since it is completely wetting to the PZT substrate and SU-8 vertical walls. Figure 6.25(a) further establishes the latter claim as the pinned film is not visible. After about 0.76s (Figure 6.25(b)), the pinned film can be observed, indicating a separation between the pinned film and bulk fluid. The evaporation of the bulk fluid initially occurs only across the width, but after about 2.76s, the bulk fluid starts to evaporate along the length as shown in Figure 6.25(c). The complete evaporation of the bulk fluid occurs after about 3.76s as observed in Figure 6.25(d).

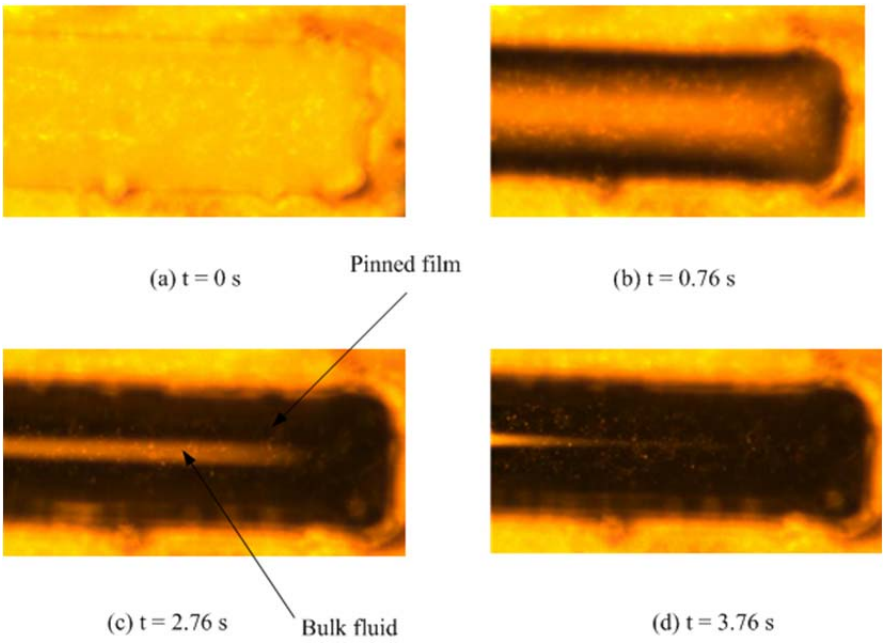

Figure 6.25: Evaporation of toluene droplet in Su-8 2075 between 0 and 3.76s

A non-dimensional comparison of the evaporation of DI-water and toluene is shown in Figure 6.26. Toluene evaporates much faster than water, but exhibits similar trends as can be observed in Figure 6.26. The analytical model yields the correct trend of the evaporation, but does not accurately predict the evaporation rate for water in the early stages of evaporation. Accounting for the analytical prediction of the separation distance between the pinned film and the bulk fluid during evaporation remains a challenge. The separation distance is dependent on the depth, width and surface roughness of the channel. Smaller channels were observed to have larger separation distances, which indicate a higher surface tension in smaller channels.

DI-water tends to maintain its width for about half the time of the evaporation cycle (8s), before a significant reduction is observed. The effects of surface tension of water and the hydrophobic nature in this experiment are responsible for this deviation from the analytical model. Toluene is completely wetting and has a lower surface tension,

hence it evaporates much faster than DI-water. The total evaporation of the bulk fluid occurs in about 3.5s, but the de-pinning process takes a slightly longer time as a result of the strong adhesive force between the pinned film and substrate. The surface roughness also enhances the adhesion of the pinned film to the edges of the channel.

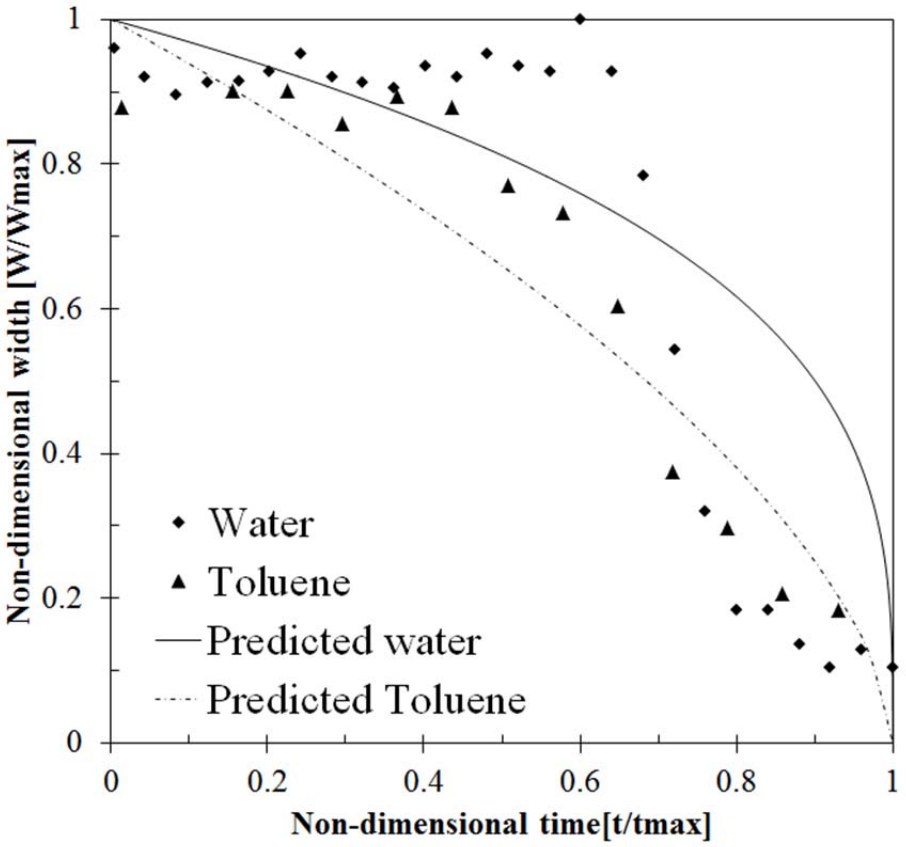

Figure 6.26: Comparison of experimental measurements and analytical predictions of evaporation in the rectangular microchannel

The effects of the height of the microchannel was also investigated and reported in Figures 6.27 and 6.28. The change of height of the channel for a fixed width can be associated with a change in volume of the droplet. The mass transfer of the droplet is not significantly affected by a change in depth of the channel as revealed in Figure 6.27 and

6.28. A reduction of the height by a third of its original height only resulted in a 1s drop in the evaporation time.

This shows that a change in height of the channel does not have a significant effect on the evaporation in the rectangular channel. The surface area of the channel exposed to the atmosphere has a more significant effect on the evaporation rate. The diffusion of the fluid takes place at the surface in contact with air directly in contact with the fluid. The evaporation rate can be modified by controlling the relative humidity in the vicinity of the ambient air surrounding the channel.

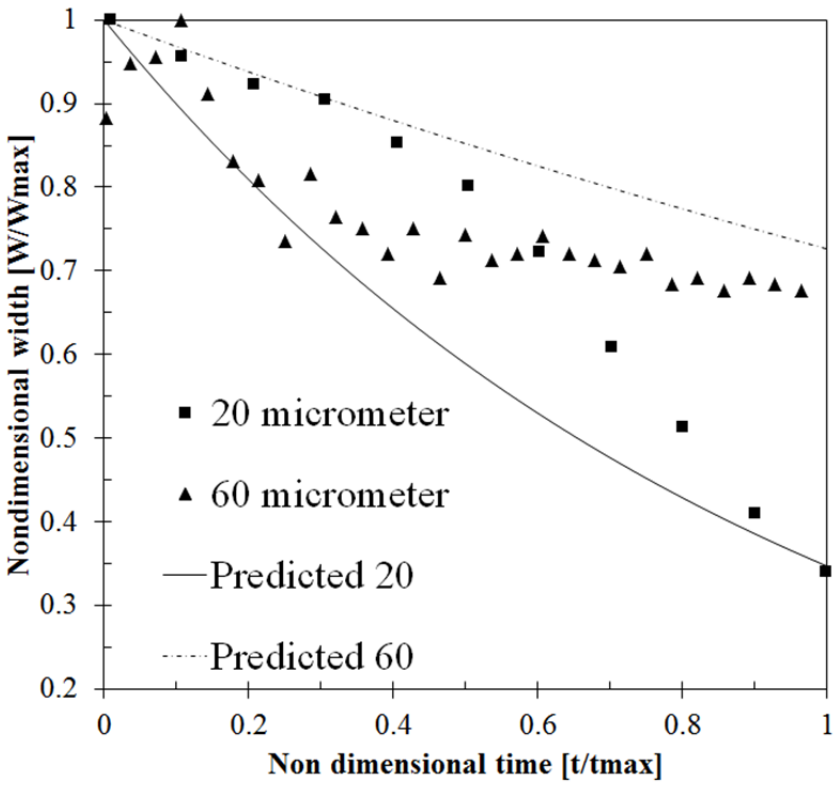

Figure 6.27: Comparison of experimental measurement and analytical prediction of evaporation of DI-water in a rectangular microchannel of different depths

However, it does have a significant effect on the pinning. This occurs due to the separation distance between the bulk fluid and the pinned film as shown in Figure 2.1.

The roughness height has a significant effect on the pinned film as a result of the decrease in microchannel depth. This can also be attributed to the surface tension forces that are larger in the smaller channel, since the surface tension force is inversely proportional to the depth of the channel. A reasonable agreement can be observed from the experimental and predicted result as shown in Figure 6.28.

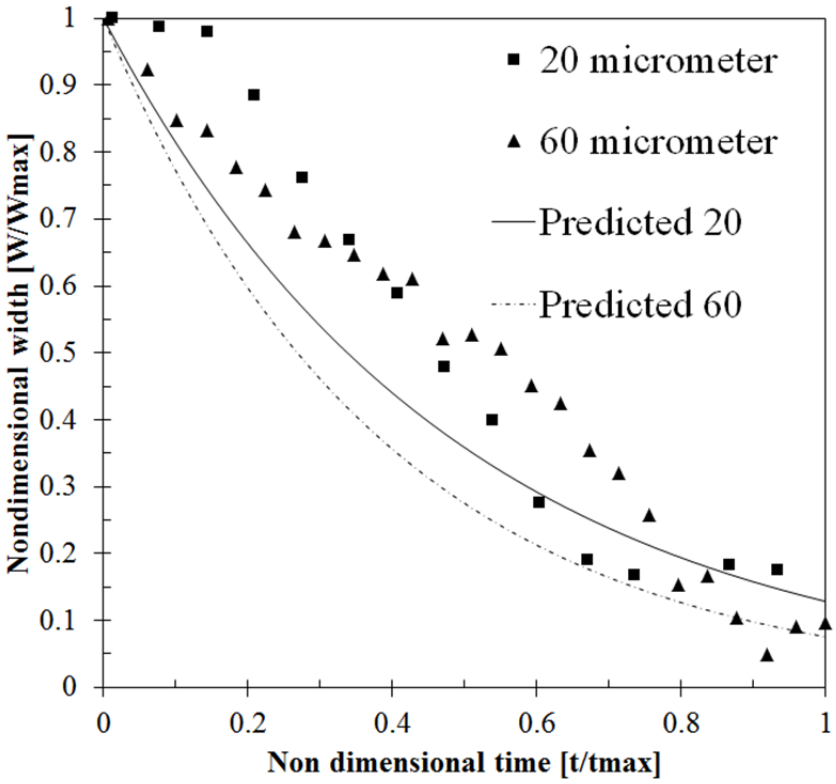

Figure 6.28: Comparison of experimental measurements and analytical predictions of evaporation of toluene in a rectangular microchannel of different depths.

The change in the contact and pinned film angles are shown in Figure 6.29. The bulk fluid evaporation contact angle varies between 41 and 47 degrees. The variation in contact angle is as a result of the droplet trying to maintain constant volume due to mass transfer from the droplet surface. The change in angle of the pinned film corresponds to an increase or decrease in the contact angle of the bulk fluid. The pinned film angle

varies between 40 and 47 degrees. The larger channels have a higher rate of evaporation initially due to the surface area of the channel, but after about 7.5s, the effect of surface area is not significant for the range of time considered.

The contact angle with the surface will depend on the nature of the surface of the substrate and the properties of the channel wall. Although DI-water is hydrophobic to SU-8, it is hydrophilic to PZT. Toluene has a contact angle of zero since it is completely wetting. The effects of contact angle and channel width on the evaporation rate are reported in Figure 6.30. A reduction in contact angle results in a decrease in the evaporation rate of the droplet. Increasing the width increases the evaporation rate of the channel.

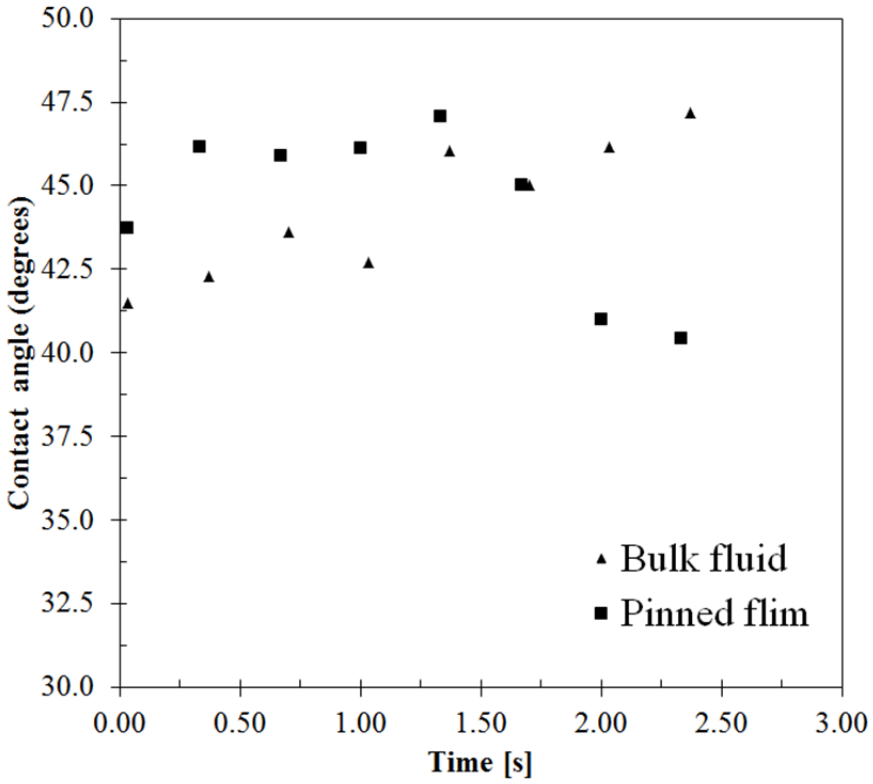

Figure 6.29: Experimentally measured contact angle of the pinned film and bulk fluid during droplet spreading

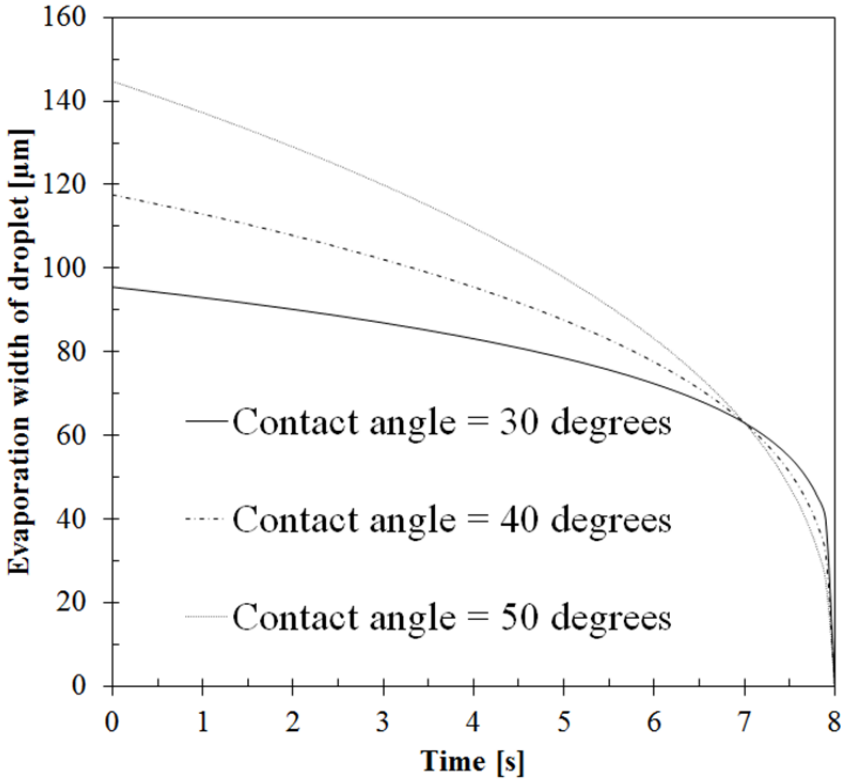

Figure 6.30: Effects of contact angle and width on evaporation of the bulk fluid in a rectangular microchannel

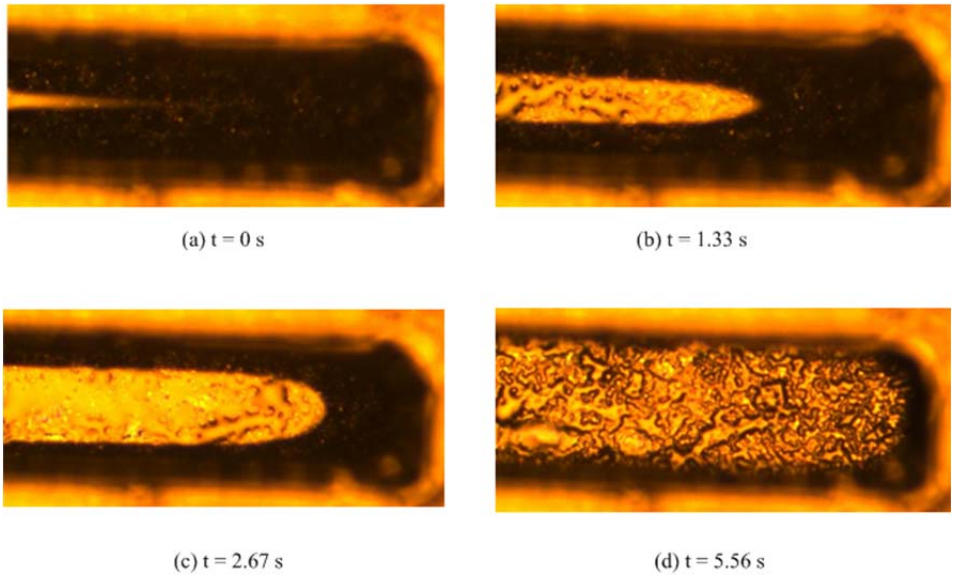

Figure 6.31: De-pinning of toluene droplet in Su-8 2075 between 0 and 5.56s

Although the channel width has a significant effect on the evaporation of toluene, the experimental observations show that it affects the structural layer of the channel. Solid particles are observed along the edges of the channel at the end of the evaporation cycle, which may suggest toluene etches the PZT substrate. The de-pinning process is interesting, because once the bulk fluid has evaporated, a split from the center is observed as shown in Figure 6.31.

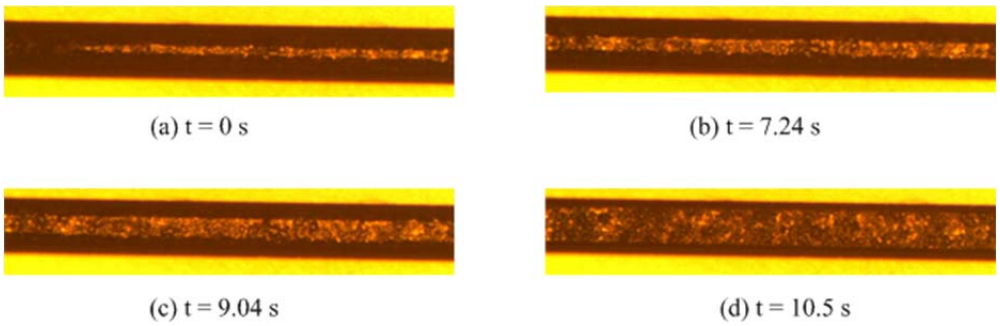

Figure 6.32: De-pinning of DI-water droplet in Su-8 2075 between 0 and 10.5s

The split is very different between toluene and water, when comparing the images in Figures 6.31 and 6.32. The difference in wetting properties of toluene and DI-water affects the separation process of the pinned film.

6.7 Experimental and analytical studies results of de-pinning in a closed microchannel

The de-pinning of the pinned toluene film commences immediately after the evaporation of the bulk fluid of toluene as observed in Figure 6.31(a). The de-pinning proceeds along the width and length simultaneously as observed in Figure 6.31(b). After about 2.67s, the rate of de-pinning is not significant across the length of the channel as observed in Figure 6.31 (c). The pinned film completely evaporates after about 5.56s as shown in Figure 6.31(d).

De-pinning of DI-water occurs over a longer period of time than that of toluene. The de-pinning process is only significant across the width of the channel, but occurs slightly across the length, as observed in Figure 6.32 (a). No further de-pinning across the length can be observed after about 7.24s as shown in Figure 6.32(b). The rate of de-pinning is significantly increased across the width after about 9.04s (Figure 6.32(c)). The pinned film completely evaporates after about 10.5s, as the PZT substrate is completely visible across the length and width of the microchannel as shown in Figure 6.32(d). The nature of the rough PZT substrate can be observed after the evaporation and de-pinning processes are complete as the images are compared for both processes.

A comparison between the de-pinning process for water and toluene is reported in Figure 6.33. A reasonable agreement can be observed between the experimental and analytical results. The analytical model accurately predicts the initial start and end of the de-pinning process, but a significant difference is observed with experimental results midway through the de-pinning process. This occurs due to the model not considering the heat transfer irreversibilities as a result of evaporation of the droplet. The experimental measurements were taken as soon as a clear path across the channel could be observed, signifying that a mixing of the two processes was not occurring simultaneously. The de-pinning rate of toluene is much faster than that of DI-water.

The de-pinning of toluene is multi- dimensional as it occurs in both the axial and transverse directions simultaneously. Only the de-pinning in the transverse direction (across the width) was considered in this study, as the rate is faster in this direction. The length of the channel is significantly higher than the width, hence the mass transfer rate is larger.

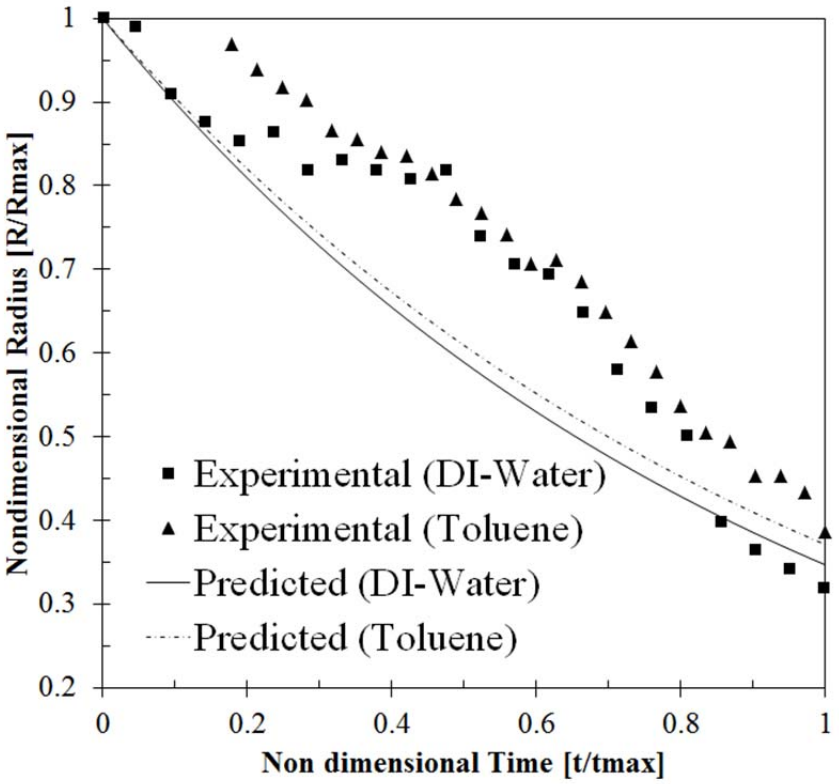

Figure 6.33: Comparison of experimental measurements and analytical predictions of de-pinning in a rectangular microchannel

A numerical two-dimensional solution will be required to account for the de-pinning in both directions. However, the limitation of the experimental setup did not allow observation of the entire channel length. The effect of change in channel width on the rate of de-pinning is reported in Figure 6.34. The effect of change in width of the channel has a significant effect on the de-pinning rate.

This can be attributed to an increase in surface area as it is directly proportional to the width of the channel. From equation (5.54), it can also be observed that the de-pinning radius is proportional to the diffusion coefficient. The analytical and experimental results are in good agreement, although the analytical model slightly overpredicts the start of the de-pinning process.

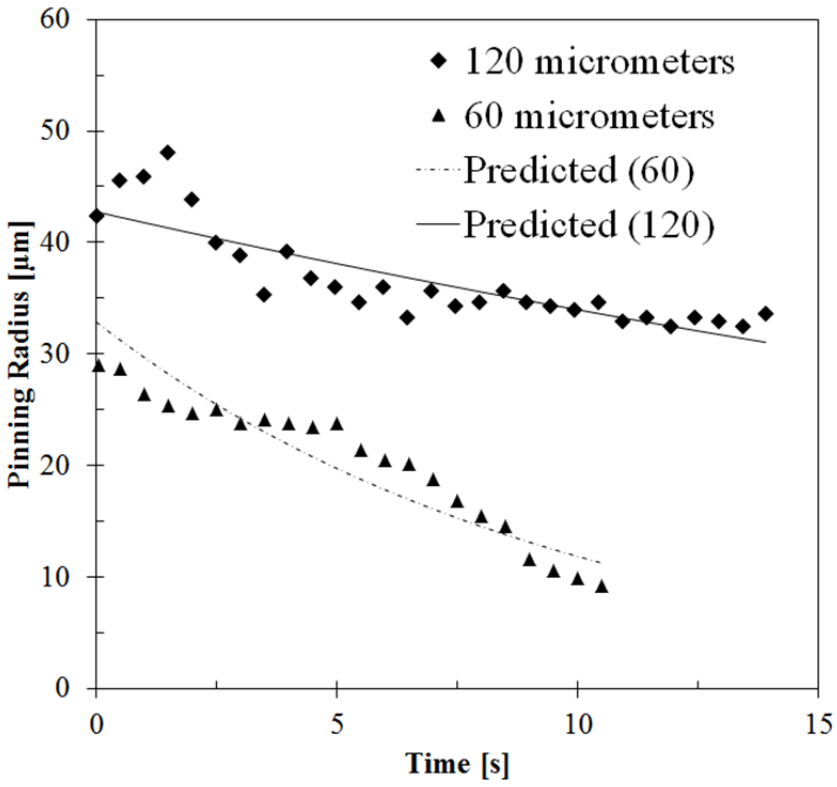

Figure 6.34: Comparison of experimental measurements and analytical predictions of de-pinning of toluene in a rectangular microchannel of different widths

A strong adhesion is observed between the pinned film and the PZT substrate. This occurs as a result of the roughness height of the substrate, as traces of the film are trapped within the grooves of the profile. Images from the experiment can be used to verify the latter assumption. The effect of height of the substrate on the de-pinning process was also investigated for toluene and reported in Figure 6.35. A non-dimensional analysis of analytical results shows a slight difference in the de-pinning rate of about 10% for the range of heights. The experimental results show a similar difference at some specific times, but the difference between analytical and experimental results is significant.

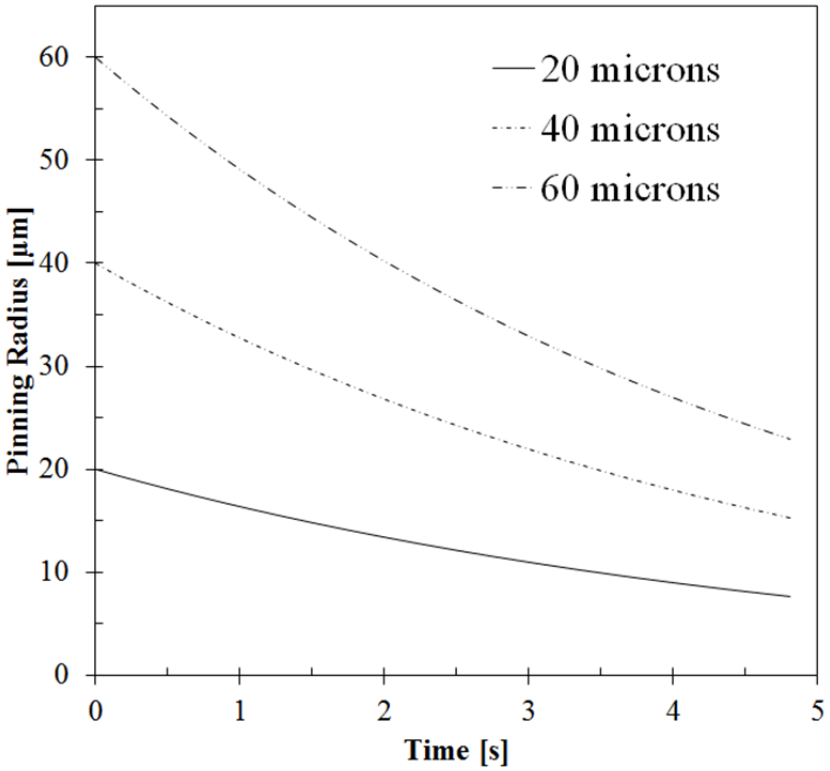

Figure 6.35: Effect of microchannel width on de-pinning of the bulk fluid in a rectangular microchannel

This can be attributed to neglecting de-pinning in the transverse direction in the current model and also neglecting the temperature gradient. Bonn [113] suggested that the inability to account for this phenomenon remains a challenge in accurately predicting the de-pinning process. The general trend of the analytical results is in good agreement with the experimental results. The change in contact line elastic force has an effect on the de-pinning rate [113]. This force increases with defects on the surface, confirming the relationship between surface roughness and the de-pinning rate. Further studies would be required to determine the actual effect of the overall volume change on the de-pinning process. The current experimental setup is limited to investigating only the change in width in relation to the de-pinning process.

Analytical studies were investigated to study the effect of channel width on the de-pinning process. Figure 6.35 indicates that larger channels have a higher de-pinning rate than smaller channels. This is expected as experimental results show similar trends.

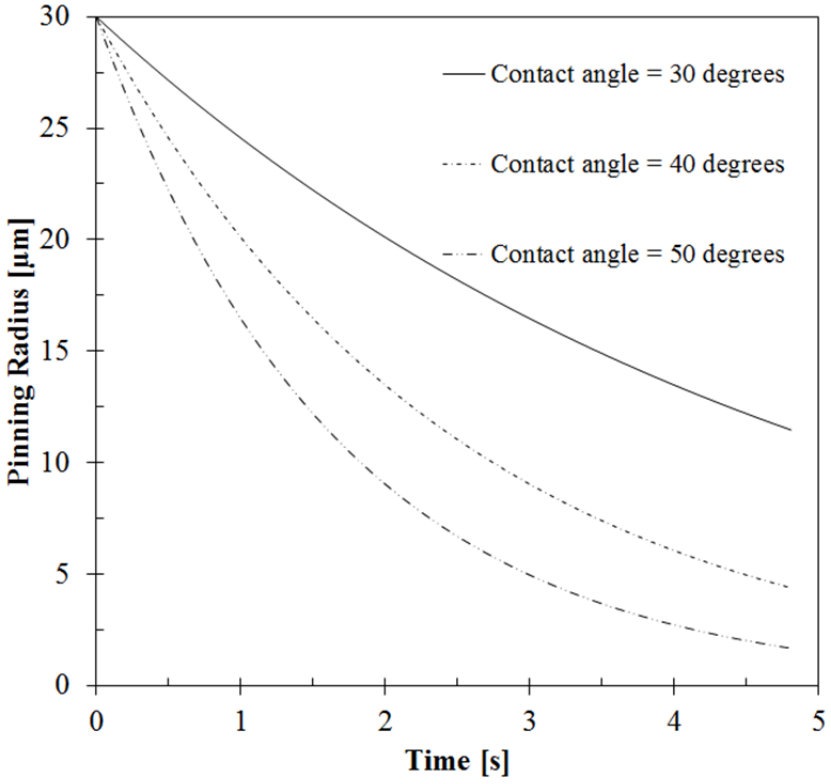

Figure 6.36: Effect of pinning contact angle on de-pinning of the bulk fluid in a rectangular microchannel

Although this model does not take into account the temperature gradient, which occurs during mass transfer from the surface, it predicts the experimental trends with reasonable accuracy. The effect of varying contact angles on the de-pinning radius was also reported in Figure 6.36. Varying the contact angle can be varied by changing the fluid, substrate or structural layer.

In this study, the choice of fluid was based on the ratio of the capillary to viscous forces. A high ratio results in an increase in the bulk velocity for the same amount of heat

input. A mineral oil which has a low evaporation rate will solve the problem of sealing the channel. However, a larger heat input is required for the same droplet volume, to yield a similar bulk velocity as DI-water or toluene in the MHE.

Although the sealing of the microchannel could not be achieved in other to measure the voltage and efficiency, an analytical investigation was performed to estimate the voltage and efficiency. New results have been presented to improve the existing knowledge of the dynamics of droplet motion in a closed microchannel. The following section will present conclusions from this thesis, future directions and recommendations for future research.

Chapter 7 : Conclusions and Recommendations

This section will highlight the major accomplishments form this study, propose ideas for future research, and elucidate recommendation for improving future work in this area.

7.1 Conclusions

A new model for predicting entropy production in an electrochemical cell was presented this thesis, particularly for diffusive irreversibilities of cuprous chloride electrolysis. The ohmic resistance has minimal effects on the electrolytic cell performance at high current densities. A significant effect of current density on overpotential was observed at low current densities (0 – 250mA/cm^2). From the entropy production results, it is preferable to operate the electrochemical cell at higher temperatures to reduce the irreversible losses. However, there are other limitations at high temperatures, due to the corrosive nature of hydrochloric acid. The current density has a significant effect on entropy production between 0 and 400mA/cm^2. The exchange current density was shown to have little effect on the cell overpotential, also the activation overpotential has the most significant effect on the cell performance. Although the ohmic resistance has little or no effect at high current densities, the effects become significant at lower current densities. Also, high charge transfer coefficients are undesirable, as they increase the entropy production in the system. At a high charge transfer coefficient, the energy required for cell operation nearly doubles, which makes the system less commercially viable. In summary, the new predictive formulation and results in this thesis have provided valuable new insight for the effective design and

improvement of electrolysis in the thermochemical copper-chlorine cycle of hydrogen production.

This thesis also examined the use of a PZT substrate for surface micromachining in microfluidics. Past studies have relied on silicon or glass substrates for surface micromachining of microfluidic devices. Although the latter substrates have the advantage of surface roughness in the order on nanometres, the ease of integrating PZT directly into the intended application provides a unique advantage. The results from this thesis have shown the excellent adhesive properties of PZT and Ti-W, by successfully patterning SU-8 directly into the heaters while maintaining good adhesion with the substrate.

To the best of the knowledge of the author, the patterning of the back of the PZT substrate with RIE by masking the front of the substrate with AZ3330 is an entirely new fabrication technique, which has not been investigated in past studies. Past experimental investigations by Glockner [112], did not achieve the production of a microheater for the MHE. This study has not only shown the possibility of fabricating the heaters, but presented experimental and analytical results to verify the use of a microheater to generate a heat flux beneath the microchannel.

This thesis has examined the fluid flow, heat transfer, and entropy production of droplet motion in a closed circular microchannel. New analytical models have been developed to predict the initial droplet acceleration, as well as thermocapillary pressure and friction forces within the droplet, and entropy generation. New experimental data was also presented for temperature and displacement of the droplet within the closed microchannel. The closed microchannel flow has a lower entropy generation number than

an open microchannel, and also water has a lower entropy generation than mineral oil droplets. The rapid response of the droplet to temperature changes indicates that thermocapillary pumping can serve a useful role in practical applications such as a thermal sensor, actuator or other micro-device application.

The effect of surface roughness on the kinematic viscosity was investigated in this study. The contribution of the apparent viscosity was considered in determining the net force on the droplet. The effect of the local Reynolds number within the boundary layer was considered in this study. The surface roughness was shown to have less impact on the droplet flow as the average bulk velocity of the fluid increased.

The transient nature of the droplet velocity has a significant effect on the voltage production in the MHE. New analytical results have been presented to determine the transient nature of the velocity of the droplet in a closed microchannel. Past studies [1, 2, 191] of a closed channel assumed that the droplet reaches a steady state. But experimental data in this thesis shows that the velocity reaches a maximum in a short time and subsequently reduces to zero as a result of the back pressure caused by the air in the closed end on the channel. The transient velocity was also related to the analytical voltage production in the MHE. A comparison was made between the steady state and transient approximation of the bulk velocity of the droplet with a time lag between both peaks. The peak transient velocity is about half of the peak of the steady state velocity. It was also shown that a similar effect is translated into a lower voltage when the transient flow is considered. The voltage was used to predict the efficiency of the MHE, while considering all of the layers deposited on the substrate.

The efficiency of the MHE was presented for different thicknesses of the piezoelectric membrane. The analytical study showed that the efficiency varied between 0.7 and 1.6% for the range of thicknesses considered. Although this efficiency appears quite low, the Carnot cycle efficiency for this system for an ambient temperature of 25^{o}C is only about 4.4% for the maximum temperature of the MHE. This indicates that if the system has a 700nm thick flexible membrane, it will be operating within 36% of the Carnot cycle efficiency. This is a relatively efficient heat engine under any standard of reference. Furthermore, since the objective is to harness low grade waste energy, the overall efficiency of the system will increase.

Also, the evaporation and pinning of a droplet in a closed rectangular microchannel has been investigated. The rate of evaporation for toluene and DI-water has been reported. New experimental and analytical results have been presented. The evaporation of toluene is twice as fast as water in a rectangular channel. Internal recirculation could be observed during the evaporation process. This could be confirmed by movement of particles during the evaporation process. The different modes of evaporation and de-pinning have been reported. Results indicate that toluene may erode the PZT substrate and should be avoided as a fluid in the microchannel despite its strong thermocapillary force. The evaporation and pinning processes are used to transfer solid particles in microfluidic applications [158]. These processes have found commercial applications in inkjet printing. Three-dimensional printing applications could benefit from the experimental and analytical results presented in this study. The results of this study could also be relevant in biomedical industries where small particles of solutes can be distributed through complex meshes.

7.2 Recommendations for future research

Controlling the droplet and sealing the top of the microchannel proved to be the most challenging aspect of this study. The design may be altered to successfully complete the MHE. Rather than injecting the droplet before sealing the channel, the channel can be sealed and capillary forces used to allow the droplet to flow into the microchannel. The mask used to fabricate the channel should be designed to pattern the open channels that span across the entire length of the substrate.

The entire substrate can then be immersed in a beaker of DI-water and the droplet may flow into the channel as a result of capillary motion. Subsequently the ends of the channel can be sealed with epoxy that requires no heat to set. The actual size and position of the droplet may still remain a challenge, but an automated system which relates the immersion depth to the size of the droplet could be built to overcome this problem. A micropump can be incorporated into the fabrication process, but this makes the design more complicated and new challenges may arise.

If the evaporation measurements were done in an environment where the humidity and temperature could be controlled, better agreement could be achieved between analytical and experimental results. The analytical model which is used to investigate the evaporation of toluene should be modified to consider the length of the droplet as a time dependent variable. This can be solved numerically and multiple microscopes and camera angles will be required to capture accurate experimental results. A microparticle analyzer may be required to study the nature of the particles during the evaporation process. It is not clear if light from the microscope could also have effect on the evaporation process. Although an infrared thermometer for measuring such small

temperature measurements is expensive, the temperature gradient will have an effect on the evaporation of the droplet.

The MHE is a possible accomplishment and would require highly sophisticated equipment to reach a commercial prototype. The design in this thesis is relatively cheap and the design conditions have been optimized and they are repeatable. This should encourage future researchers to pursue the challenge. Microfabrication is not only a difficult and complicated process, but patience and financial commitments are needed for success in this field of study.

References

[1] P.S. Glockner, G.F. Naterer, Surface tension and frictional resistance of thermocapillary pumping in a closed microchannel, Int. J. Heat Mass Transfer. 49 (2006) 4424-36.

[2] P.S. Glockner, G.F. Naterer, Thermocapillary control of microfluidic transport with a stationary cyclic heat source, J. Micromech. Microengineering. 15 (2005) 2216-29.

[3] S. Whalen, A. Thompson, D. Bahr, C. Richards, R. Richards, Design, fabrication and testing of the P3 micro heat engine, Sensor Actuat. A-Phys. 104 (2003) 290-8.

[4] PhysOrg, Nano motors, Retrieved April 15, 2007, from http://www.physorg. com/news10198. html.

[5] A. Bieberle-Hutter, D. Beckel, A. Infortuna, U.P. Muecke, J.L.M. Rupp, L.J. Gauckler, S. Rey-Mermet, P. Muralt, N.R. Bieri, N. Hotz, M.J. Stutz, D. Poulikakos, P. Heeb, P. Muller, A. Bernard, R. Gmur, T. Hocker, A micro-solid oxide fuel cell system as battery replacement, J. Power Sources. 177 (2008) 123-30.

[6] S.M. Lee, Kwan-Soo Lee, Young-Lae Kim, Silver alloying effect on the electrochemical behaviour of Si-Zr thin film anodes, J. Power Sources. 146 (2005) 464-8.

[7] A.M. Sastry, K.A. Cook, An algorithm for selection and design of hybrid power supplies for MEMS with a case study of a micro-gas chromatograph system, J. Power Sources. 140 (2005) 181-202.

[8] M.J. Ramsay, W.W. Clark, Piezoelectric energy harvesting for bio MEMS applications, Proc. SPIE Conf. 4332 (2001) 429-38.

[9] C.M. Spadaccini, X. Zhang, C.P. Cadou, N. Miki, I.A. Waitz, Preliminary development of a hydrocarbon-fuelled catalytic micro-combustor, Sensor Actuat. A-Phys. 103 (2003) 219-24.

[10] W.M. Yang, S.K. Chou, C. Shu, Z.W. Li, H. Xue, Development of microthermophotovoltaic system, Appl. Phys. Lett. 81 (2002) 5255-7.

[11] J. Larminie, A. Dicks, Knovel (Firm)., Fuel cell systems explained, 2nd Edition, John Wiley and Sons Ltd., West Sussex, UK, 2003.

[12] N. Nguyen, S.H. Chan, Micromachined polymer electrolyte membrane and direct methanol fuel cells - A review, J. Micromech. Microengineering. 16 (2006) 1-12.

[13] K.B. Min, S. Tanaka, M. Esashi, Fabrication of novel MEMS-based polymer electrolyte fuel cell architectures with catalytic electrodes supported on porous SiO2, J. Micromech. Microengineering. 16 (2006) 505-11.

[14] R. Hahn, S. Wagner, A. Schmitz, H. Reichl, Development of a planar micro fuel cell with thin film and micro patterning technologies, J. Power Sources. 131 (2004) 73-8.

[15] H. Cha, H. Choi, J. Nam, Y. Lee, S.M. Cho, E. Lee, J. Lee, C. Chung, Fabrication of all-polymer micro-DMFCs using UV-sensitive photoresist, Electrochim. Acta. 50 (2004) 795-99.

[16] S. Aravamudhan, S. Bhansali, A.R.A. Rahman, Porous silicon based orientation independent, self-priming micro direct ethanol fuel cell, Sensor Actuat. A-Phys. 123-124 (2005) 497-504.

[17] C.Y. Lee, G.W. Wu, C.L. Hsieh, In situ diagnosis of micrometallic proton exchange membrane fuel cells using microsensors, J. Power Sources. 172 (2007) 363-7.

[18] S.J. Lee, Yu-Ming Lee, C.Y. Lee, J.J. Lai, F.H. Kuan, C.W. Chuang, The performance of miniature metallic PEM fuel cells, J. Power Sources. 171 (2007) 148-54.

[19] B.E. Buergler, M. Ochsner, S. Vuillemin, L.J. Gauckler, From macro- to micro-single chamber solid oxide fuel cells, J. Power Sources. 171 (2007) 310-20.

[20] Y. Zhang, J. Lu, S. Shimano, H. Zhou, R. Maeda, Development of MEMS-based direct methanol fuel cell with high power density using nanoimprint technology, Electrochem. Commun. 9 (2007) 1365-8.

[21] F. Takei, N.F. Cooray, K. Yoshida, H. Yoshida, K. Ebisu, S. Suzuki, N. Sawatari, Development of prototype micro fuel cells for mobile electronics, Fujitsu Sci. Tech. J. 41 (2005) 191-200.

[22] G.Q. Lu, C.Y. Wang, T.J. Yen, X. Zhang, Development and characterization of a silicon-based micro direct methanol fuel cell, Electrochim. Acta. 49 (2004) 821-8.

[23] S. Motokawa, M. Mohamedi, T. Momma, S. Shoji, T. Osaka, MEMS-based design and fabrication of a new concept micro direct methanol fuel cell (DMFC), Electrochem. Commun. 6 (2004) 562-5.

[24] Y. Yamazaki, Application of MEMS technology to micro fuel cells, Electrochim. Acta. 50 (2004) 663-6.

[25] Y. Tang, K. Stanley, J. Wu, D. Ghosh, J. Zhang, Design consideration of micro thin film solid-oxide fuel cells, J. Micromech. Microengineering. 15 (2005) 185-92.

[26] V.T. Srikar, K.T. Turner, T.Y.A. Ie, S.M. Spearing, Structural design considerations for micromachined solid-oxide fuel cells, J. Power Sources. 125 (2004) 62-9.

[27] R.R. King, D.C. Law, K.M. Edmondson, C.M. Fetzer, G.S. Kinsey, H. Yoon, R.A. Sherif, N.H. Karam, 40% efficient metamorphic GaInP/GaInAs/Ge multijunction solar cells, Appl. Phys. Lett. 90 (2007) 183516-1.

[28] J.B. Lee, Z. Chen, M.G. Allen, A. Rohatgi, R. Arya, A miniaturized high-voltage solar cell array as an electrostatic MEMS power supply, J. Microelectromech. Syst. 4 (1995) 102-8.

[29] S. Bermejo, P. Ortega, J.J. Jimenez, L. Castaner, Response of c-Si PV arrays under monochromatic light for MEMS power supply, J. Micromech. Microengineering. 15 (2005) 1446-53.

[30] A. Kribus, Thermal integral micro-generation systems for solar and conventional use, J. Sol. Energ-T ASME. 124 (2002) 189-97.

[31] R.W. Miles, K.M. Hynes, I. Forbes, Photovoltaic solar cells: An overview of state-of-the-art cell development and environmental issues, Prog. Cryst. Growth Charact. Mater. 51 (2005) 1-42.

[32] M. Bashahu, P. Nkundabakura, Review and tests of methods for the determination of the solar cell junction ideality factors, Sol. Energy. 81 (2007) 856-63.

[33] C. Baur, A.W. Bett, F. Dimroth, G. Siefer, M. Meusel, W. Bensch, W. Kostler, G. Strobl, Triple-junction III-V based concentrator solar cells: perspectives and challenges, J. Sol. Energ-T. ASME. 129 (2007) 258-65.

[34] T.L. Benanti, D. Venkataraman, Organic solar cells: an overview focusing on active layer morphology, Photosynth. Res. 87 (2006) 73-81.

[35] M. Bosi, C. Pelosi, The potential of lll-V semiconductors as terrestrial photovoltaic devices, Prog. Photovolt. Res. Appl. 15 (2007) 51-68.

[36] R. Brendel, Thin-film crystalline silicon mini-modules using porous Si for layer transfer, Sol. Energy. 77 (2004) 969-82.

[37] E. Bundgaard, F.C. Krebs, Low band gap polymers for organic photovoltaics, Sol. Energ. Mat. Sol. C. 91 (2007) 954-85.

[38] K.L. Chopra, P.D. Paulson, V. Dutta, Thin-film solar cells: An overview, Prog. Photovolt. Res. Appl. 12 (2004) 69-92.

[39] N.G. Dhere, S.R. Ghongadi, M.B. Pandit, A.H. Jahagirdar, D. Scheiman, CIGS2 thin-film solar cells on flexible foils for space power, Prog. Photovolt. Res. Appl. 10 (2002) 407-16.

[40] S. Erten, E. Eren, S. Icli, Dye sensitized solar cell based on 1,8-naphthalene benzimidazole comprising carboxyl group, Eur. Phys. J-Appl. Phys. 38 (2007) 227-30.

[41] K. Feldrapp, R. Horbelt, R. Auer, R. Brendel, Thin-film (25.5 m) solar cells from layer transfer using porous silicon with 32.7 mA/cm2 short-circuit current density, Prog. Photovolt. Res. Appl. 11 (2003) 105-12.

[42] L. Ferraioli, P. Maddalena, A. Parretta, A. Wang, J. Zhao, Current-voltage characteristics of high-efficiency silicon solar cells from photoluminescence, Appl. Phys. Lett. 85 (2004) 4222-4.

[43] A. J Frank, N. Kopidakis, J. Lagemaat, Electrons in nanostructured TiO2 solar cells: transport, recombination and photovoltaic properties, Coord. Chem. Rev. 248 (2004) 1165-79.

[44] A.M. Hermann, Polycrystalline thin-film solar cells-a review, Sol. Energ. Mat. Sol. C. 55 (1998) 75-81.

[45] R. Koeppe, O. Bossart, G. Calzaferri, N.S. Sariciftci, Advanced photon-harvesting concepts for low-energy gap organic solar cells, Sol. Energ. Mat. Sol. C. 91 (2007) 986-95.

[46] J.M. Kroon, N.J. Bakker, H.J.P. Smit, P. Liska, K.R. Thampi, P. Wang, S.M. Zakeeruddin, M. Gratzel, A. Hinsch, S. Hore, U. Wurfel, R. Sastrawan, J.R. Durrant, E. Palomares, H. Pettersson, T. Gruszecki, J. Walter, K. Skupien, G.E. Tulloch, Nanocrystalline dye-sensitized solar cells having maximum performance, Prog. Photovolt. Res. Appl. 15 (2007) 1-18.

[47] H. Li, R.L. Stolk, D.W. van, M.Y.S. Rusche, J.K. Rath, R.E.I. Schropp, Thin film micro- and polycrystalline silicon nip cells on stainless steel made by hot-wire chemical vapour deposition, Thin Solid Films. 501 (2006) 276-9.

[48] L.L. Gui, G.H. Lu, X.N. Yang, L. Zhou En, Progress in polymer solar cell, Chinese Sci. Bull. 52 (2007) 145-58.

[49] Q. Yao, Z.H. Lu, Energy analysis of silicon solar cell modules based on an optical model for arbitrary layers, Sol. Energy. 81 (2007) 636-47.

[50] O. Lundberg, M. Edoff, L. Stolt, The effect of Ga-grading in CIGS thin film solar cells, Thin Solid Films. 480-481 (2005) 520-5.

[51] T. Sakakibara, H. Izu, T. Shibata, S. Takahashi, H. Tarui, H. Hirano, K. Shibata, S. Kiyama, N. Kawahara, Multi-source power supply system using micro-photovoltaic devices combined with microwave antenna, New Mater. Res. (2001) 192-5.

[52] Amereco Solar, Southwest Photovoltaic (PV) Systems, Retrieved September 10, 2007, from http://www.southwestpv.com/.

[53] Phyorg, First solar powered nanomotor, Retrieved September 10, 2007, from http://www.physorg.com/news10198.html.

[55] Alter systems, Go green for life, Retrieved September 12, 2007, from http://www.altersystems.com/catalog/index.

[56] D. Golodnitsky, V. Yufit, M. Nathan, I. Shechtman, T. Ripenbein, E. Strauss, S. Menkin, E. Peled, Advanced materials for the 3D microbattery, J. Power Sources. 153 (2006) 281-7.

[57] S.R. Brown, S.M. Kauzlarich, F. Gascoin, G.J. Snyder, Yb14MnSb11: New high efficiency thermoelectric material for power generation, Chem. Mater. 18 (2006) 1873-1877.

[58] M. Chen, S.S. Lu, B. Liao, On the figure of merit of thermoelectric generators, J. Energ. Res-ASME. 127 (2005) 37-41.

[59] M. Strasser, R. Aigner, C. Lauterbach, T.F. Sturm, M. Franosch, G. Wachutka, Micromachined CMOS thermoelectric generators as on-chip power supply, Sensor Actuat. A-Phys. 114 (2004) 362-70.

[60] R. Venkatasubramanian, E. Siivola, T. Colpitts, B. O'Quinn, Thin-film thermoelectric devices with high room-temperature figures of merit, Nature. 413 (2001) 597-602.

[61] W. Wang, F. Jia, Q. Huang, J. Zhang, A new type of low power thermoelectric micro-generator fabricated by nanowire array thermoelectric material, Microelectron. Eng. 77 (2005) 223-9.

[62] J. Weber, K. Potje-Kamloth, F. Haase, P. Detemple, F. Volklein, T. Doll, Coin-size coiled-up polymer foil thermoelectric power generator for wearable electronics, Sensor Actuat. A-Phys. 132 (2006) 325-30.

[63] X.C. Xuan, Optimum design of a thermoelectric device, Semicond. Sci. Tech. 17 (2002) 114-9.

[64] K. Yoshida, S. Tanaka, S. Tomonari, D. Satoh, M. Esashi, High-energy density miniature thermoelectric generator using catalytic combustion, J. Microelectromech. Syst. 15 (2006) 195-203.

[65] Q.J. Zhang, X.F. Tang, P.C. Zhai, M. Niino, C. Endo, Recent development in nano and graded thermoelectric materials, Mater. Sci. Forum. 492-493 (2005) 135-40.

[66] J.R. Lim, J.F. Whitacre, J. Fleurial, C. Huang, M.A. Ryan, N.V. Myung, Fabrication method for thermoelectric nanodevices, Adv. Mater. 17 (2005) 1488-92.

[67] R. Funahashi, M. Mikami, T. Mihara, S. Urata, N. Ando, A portable thermoelectric-power-generating module composed of oxide devices, J. Appl. Phys. 99 (2006) 66117-120.

[68] W.V. Slaton, J.C.H. Zeegers, Thermoelectric power generation in a thermoacoustic refrigerator, Appl. Acoust. 67 (2006) 450-60.

[69] S.P. Beeby, M.J. Tudor, N.M. White, Energy harvesting vibration sources for microsystems applications, Meas. Sci. Technol. 17 (2006) 175-95.

[70] C.B. Williams, R.B. Yates, Analysis of a micro-electric generator for microsystems, IEE Proc-G. 1 (1995) 369-72.

[71] S.P. Beeby, R.N. Torah, M.J. Tudor, P. Glynne-Jones, T. O'Donnell, C.R. Saha, S. Roy, A micro electromagnetic generator for vibration energy harvesting, J. Micromech. Microengineering. 17 (2007) 1257-65.

[72] C. Shearwood, R.B. Yates, Development of an electromagnetic micro-generator, Electron. Lett. 33 (1997) 1883-4.

[73] C.B. Williams, C. Shearwood, M.A. Harradine, P.H. Mellor, T.S. Birch, R.B. Yates, Development of an electromagnetic micro-generator, IEE Proc-G. 148 (2001) 337-42.

[74] M. El-Hami, P. Glynne-Jones, N.M. White, M. Hill, S. Beeby, E. James, A.D. Brown, J.N. Ross, Design and fabrication of a new vibration-based electromechanical power generator, Sensor Actuat. A-Phys. 92 (2001) 335-42.

[75] M. Mizuno, D.G. Chetwynd, Investigation of a resonance microgenerator, J. Micromech. Microengineering. 13 (2003) 209-16.

[76] P. Glynne-Jones, M.J. Tudor, S.P. Beeby, N.M. White, An electromagnetic, vibration-powered generator for intelligent sensor systems, Sensor Actuat. A-Phys. 110 (2004) 344-9.

[77] N.N.H. Ching, H.Y. Wong, W.J. Li, P.H.W. Leong, Z. Wen, A laser-micromachined multi-modal resonating power transducer for wireless sensing systems, Sensor Actuat. A-Phys. 97-98 (2002) 685-90.

[78] T. von Buren, G. Troster, Design and optimization of a linear vibration-driven electromagnetic micro-power generator, Sensor Actuat. A-Phys. 135 (2007) 765-75.

[79] C.T. Pan, T.T. Wu, Development of a rotary electromagnetic microgenerator, J. Micromech. Microengineering. 17 (2007) 120-8.

[80] C. Serre, A. Perez-Rodriguez, N. Fondevilla, J.R. Morante, J. Montserrat, J. Esteve, Vibrational energy scavenging with Si technology electromagnetic inertial microgenerators, Microsyst. Technol. 13 (2007) 1655-1661.

[81] S. Scherrer, D.G. Plumlee, A.J. Moll, Energy scavenging device in LTCC materials, Microsyst. Technol. 13 (2005) 77-8.

[82] A. Badel, A. Benayad, E. Lefeuvre, L. Lebrun, C. Richard, D. Guyomar, Single crystals and nonlinear process for outstanding vibration-powered electrical generators, IEEE Trans. Ultrason. Ferroelectr. Freq. Control. 53 (2006) 673-83.

[83] M. Miyazaki, H. Tanaka, G. Ono, T. Nagano, N. Ohkubo, T. Kawahara, Electric-energy generation through variable-capacitive resonator for power-free LSI, IEICE Trans. Electron. 87 (2004) 549-55.

[84] S. Roundy, E.S. Leland, J. Baker, E. Carleton, E. Reilly, E. Lai, B. Otis, J.M. Rabaey, P.K. Wright, V. Sundararajan, Improving power output for vibration-based energy scavengers, Pervasive Comput. 4 (2005) 28-36.

[85] S. Roundy, On the effectiveness of vibration-based energy harvesting, J. Intell. Mater. Syst. Struct. 16 (2005) 809-823.

[86] S. Roundy, P.K. Wright, J. Rabaey, A study of low level vibrations as a power source for wireless sensor nodes, Comput. Commun. 26 (2003) 1131-44.

[87] S.J. Roundy, Energy scavenging for wireless sensor nodes with a focus on vibration to electricity conversion, PhD thesis, University of Buckley California. 2003.

[88] P.D. Mitcheson, P. Miao, B.H. Stark, E.M. Yeatman, A.S. Holmes, T.C. Green, MEMS electrostatic micropower generator for low frequency operation, Sensor Actuat. A-Phys. 115 (2004) 523-9.

[89] R. Tashiro, N. Kabei, K. Katayama, E. Tsuboi, K. Tsuchiya, Development of an electrostatic generator for a cardiac pacemaker that harnesses the ventricular wall motion, J. Artif. Organs. 5 (2002) 239-45.

[90] S. Meninger, J. Mur-Miranda, R. Amirtharajah, A. Chandrakasan, J. Lang, Vibration-to-electric energy conversion, IEEE Power Electron. (Digest of Technical Papers). (1999) 48-53.

[91] W. Ma, R. Zhu, L. Rufer, Y. Zohar, M. Wong, An integrated floating-electrode electric microgenerator, J. Microelectromech. Syst. 16 (2007) 29-37.

[92] P. Miao, A.S. Holmes, E.M. Yeatman, T.C. Green, P.D. Mitcheson, Micro-machined variable capacitors for power generation, Proc. Electrostatics Conference Inst. of Phys, Edinburg, UK. 2 (2003) pp. 53-8.

[93] R. Tashiro, N. Kabei, K. Katayama, Y. Ishizuka, F. Tsuboi, K. Tsuchiya, Development of an electrostatic generator that harnesses the motion of a living body: (use of a resonant phenomenon), JSME Int. J. Series C. 43 (2000) 916-22.

[94] B.H. Stark, P.D. Mitcheson, P. Miao, T.C. Green, E.M. Yeatman, A.S. Holmes, Converter circuit design, semiconductor device selection and analysis of parasitics for micropower electrostatic Generators, IEEE Trans. Power Electron. 21 (2006) 27-37.

[95] B.H. Stark, T.C. Green, Comparison of SOI power device structures in power converters for high-voltage, low-charge electrostatic microgenerators, IEEE Trans. Electron. Devices. 52 (2005) 1640-8.

[96] N.M. White, P. Glynne-Jones, S.P. Beeby, A novel thick-film piezoelectric micro-generator, Smart Mater. Struct. 10 (2001) 850-2.

[97] Y.B. Jeon, R. Sood, J. Jeong, S. Kim, MEMS power generator with transverse mode thin film PZT, Sensor Actuat. A-Phys. 122 (2005) 16-22.

[98] V.H. Schmidt, Piezoelectric energy conversion in windmills, Ultrason. 2 (1992) 897-904.

[99] N.S. Shenck, J.A. Paradiso, Energy scavenging with shoe-mounted piezoelectrics, IEEE Micro. 21 (2001) 30-42.

[100] S.R. Platt, S. Farritor, H. Haider, On Low-frequency electric power generation with PZT ceramics, IEEE/ASME Trans. Mechatronics. 10 (2005) 240-52.

[101] H.W. Kim, A. Batra, S. Priya, K. Uchino, D. Markley, R.E. Newnham, H.F. Hofmann, Energy harvesting using a piezoelectric "cymbal" transducer in dynamic environment, JPN J. Appl. Phys. 1. 43 (2004) 6178-83.

[102] S. Priya, C. Chen, D. Fye, J. Zahnd, Piezoelectric windmill: a novel solution to remote sensing, JPN J. Appl. Phys. 2. 44 (2005) 104-7.

[103] K. Ren, Y. Liu, X. Geng, H.F. Hofmann, Q.M. Zhang, Single crystal PMN-PT/epoxy 1-3 composite for energy-harversting application, IEEE Trans. Ultrason. Ferroelectr. Freq. Control. 53 (2006) 631-37.

[104] F. Hua-Bin, L. Jing-Quan, X. Zheng-Yi, D. Lu, C. Di, C. Bing-Chu, L. Yue, A MEMS-based piezoelectric power Generator for low frequency vibration energy harvesting, Chinese Phys. Let. 23 (2006) 732-4.

[105] S. Wu, J. Mai, Y.C. Tai, C.M. Ho, Micro heat exchanger by using MEMS impinging jets, Proc. IEEE Micr. Elect., Orlado Fl. (1999) pp.171-6.

[106] K. Vafai, L. Zhu, Analysis of two-layered micro-channel heat sink concept in electronic cooling, Int. J. Heat Mass Transfer. 42 (1999) 2287-97.

[107] A.J. Tudos, G.A.J. Besseling, R.B.M. Schasfoort, Trends in miniaturized total analysis systems for point-of-care testing in clinical chemistry, Lab Chip. 1 (2001) 83-95.

[108] G.F. Naterer, P.S. Glockner, D. Thiele, S. Chomokovski, G. Venn, G. Richardson, Surface micro-grooves for near-wall exergy and flow control: application to aircraft intake de-icing, J. Micromech. Microengineering. 15 (2005) 501-13.

[109] J. Yang, F. Lu, L.W. Kostiuk, D.Y. Kwok, Electrokinetic microchannel battery by means of electrokinetic and microfluidic phenomena, J. Micromech. Microengineering. 13 (2003) 963-70.

[110] B.C. Regan, S. Aloni, K. Jensen, A. Zettl, Surface-tension-driven nanoelectromechanical relaxation oscillator, Appl. Phys. Lett. 86 (2005) 123119-1.

[111] G.F. Naterer, P.S. Glockner, Surface tension and frictional resistance of thermocapillary pumping in a closed microchannel, Int. J. Heat Mass Transfer. 49 (2006) 4424-36.

[112] P.S. Glockner, Numerical and Experimental Investigation of Thermocapillary Pumping in Closed-End Microchannels for Micro Heat Engines, PhD thesis University of Manitoba, Winepeg, 2006.

[113] D. Bonn, J. Eggers, J. Indekeu, J. Meunier, E. Rolley, Wetting and spreading, Rev. Mod. Phys. 81 (2009) 739-805.

[114] C.B. Sobhan, S.V. Garimella, A comparative analysis of studies on heat transfer and fluid flow in microchannels, Microscale Therm. Eng. 5 (2001) 293-311.

[115] R. Baviere, M. Favre-Marinet, S. Le Person, Bias effects on heat transfer measurements in microchannel flows, Int. J. Heat Mass Transfer. 49 (2006) 3325-37.

[116] S.V. Garimella, P.S. Lee, Thermally developing flow and heat transfer in rectangular microchannels of different aspect ratios, Int. J. Heat Mass Transfer. 49 (2006) 3060-7.

[117] R. Muwanga, I. Hassan, M. Ghorab, Numerical investigation of a radial microchannel heat exchanger with varying cross-sectional channels, J. Thermophys. Heat Transfer. 22 (2008) 321-32.

[118] T.C. Hui, X. Wang, Y.T. Hwee, A numerical study of the Hampson-type miniature Joule-Thomson cryocooler, Int. J. Heat Mass Transfer. 49 (2006) 582-93.

[119] H. Chen, B. Zhang, J. Ma, Theoretical and numerical analysis of convective heat transfer in the rotating helical pipes, Int. J. Heat Mass Transfer. 46 (2003) 4899-909.

[120] H. Honda, Y.S. Wang, Theoretical study of evaporation heat transfer in horizontal microfin tubes: stratified flow model, Int. J. Heat Mass Transfer. 47 (2004) 3971-83.

[121] S. Luciani, C. Le Niliot, Local heat transfer estimation in microchannels during convective boiling under microgravity conditions: 3D inverse heat conduction problem using BEM techniques, J. Phys. 135 (2008) 012067- 75.

[122] K.C. Toh, X.Y. Chen, J.C. Chai, Numerical computation of fluid flow and heat transfer in microchannels, Int. J. Heat Mass Transfer. 45 (2002) 5133-41.

[123] W.A. Khan, M.M. Yovanovich, Analytical modeling of fluid flow and heat transfer in micro/nano-channel heat sinks, Proc. ASME InterPACK, Vancouver, BC. (2007) pp.109-20.

[124] G. Rosengarten, J. Cooper-White, G. Metcalfe, Experimental and analytical study of the effect of contact angle on liquid convective heat transfer in microchannels, Int. J. Heat Mass Transfer. 49 (2006) 4161-70.

[125] G. Croce, P. D'agaro, C. Nonino, Three-dimensional roughness effect on microchannel heat transfer and pressure drop, Int. J. Heat Mass Transfer. 50 (2007) 5249-59.

[126] W. Qu, M. Mala, D. Li, Heat transfer for water flow in trapezoidal silicon microchannels, Int. J. Heat Mass Transfer. 43 (2000) 3925-36.

[127] V. Zimparov, Extended performance evaluation criteria for enhanced heat transfer surfaces: heat transfer through ducts with constant heat flux, Int. J. Heat Mass Transfer. 44 (2001) 169-80.

[128] A. Bejan, Entropy generation minimization: The new thermodynamics of finite-size devices and finite-time processes, J. Appl. Phys. 79 (1996) 1191-218.

[129] G.F. Naterer, O.B. Adeyinka, Microfluidic exergy loss in a non-polarized thermomagnetic field, Int. J. Heat Mass Transfer. 48 (2005) 3945-56.

[130] A.K. Hussain, T.A. Hussain, H.A.K. Shahad, A thermodynamic analysis of non-equilibrium heat conduction in a semi-infinite medium subjected to a step change in temperature, Energ. Convers. Manage. 44 (2003) 1373-86.

[131] G.F. Naterer, J.A. Camberos, Entropy-Based Design and Analysis of Fluids Engineering Systems, CRC Press, Boca Raton, FL, 2008.

[132] I. Dagtekin, H.F. Oztop, A.Z. Sahin, An analysis of entropy generation through a circular duct with different shaped longitudinal fins for laminar flow, Int. J. Heat Mass Transfer. 48 (2005) 171-81.

[133] E.B. Ratts, A.G. Raut, Entropy generation minimization of fully developed internal flow with constant heat flux, J. Heat Trans-T. ASME. 126 (2004) 656-9.

[134] T.A. Jankowski, Minimizing entropy generation in internal flows by adjusting the shape of the cross-section, Int. J. Heat Mass Transfer. 52 (2009) 3439-45.

[135] D.K. Ryland, H. Li, R.R. Sadhankar, Electrolytic hydrogen generation using CANDU nuclear reactors, Int. J. Energy Res. 31 (2007) 1142-55.

[136] G.F. Naterer, K. Gabriel, Z.L. Wang, V.N. Daggupati, R. Gravelsins, Thermochemical hydrogen production with a copper-chlorine cycle. I: oxygen release from copper oxychloride decomposition, Int. J. Hydrogen Energy. 33 (2008) 5439-50.

[137] G.F. Naterer, V.N. Daggupati, G. Marin, K.S. Gabriel, Z.L. Wang, Thermochemical hydrogen production with a copper-chlorine cycle, II: flashing and drying of aqueous cupric chloride, Int. J. Hydrogen Energy. 33 (2008) 5451-9.

[138] S. Manish, R. Banerjee, Comparison of biohydrogen production processes, Int. J. Hydrogen Energy. 33 (2008) 279-86.

[139] D.B. Levin, L. Pitt, M. Love, Biohydrogen production: prospects and limitations to practical application, Int. J. Hydrogen Energy. 29 (2004) 173-85.

[140] S.H. Jensen, P.H. Larsen, M. Mogensen, Hydrogen and synthetic fuel production from renewable energy sources, Int. J. Hydrogen Energy. 32 (2007) 3253-7.

[141] V. Lipovestsky, Production of hydrogen, obtaining electric and thermal energy by water dissociation method, Int. J. Hydrogen Energy. 29 (2004) 1555-83.

[142] W. Kreuter, H. Hofmann, Electrolysis: the important energy transformer in a world of sustainable energy, Int. J. Hydrogen Energy. 23 (1998) 661-6.

[143] T.Z. Yan, Tien-Chien Jen, Two-phase flow modeling of liquid-feed direct methanol fuel cell, Int. J. Heat Mass Transfer. 51 (2008) 1192-204.

[144] J.J. Hwang, P.Y. Chen, Heat/mass transfer in porous electrodes of fuel cells, Int. J. Heat Mass Transfer. 49 (2006) 2315-27.

[145] G.F. Naterer, C.D. Tokarz, J. Avsec, Fuel cell entropy production with ohmic heating and diffusive polarization, Int. J. Heat Mass Transfer. 49 (2006) 2673-83.

[146] G.F. Naterer, Establishing heat-entropy analogies for interface tracking in phase change heat transfer with fluid flow, Int. J. Heat Mass Transfer. 44 (2001) 2903-16.

[147] G.F. Naterer, Applying heat-entropy analogies with experimental study of interface tracking in phase change heat transfer, Int. J. Heat Mass Transfer. 44 (2001) 2917-32.

[148] J. Nikuradse, National Advisory Committee for Aeronautics: Laws of Flow in Rough Pipes, National Advisory Committee for Aeronautics, Washington, US, 1950.

[149] S.G. Kandlikar, S. Joshi, S. Tian, Effect of channel roughness on heat transfer and fluid flow characteristics at low Reynolds numbers in small diameter tubes, 35th National Heat Transfer Conference, Anaheim, Ca. (2001) pp. 1609-18.

[150] C. Zhang, Y. Chen, M. Shi, Effects of roughness elements on laminar flow and heat transfer in microchannels, Chem. Eng. Process. 49 (2010) 1188-92.

[151] M. Mala, D. Li, Flow characteristics of water in microtubes, Int. J. Heat Fluid Flow. 20 (1999) 142-148.

[152] A. Kasyap, J. Lim, D. Johnson, S. Horowitz, T. Nishida, K. Ngo, M. Sheplak, L. Cattafesta, Energy Reclamation from a Vibrating Piezoelectric Composite Beam, 9th Annual Conference on Sound and Vibration Orlando, Fl. (2002) pp. 36-43.

[153] S. Horowitz, A. Kasyap, F. Liu, D. Johnson, T. Nishida, K. Ngo, M. Sheplak, L. Cattafesta, Technology development for self-powered sensors, AIAA 1st Flow Control Conference St. Louis, Mo. (2002) pp. 2002–702 .

[154] K.A. Cook-Chennault, N. Thambi, M.A. Bitetto, E. Hameyie, Piezoelectric Energy Harvesting: A Green and Clean Alternative for Sustained Power Production. **B**. Sci. Technol. Soc. 28 (2008) 496-509.

[155] L. Mateu, F. Moll, Optimum piezoelectric bending beam structures for energy harvesting using shoe inserts, J. Intel. Mat. Syst. Str. 16 (2005) 835-45.

[156] H.S. Yoon, G. Washington, A. Danak, Modeling, optimization, and design of efficient initially curved piezoceramic unimorphs for energy harvesting applications, J. Intel. Mat. Syst. Str.16 (2005) 877-88.

[157] K. Ragil, D. Bonn, D. Broseta, J. Meunier, Wetting of alkanes on water from a Cahn-type theory, J. Chem. Phys. 105 (1996) 5160-7.

[158] R.D. Deegan, O. Bakajin, T.F. Dupont, G. Huber, S.R. Nagel, T.A. Witten, Contact line deposits in an evaporating drop, Phys. Rev. E. 62 (2000) 756-65.

[159] S.M. Rowan, M.I. Newton, G. McHale, Evaporation of microdroplets and the wetting of solid surfaces, J. Phys. Chem. 99 (1995) 13268-71.

[160] G. McHale, S.M. Rowan, M.I. Newton, M.K. Banerjee, Evaporation and the wetting of a low-energy solid surface, J. Phys. Chem. B. 102 (1998) 1964-7.

[161] C. Poulard, G. Guéna, A.M. Cazabat, A. Boudaoud, M.B. Amar, Rescaling the dynamics of evaporating drops, Langmuir. 21 (2005) 8226-33.

[162] R.D. Deegan, Pattern formation in drying drops, Phys. Rev. E. 61 (2000) 475-85.

[163] R.D. Deegan, O. Bakajin, T.F. Dupont, Capillary flow as the cause of ring stains from dried liquid drops, Nature. 389 (1997) 827-29.

[164] J.R. Welty, C.E. Wicks, G. Rorrer, R.E. Wilson, Fundamentals of Momentum, Heat, and Mass Transfer, Wiley-India, 2009.

[165] S.H. Davis, Thermocapillary instabilities, Annu. Rev. Fluid Mech**.** 19 (1987) 403-35.

[166] E. Sultan, A. Boudaoud, M.B. Amar, Diffusion-limited evaporation of thin polar liquid films, J. Eng. Math. 50 (2004) 209-22.

[167] C. Bourges, M.E.R. Shanahan, Influence of evaporation on the contact angle of water drops, C. R. Acad. Sci. Ii-B. 316 (1993) 311-16.

[168] D. Bonn, J. Meunier, Comment on evaporation preempts complete wetting, Euro. Phys. Lett. 39 (1997) 341-2.

[169] N. Shahidzadeh-Bonn, S. Rafai, A. Azouni, D. Bonn, Evaporating droplets, J. Fluid Mech. 549 (2006) 307-13.

[170] M. Cachile, O. Benichou, A. Cazabat, Evaporating droplets of completely wetting liquids, Langmuir. 18 (2002) 7985-90.

[171] S.J. Kline, F. McClintock, Describing uncertainties in single-sample experiments, Mech. Eng. 75 (1953) 3-8.

[172] R. Abernethy, R. Benedict, R. Dowdell, ASME measurement uncertainty, Trans ASME: J. Fluids Eng. 107 (1985) 161-4.

[173] G. Knowles, G. Vickers, J. Anthony, Implementing Evaluation of the Measurement Process in an Automotive Manufacturer: A Case Study, Qual. Reliab. Eng. Int. 19 (2003) 397-410.

[174] National Instrument, Bias Error for Digital Acquisition board, Retrieved December 1, 2008, from http://www.ni.com/dataacquisition/compactdaq/.

[175] VTL, Bias Measurement and Adjustment Instructions, Retrieved September 7, from http://www.vtl.com/pages/bias.html.

[176] J.S. Newman, K.E. Thomas-Alyea, Electrochemical Systems, 3rd Edition, Wiley-Interscience, Hoboken, NJ, 2004.

[177] C. Hamann, A. Hamnett, W. Vielstich, Electrochemistry. 2nd Edition, Weinheim : Wiley-VCH, NY, 2007.

[178] A. Odukoya, G.F. Naterer, Electrochemical mass transfer and entropy generation of cuprous chloride electrolysis, Int. J. Hydrogen Energy. 36 (2011) 11345-52.

[179] H. Ghadamian, Y. Saboohi, Quantitative analysis of irreversibilities causes voltage drop in fuel cell (simulation modeling), Electrochim. Acta. 50 (2004) 699-704.

[180] G.F. Naterer, C.D. Tokarz, Entropy based design of fuel cells, J. Fuel Cell Sci. Tech. 3 (2006) 165-74.

[181] L. Stolberg, H. Boniface, L. Deschenes, S. York, S. McMahon and S. Suppiah, Recent Advances at AECL in the Cu-Cl Cycle for Nuclear-Produced Hydrogen, ORF Workshop on Thermochemical Nuclear-Based Hydrogen Production, Oshawa, ON. December, 2007.

[182] A. Odukoya, G.F. Naterer, I. Dincer, Entropy generation of droplet motion with surface tension hysteresis in a closed microchannel, J. Micromech. Microeng. 21 (2011) 1-11.

[183] A. Odukoya, G.F. Naterer, Experimental study of droplet motion and thermocapillary heat transfer in a closed microchannel, 10th AIAA/ASME Joint Thermophys. Heat Transfer Conf., Chicago IL. 21 (2010).

[184] Y. Yang, A. Odukoya, G.F. Naterer, Droplet meniscus motion of thermocapillary pumping in a closed microchannel with external heating, Proceedings 12th IEEE Inter Society Conference, Las Vegas, NV. (2010) pp. 1-6.

[185] C. Liu, Foundation of MEMS, Pearson Prentice Hall, Upper Saddle River, NJ, 2006.

[186] M. Gad-el-Hak, The MEMS Handbook, 2nd Edition, CRC/Taylor and Francis, Boca Raton, FL, 2006.

[187] J. Greffet, Laws of macroscopic heat transfer and their limits, in: Microscale and Nanoscale Heat Transfer, Springer, Berlin, Germany (2006) pp. 1-13.

[188] D. Liu, S.V. Garimella, Investigation of liquid flow in microchannels, J. Thermophys. Heat Transfer. 18 (2004) 65-72.

[189] G.F. Naterer, Heat Transfer in Single and Multiphase Systems, CRC Press, Boca Raton, FL, 2003.

[190] F.P. Incropera, T.L. Bergman, A.S. Lavine, D.P. DeWitt, Fundamentals of Heat and Mass Transfer, 6th Edition, Wiley, Hoboken, NJ, 2011.

[191] P.S. Glockner, G.F. Naterer, Interfacial thermocapillary pressure of an accelerated droplet in microchannels: Part I. Fluid flow formulation, Int. J. Heat Mass Transfer. 50 (2007) 5269-82.

[192] V.I. Baikov, E.V. Korobko, N.A. Goncharova, Spreading of a liquid droplet over a solid horizontal surface, J. Eng. Phys. Thermophys. 76 (2003) 274-8.

[193] P. Szymanski, Some exact solutions of the hydrodynamic equations of a viscous fluid in the case of a cylindrical tube, J. Math. Pure Appl. 11 (1932) 67-107.

[194] D.W. Appel, P. Hubbard, L. Landweber, E. Laursen, J. McNown, H. Rouse, T. Siao, A. Toch, C. Yih, H. Rouse, Advanced mechanics of fluids, Phys. Today. 12 (1959) 54.

[195] V.S. Arpaci, P.S. Larsen, Heat engineering convection heat transfer, Prentice-Hall, Englewood Cliffs, NJ, 1984.

[196] M.E. Erdogan, On the flows produced by sudden application of a constant pressure gradient or by impulsive motion of a boundary, Int. J. Nonlinear Mech. 38 (2003) 781-97.

[197] M.E. Erdogan, C.E. Imrak, On some unsteady flows of a non-Newtonian fluid, Appl. Math. Model. 31 (2007) 170-80.

[198] Y.S. Muzychka, M.M. Yovanovich, Compact models for transient conduction or viscous transport in non-circular geometries with a uniform source, Int. J. Thermal. Sci. 375 (2004) 161-72.

[199] Y.S. Muzychka, M.M. Yovanovich, Unsteady viscous flows and Stokes's first problem, Int. J. Thermal. Sci. 49 (2006) 820-8.

[200] S. Churchill, R. Usagi, A general expression for the correlation of rates of transfer and other phenomena, AICHE J. 18 (1972) 1121-8.

[201] J. Cho, M. Anderson, R. Richards, D. Bahr, C. Richards, Optimization of electromechanical coupling for a thin-film PZT membrane: II. Experiment, J. Micromech. Microengineering. 15 (2005) 1804-9.

[202] O. Tabata, K. Kawahata, S. Sugiyama, I. Igarashi, Mechanical property measurement of thin films using load-deflection of composite rectangular membranes, Sensor Actuators. 20 (1989) 135-41.

[203] P. Muralt, Piezoelectric thin films for MEMS, Integr. Ferroelectr. 17 (1997) 297-307.

[204] V. Glebovsky, V.Y. Yaschak, V. Baranov, E. Sackovich, Properties of titanium-tungsten thin films obtained by magnetron sputtering of composite cast targets, Thin Solid Films. 257 (1995) 1-6.

Appendix

Appendix 1: List of journals publications

Odukoya, A., Naterer, G. F., "Electrochemical Mass Transfer Irreversibility of Cuprous Chloride Electrolysis", International Journal of Hydrogen Energy, vol. 36, pp. 11345 - 11352, 2011

Odukoya, A., Naterer, G. F., Dincer, I., "Entropy Generation of Droplet Motion with Surface Tension Hysteresis in a Closed Microchannel" (in press), Journal of Micromechanics and Microengineering, vol. 21, pp. 1-11, 2011

Appendix 2: List of conferences publications

Odukoya, A., Naterer, G. F., "Piezoelectric Energy Conversion by Thermocapillary Pumping in a Closed Microchannel", 23rd Canadian Congress of Applied Mechanics, Vancouver, BC, June 5 – 9, 2011

Odukoya, A., Naterer, G. F., "Electrochemical Mass Transfer Irreversibility of Cuprous Chloride Electrolysis for Hydrogen Production", 2nd International Conference on Hydrogen Production, Istanbul, Turkey, June 16 – 18, 2010

Odukoya, A., Naterer, G. F., ``Experimental Study of Droplet Motion and Thermocapillary Heat Transfer in a Closed Microchannel", 10th AIAA/ASME Joint Thermophysics and Heat Transfer Conference, Chicago, Illinois, June 28 – July 1, 2010

Yang, J., Odukoya, A., Naterer, G. F., ``Droplet Meniscus Motion of Thermocapillary Pumping in a Closed Microchannel with External Heating", ITherm 2010 Conference, 12th Intersociety Conference on Thermal and Thermomechanical Phenomena in Electronic Systems, Las Vegas, NV, June 2 – 5, 2010

Appendix 3: Textbook chapter

Odukoya, A., Naterer, G. F., 2011. Clean Energy: Resources, Production and Developments- Chapter 7 - Energy Conversion in Micro-Electromechanical Systems, pp. 245-273